Theses and Dissertations

Summer 2016

Dynamic breathing lung models for healthy and asthmatic subjects based on assessment of regional lung function

Nariman Jahani
University of Iowa

DYNAMIC BREATHING LUNG MODELS FOR HEALTHY AND ASTHMATIC SUBJECTS BASED ON ASSESSMENT OF REGIONAL LUNG FUNCTION

by

Nariman Jahani

A thesis submitted in partial fulfillment
of the requirements for the Doctor of Philosophy
degree in Mechanical Engineering in the
Graduate College of
The University of Iowa

August 2016

Thesis Supervisor: Professor Ching-Long Lin

Graduate College
The University of Iowa
Iowa City, Iowa

CERTIFICATE OF APPROVAL

_____

PH.D. THESIS

_____

This is to certify that the Ph.D. thesis of

Nariman Jahani

has been approved by the Examining Committee for
the thesis requirement for the Doctor of Philosophy degree
in Mechanical Engineering at the August 2016 graduation.

Thesis Committee: _____
Ching-Long Lin, Thesis Supervisor

_____
Eric A. Hoffman

_____
Jia Lu

_____
James H. J. Buchholz

_____
M. L. (Suresh) Raghavan

ACKNOWLEDGEMENTS

ABSTRACT

We develop dynamic breathing lung models for healthy and asthmatic subjects by utilizing two or multiple volumetric multi-detector-row computed tomographic (MDCT) of lung images acquired from both static CT and four-dimensional CT (4D-CT) scans. A mass preserving image registration is utilized to derive local variables including Jacobian (ratio of volume change) and maximum shear strain or anisotropic deformation index (ADI) for assessment of lung deformation, and local air volume and flow rate for assessment of regional ventilation. First, lung image data of six normal human subjects acquired at three static inflation levels, 20% of vital capacity (VC), 60% VC and 80% VC, are used to evaluate the non-linear characteristics of the human lung during deep breathing. We quantify the non-linearity by comparing the variables which are interpolated linearly between 20% and 80% VC images with those of direct registration of 20%, 60% and 80% VC images to observe how the results are deviated from linear curves. Then, we assess regional ventilation, nonlinearity, and hysteresis of the lung motion during dynamic breathing using 4D-CT data sets. Six healthy adult humans are studied during controlled tidal breathing as well as during total lung capacity (TLC) and functional residual capacity (FRC) breath holds. Results from static analysis are utilized to contrast static vs. dynamic (deep vs. tidal) breathing. A rolling-seal piston system is employed to maintain consistent tidal breathing during 4D-CT spiral image acquisition, providing required between-breath consistency for physiologically meaningful reconstructed respiratory motion. Lobar distributions of air volume change during tidal breathing are correlated with those of deep breathing to differentiate regional ventilation between deep and tidal breathing. With ADI, we are able to quantify nonlinearity and hysteresis of lung deformation that can only be

captured in dynamic images. In addition, 4D-CT data sets for six mild/moderate asthmatic subjects are added during tidal breathing following acquisition of two static scans at TLC and FRC. We analyze those data to assess ventilation heterogeneity, non-linear deformation and hysteresis of lung motion to distinguish regional and global features of asthmatic lungs from those of healthy lungs during breathing. Eventually, 4D-CT data for healthy and asthmatic lungs are utilized to derive physiologically consistent boundary conditions for computational fluid dynamic (CFD) simulation of airflow in the human lungs during tidal breathing. We investigate the effect of dynamic breathing on air flow distribution and pressure drop along the central airways.

PUBLIC ABSTRACT

The objective of this work is to develop a realistic dynamic model for breathing human lungs to evaluate lung functions for healthy and asthmatic subjects. We acquire lung images at different inflation level during deep breathing (static) as well as normal (dynamic) breathing. Then, we apply image processing techniques to analyze these lung image data. Image processing techniques provide essential tools to assess how human lung locally moves and how air changes inside the airways of the lung. We quantify non-linear features of human lungs by analyzing lung motion and air volume change using static and dynamic images. We utilize those features to distinguish lung functions derived from static and dynamic imaging. In addition, we use dynamic images to study differences of lung functions between inhaltion and exhalation during normal breathing due to lung hysteresis. Furthermore, knowing these differences helps differentiate lung functions between healthy and asthmatic subjects. Lastly, we use computational fluid dynamics techniques to simulate air flow and pressure distribution in the airways for both healthy and asthmatic lungs during dynamic breathing. The simulation has a potential to provide essential indicators such as airway resistance to predict and evaluate the progress of asthma.

TABLE OF CONTENTS

LIST OF TABLES

LIST OF FIGURES

1 INRODUCTION

1.1 Background

1.1.1 Healthy and asthmatic lung physiology

The lungs are the main respiratory organ in humans. There are two lungs located on each side of the body. Their main function is to exchange oxygen and carbon dioxide so that oxygen is transferred into the blood and CO_2 is released from that. Lung sizes are not the same and the right lung has greater proportion. The left lung is divided into two lobes by an oblique fissure: left lower lobe (LLL) and left upper lobe (LUL) while the right lung consists of three lobes: right lower lobe (RLL), right middle lobe (RML) and right upper lobe (RUL). A horizontal and an oblique fissures separate lobes in the right lung. Lobes are able to slide against adjacent lobes and chest wall (33).

The lung as a part of respiratory system transport the gas through airways. Airways are like a bifurcation network which starts from largest airway called trachea and split into smaller and smaller airways called bronchi and bronchioles. The bronchioles where air is transferred to the alveoli are called the respiratory bronchioles. Air is transferred from the pharynx to the trachea. Then, trachea split the air to the left and right lungs until air is transferred to alveoli where oxygen and CO_2 are exchanged.

Global lung function can be evaluated using pulmonary function test (PFT) considered as non-invasive tests. The test provides information to diagnose the lung disorders and find a certain treatment for that. The PFT data include:

- **Tidal volume**: Lung volume difference between end-inhaltion and end exhalation during normal breathing. The normal value is about 500-600 *ml* in adults.

- **Residual volume (RV)**: The amount of air remaining in the lung after the most forced exhalation. This volume should be calculated via indirect methods and cannot be measured.

- **Vital Capacity (VC)**: The maximum amount of air breathed out after a maximum inhalation.

- **Total lung capacity (TLC)**: The amount of air remaining in the lung after a maximum inhalation. This volume is the summation of RV and VC.

- **Functional residual capacity (FRC)**: The volume representing amount of air at the end of a normal exhalation.

- **Forced expiratory volume (FEV)**: The amount of air measured during a forced exhalation. The amount can be measured at the first (FEV1), second (FEV2), or third seconds (FEV3) of the forced exhalation.

- **Forced vital capacity (FVC)**: The maximum amount of air during the measurement of forced expiratory volume.

Two important types of lung disorders are obstructive and restrictive lung diseases where produce problems with airflow within the lungs. Those disorders are observed in lung disease such asthma and chronic obstructive pulmonary disease (COPD). In this study, we focus on asthmatic human lungs. Asthma is a lung disease characterized by airway inflammation, airway hyper-responsiveness and airflow obstruction. With use of PFT, we are able to find obstructive patterns within the asthmatic lungs. Increase of airway resistance in asthma causes airflow obstruction which can be observed in decrease of FEV1 and FEV1/FVC ratio, and FVC is reduced due to hyperinflation of lung. To evaluate the severity of asthma, a methacholine challenge which increase restriction. Several studies

identified and introduced qualitative and quantitative variables to examine physiological heterogeneity among asthmatic lungs.

1.1.2   *Static and dynamic computed tomography imaging*

Computed tomography (CT) imaging produces high resolution of two-dimensional slices (tomographic images) using combination of several x-ray images obtained from different angles. All slices of a volumetric image are acquired continuously with the scanner table movement and x-ray tube rotation simultaneously. A reconstruction process is applied to generate a three-dimensional image by connecting individual slices. With advances in image acquisition techniques, multi-detector CT (MDCT) imaging allows to collect multiple slices simultaneously in order to provide faster acquisition and more coverage of a volumetric image. As result of high spatial resolution and short acquisition time, MDCT has been used as an effective tool for lung imaging. With use of MDCT imaging, detailed anatomical information of lungs can be extracted. With use of lung segmentation algorithms (35), different parts of such as lungs (left and right lungs), lobes (64), bronchial trees (68), vessel trees (65) and fissures can be segmented. Those accurate segmentation can provide detailed information such as regional lung volumes, airway geometry and local lung density.

CT data sets can be used to assess lung function and respiratory motion. Volumetric lung images can be acquired using both static and dynamic imaging. Static lung images usually are achieved at controlled volumes during breath-hold condition. However, four-dimensional (4D) dynamic image data set are acquired during breathing. 4D-CT imaging has potential to provide physiological meaningful information to assess breathing lungs and distinguish between inhalation and exhalation ((5), (40), (20), (79)). However, relative

to static scans, they have lower resolution and higher radiation dose. In addition, to reduce artificial motion and acquire consistent images, it is important that subjects to be scanned at consistent lung volumes (60). In this study, both static and 4D-CT image data were acquired during breath-hold and tidal breathing, respectively. All CT image acquisition were approved by the University of Iowa's Institutional Review Board.

1.1.3   Regional ventilation and deformation

Analysis of lung volume change and respiratory motion is the primary metric to assess the lung function and its health. Because the lung moves non-uniformly and has non-linear behavior, its motion yields regional heterogeneous ventilation and displacement field within the lung (59). Therefore heterogeneity of regional values leads to that diagnostic of lung diseases and consequently, radiotherapy techniques to be region-specific.

Regional ventilation is assessed by estimating local volume change (Jacobian) and distribution of local air volumes within the lung. The given regional ventilation would give more physiological information if we achieve and analyze those values during breathing and combine those with a measured respiratory cycle like what it is done with 4D-CT image data during tidal breathing. Combining regional ventilation with the respiratory cycle allows to quantify local dynamic flow within the lung to simulate local breathing pattern of healthy and diseased lungs (15). Further studies showed that assessment of regional deformation is not just volume change (1). Anisotropic deformation may also exist independent from volume change. In the other word, the local volume may be constant while it deforms significantly when we have expansion in one direction and contraction along other direction. Anisotropic deformation can be used to capture non-linearity of the

lung motion during breathing (41). Although non-linear motion is observed in both static and dynamic breathing scans, we can differentiate breathing characteristics between inhalation and exhalation using dynamic scans (40). Therefore, estimation of non-linearity in dynamic breathing results in quantifying hysteresis of lung motion between inhaltion and exhalation ((5), (15)).

1.1.4 Image registration techniques

Image registration is a method to determine a spatial transformation to match any pairs of images acquired at different positions and times or image data from different imaging modalities. Because of non-uniform deformation of the lung, it is better to use non-rigid image registration methods to capture accurate motion of each local point within the lung (83). Several image registration techniques as powerful tools in medical imaging have been utilized in several studies to link the lung images from different lung volumes, times or modalities ((8), (25), (43)). Image registration can provide regional functional parameters such as regional ventilation, regional deformation, and deformation of the airway tree to assess lung function and respiratory motion. In addition, those regional lung information can be used to evaluate altered local function of diseased lungs such as asthma and COPD.

1.1.5 Computational fluid dynamics

Computation fluid dynamics (CFD) has become an important tool to assess flow pattern, particle deposition and shear forces at the airways surfaces ((26), (52), (80)). Quantitative assessment of regional ventilation allows to generate physiologically meaningful boundary condition to be applied in CFD simulation. Several studies developed CFD methods using breath-hold lung images to analyze flow pattern assuming ideal

breathing cycles ((80), (81)). However, regional ventilation estimated from 4D-CT image data can be combined with actual breathing cycle to derive time-varying global and local flow rate at the boundaries of terminal airways to estimate more physiological results. Furthermore, air flow simulation can be developed for application such as analysis of flow pattern in lungs with asthma or COPD to predict regional airflow obstruction and pressure distribution.

1.2 Overall goals

The main purpose of this study is to develop breathing lung models for both healthy and asthmatic human subjects using volumetric lung images at different phases with image registration techniques. An algorithm is implemented to link local variables to global lung volume to assess lung motion during breathing. Local variables such as regional ventilation, Jacobian and anisotropic deformation are quantified from displacement field obtained from a mass preserving image registration method. In this study, we consider two ways to achieve different lung volumes at different inflation levels. First, we acquire three static MDCT lung images at FRC, TLC and an intermediate lung volume between FRC and TLC for healthy human subjects. In the second way, we obtain 4D-CT lung volumes during tidal breathing following acquisition of two deep breathing scans at TLC and FRC for both healthy and asthmatic human lungs. The novelty of 4D-CT image acquisition in this study is that a rolling-seal piston system is employed to maintain consistent tidal breathing during 4D-CT spiral image acquisition, providing required between-breath consistency for physiologically meaningful reconstructed respiratory motion. Therefore, unlike static scans, actual breathing waveform is measured. In the three-image analysis, we evaluate non-linear characteristics of lung behavior by quantifying regional ventilation and

deformation during deep berating. In this case, an ideal sinusoidal waveform is assumed to calculate the flow and deformation rates. Then, the results are compared with two-image (TLC and FRC) linear interpolation to quantify the degrees of non-linearity of variables being deviated from those based on linear assumption. In the 4D-CT image analysis, the healthy subjects are first analyzed to define sensitive local variables during dynamic breathing. The aim is to assess asymmetric regional ventilation, nonlinearity, and hysteresis of human lungs during dynamic breathing at tidal volume. In addition, quantitative assessments of 4D-CT image data are utilized for comparison with the results obtained from two-image and three-image based analyses to contrast static vs dynamic (deep vs. tidal) breathing. Then, the analysis is utilized for asthmatic subjects to distinguish regional and global features of asthmatic lungs from those of healthy lungs during breathing. Quantification of ventilation heterogeneity, non-linearity and hysteresis of lung motion allow to evaluate different characteristics between healthy and asthmatic lungs. Furthermore, precise analysis of regional ventilation during tidal breathing allows us to estimate physiologically meaningful time-varying airflow distributions in order to define improved boundary conditions for CFD simulation. Then, we will apply those improved boundary conditions and deforming lung geometric models for CFD simulation of airflow in healthy and asthmatic lungs.

1.3 Specific aims

The specific aims of this study are listed as follows:

1. Evaluation of non-linear characteristics of human lungs via image registration-derived local variables based on MDCT lung volumetric image data of six normal human subjects acquired at three inflation levels: 20% VC, 60% VC and 80% VC.

- Constructing a quadratic relationship between local variables and global air volumes of the lung.

- Comparing three-image-based results with the two-image-based results in which local variables change linearly.

2. Assessment of regional ventilation, nonlinearity, and hysteresis of human lungs during dynamic breathing via image registration of 4D-CT scans for six healthy subject during tidal breathing as well as during TLC and FRC.

   - Controlling the tidal volume during dynamic imaging with a with a unique dual rolling-seal piston for accurate image reconstruction.

   - Deriving sensitive local variables, such as air volume and flow rate for assessing regional ventilation and anisotropic deformation index (ADI) for quantifying nonlinearity and hysteresis of lung motion.

   - Comparing 4D-CT-derived regional ventilation with those estimated by linear and non-linear assumption in static scans.

3. Differentiation of characteristics of regional functional variables in asthmatic lungs from healthy lungs during dynamic and static breathing.

   - Quantifying regional ventilation, heterogeneity, non-linearity and hysteresis of lung deformation to assess differences in respiratory motion between healthy and asthmatic subjects using 4D-CT image data.

   - Comparing analysis of tidal breathing with that of deep breathing in asthmatic lungs.

- Quantifying local alterations of structural variables [bifurcation angle, circularity, airway wall thickness (WT), and hydraulic diameter (Dh)] in asthmatic subjects during tidal breathing.

4. CFD simulation of airflow in selected healthy and asthmatic subjects using 4D-CT image data.

   - Deforming the surface mesh to match other CT images using the image registration technique.

   - Investigating the effect of dynamic breathing on pressure drop and resistance along the central airways for both healthy and asthmatic lungs.

2   ASSESSMENT OF REGIONAL NON-LINEAR VENTILATION AND TISSUE DEFORMATION USING THREE BREATH-HOLD CT DATA SETS

2.1 Introduction

The non-linear characteristics of the human lungs make quantitative assessment of lung deformation at intermediate inflation levels challenging. Previous studies showed that changes inside lungs, such as lung deformation, occur regionally (59). The ability to detect more sensitively regional changes of the lungs as a function of inflation level can potentially improve early detection of abnormalities in diseased lungs.

Several image-processing methods have been proposed to evaluate regional changes of the lungs ((4), (14)). One technique to assess lung expansion is deformable image registration ((15), (62)). Yin et al. (83) developed a mass preserving non-rigid registration technique for pairs of lung images. Matching of two images yields the displacement field needed to calculate regional tissue deformation and air volume change. To evaluate lung expansion, parameters such as regional lung deformation and ventilation can be estimated. West & Matthews (73) showed that lung may exhibit regionally anisotropic deformation, being independent from volume change. Consequently, some studies employed anisotropic deformation index in addition to volume change to provide some sensitive measures of regional lung deformation (1, 13). However, if only two lung volumetric images, typically one image at the end of normal expiration (functional residual capacity, FRC, or residual volume, RV) and the other at the end of a maximal inspiration (total lung capacity, TLC), are available, analysis and prediction of lung mechanical

behaviors may not adequately account for non-linear behaviors of the lungs at intermediate inflation steps during normal breathing.

Recent advances in MDCT and four-dimensional CT allow one to interrogate regional changes in the lungs at multiple inflation levels and time points. Different studies used those images to consider different aspects of lung motion, such as dynamic airflow and tissue motion, to study the pulmonary function at different inflation levels ((19), (27), (48), (62)). Although dynamic images are more desirable than static images to study lung functions, static images provide higher spatial resolution images. Ding et al.(17) performed CT experiments on four adult sheep to evaluate lung expansion for both static and dynamic images via image registration. They compared registration-derived volume changes to regional ventilation measured from Xenon-CT images, demonstrating good correlations between them for both dynamic and static images. However, only a few of studies investigated the non-linear behaviors of the lungs in comparison with linear counterparts using two images. Yin et al. (80) proposed a method to simulate air flow in the human lung by registering two lung images for subject-specific regional ventilation, demonstrating more physiologically consistent lobar air distribution than the one image-based approach (49). Later, Yin et al. (81) proposed a multiscale breathing lung model based on three MDCT lung images of one human subject. Unlike the two image-based approach with constant flow rates during respiration, the three image-based algorithm can derive time-varying flow boundary conditions for computational fluid dynamics analysis of pulmonary airflow.

The objective of this paper is to examine non-linear characteristics of the human lung by matching MDCT volumetric lung images at three inflation levels. Local variables

of lung deformation and air flow derived via image registration are then used to construct a quadratic relationship between local variables and global air volumes of the lung. The results are compared with the two-mage based results in which local variables change linearly. We further quantify the differences of these local variables at intermediate inflation levels obtained by two-image linear interpolation and three-image quadratic interpolation, and discuss non-linear lung behaviors.

2.2 Method

2.2.1 MDCT image acquisition

The MDCT lung volumetric images for six normal human subjects were acquired in the supine position at three static inflation levels: 20% of vital capacity (VC), 60% VC and 80% VC. Variables corresponding to 20%, 60% and 80% VC are denoted with subscripts 1, 2 and 3, respectively. We used a Siemens Sensation 64-slice MDCT scanner (Forchheim, Germany) with 120 kV, 75 mAs, 0.75 mm slice thickness, 500 mm field of view. The University Institutional Review Board approved the scanning protocol. The software Apollo (VIDA Diagnostics, Coralville, Iowa) was used to segment the lungs and lobes of CT images.

2.2.2 Image registration

If image intensity $I(\mathbf{x})$ in the Hounsfield unit (HU) is known at position $\mathbf{x}$, the air and tissue fractions are calculated as

$$\beta_{air}(\mathbf{x}) = \frac{HU_{tissue} - I(\mathbf{x})}{HU_{tissue} - HU_{air}} \quad \text{and} \quad \beta_{tissue}(\mathbf{x}) = \frac{I(\mathbf{x}) - HU_{air}}{HU_{tissue} - HU_{air}} \tag{2.1}$$

where the HUs of air and tissue are taken as HU_{air}= -1000 and HU_{tissue}=55, respectively. In mapping two images, one image is chosen as the reference image and the other the floating image. The registration is to determine an optimal spatial transformation that matches the

two images by minimizing a cost function E based on the local tissue difference between the corresponding regions (83).

$$E = \sum_{\mathbf{x} \in \Omega} \left[v_r(\mathbf{x}) \beta_{tissue}^r(\mathbf{x}) - v_f(\mathbf{T}(\mathbf{x})) \beta_{tissue}^f(\mathbf{T}(\mathbf{x})) \right]^2 \qquad (2.2)$$

where $\mathbf{T}(\mathbf{x})$ is the transformation function which maps a point at location $\mathbf{x}$ in the reference image to the corresponding point in the floating image. v_r and v_f are the volumes of the corresponding point in the reference and floating images, respectively. The subscripts (or superscripts) r and f denote the reference and floating images, respectively. In this study, mappings are done for 20%-80% VC and 20%-60% VC pairs with 80% VC and 60% VC images as the reference images, respectively, and 20% VC is used as the floating image.

2.2.3   Variables definition

Deformation Indices

The transformation function obtained by image registration is used to construct variables for assessment of local volume change and anisotropic deformation. The deformation gradient tensor is defined below as the gradient of transformation function

$$\mathbf{F} = \nabla \mathbf{T} \qquad (2.3)$$

The eigenvalues of $\mathbf{F}^T\mathbf{F}$, λ'_{pi}, at a given point, are associated with each local volume from 80% to 20% VC or 60% to 20% VC. Consequently, the principal strains of lung tissue deformation, λ_{pi}, from 20% to 80% VC or 20% to 60% VC are calculated as (13)

$$\lambda_{pi} = \frac{1}{\sqrt{\lambda'_{pi}}} \qquad (2.4)$$

 With principal strains, we can define two independent indices that measure lung deformation.

Jacobian, $J = v_r(\mathbf{x})/v_f(\mathbf{T}(\mathbf{x}))$, is defined as the ratio of local lung volume at a given inflation level to the volume at 20% VC, measuring contraction or expansion relative to the 20% VC. That is, there is local expansion if $J > 1$ and local contraction if $J < 1$. The definition of Jacobian in terms of principal strains is

$$J = \lambda_{p1}\lambda_{p2}\lambda_{p3} \tag{2.5}$$

where subscripts $p1$, $p2$ and $p3$ denote three principal strains. Also, a body can deform while its volume is constant. For example, consider a cube whose lines are initially perpendicular to each other. A cube can be deformed into a parallelepiped volume by change in angle between any pair of orthogonal lines while remaining a constant volume. This change in angle, ψ, from 90° is a representation of shear strain, γ, defined as

$$\gamma = \tan\psi \tag{2.6}$$

By sorting these eigenvalues as $\lambda_{p1} > \lambda_{p2} > \lambda_{p3}$, the local shear strain, γ_{max}, is given by (24)

$$\gamma_{max} = \frac{\lambda_{p1} - \lambda_{p3}}{2} \tag{2.7}$$

Similarly, Napadow et al. (54) determined anisotropy index by subtraction of axial strains in a 2D plane. Since γ_{max} is proportional to maximum difference between principle strains, it can be considered as an anisotropy index in a 3D domain. Thus, isotropic deformation occurs when volume increases equivalently in all direction (e.g. $\lambda_{p1} = \lambda_{p2} = \lambda_{p3}$), which corresponds to $\gamma_{max} = 0$. On the other hand, anisotropic deformation is associated with greater difference between principal strains, resulting in higher value of γ_{max}.

Air volume

For each registration, air volume at position **x** can be calculated at the two levels as

$$v_{air}^r(\mathbf{x}) = v_r(\mathbf{x})\beta_{air}^r(\mathbf{x})$$
$$v_{air}^f(\mathbf{x}) = v_f(\mathbf{T}(\mathbf{x}))\beta_{air}^f(\mathbf{T}(\mathbf{x})) \tag{2.8}$$

where v_{air}^r and v_{air}^f are the air volumes at the reference image (60% or 80% VC) and floating image (20% VC), respectively. β_{air} is calculated by Eq. (2.1).

2.2.4 Interpolation method

For lung air volumes at three states 20% (V_1), 60% (V_2) and 80% VC (V_3), corresponding local variables f_1, f_2 and f_3, are used to approximate variable f as a quadratic function of the total lung air volume.

$$f(\mathbf{x}, V(t)) = a(\mathbf{x}) + b(\mathbf{x})V(t) + c(\mathbf{x})V(t)^2 \tag{2.9}$$

Since the images are scanned statically and the time information is not available, the global lung air volume change is assumed following a sinusoidal breathing waveform. The global lung air volume at a reference normalized time, t^*, with a time period of unity is taken as

$$V(t^*) = V_1 + \frac{\Delta V}{2}(1 - \cos(2\pi t^*)) \tag{2.10}$$

where V_1 and V_3 are roughly corresponding to FRC and TLC, respectively and $\Delta V = V_3 - V_1$. Thus, the reference times for the minimum volume (V_1) and the maximum volume (V_3) are 0 and 0.5, respectively, and the peak inspiratory flow rate corresponds to $t^* = 0.25$ (81). In the case of using linear interpolation based on two images (20% and 80% VC), the coefficient $c(\mathbf{x})$ in Eq. (2.9) is set to zero, whereas the waveform Eq. (2.10) remains the same.

By using air volume, Jacobian and local shear strain, respectively, as f in Eq. (2.9) measured at V_1, V_2 and V_3, quadratic interpolation functions of these variables can be constructed as a function of global lung air volume. Then, the time rate of change of these variables can be calculated as

$$\frac{\partial f(\mathbf{x}, t)}{\partial t} = \frac{\partial f}{\partial V}\left[\frac{dV}{dt^*}\right]\frac{dt^*}{dt} = (b + 2cV)[\pi(\Delta V)\,\sin(2\pi t^*)]\frac{dt^*}{dt} \tag{2.11}$$

where $\frac{dt^*}{dt}$ is uniform and set to unity with $t^*=t$ hereafter.

The entire human lung can be divided into left and right lungs. The left lung consists of two lobes [(left upper lobe, left lower lobe)=(LUL, LLL)], whereas the right lung consists of three lobes [(right upper lobe, right middle lobe, right lower lobe)=(RUL, RML, RLL)]. Thus, there are a total of five lobes and the left lung is usually smaller than the right lung. To find the rate in a region of interest R, we calculate

$$\sum_{\mathbf{x} \in R}\frac{\partial f(\mathbf{x}, t)}{\partial t} = \left(\sum_{\mathbf{x} \in R}\frac{\partial f}{\partial V}\right)\frac{dV}{dt} = \frac{\partial\,\sum_{\mathbf{x} \in R} f}{\partial V}\frac{dV}{dt} \tag{2.12}$$

With the assumption that the region R is the total lung and f is local air volume, $\sum_{\mathbf{x} \in R} f = V$, $\sum_{\mathbf{x} \in R}\partial f(\mathbf{x}, t)/\partial t = dV/dt$, indicating that the above method conserves the global lung air flow. The local variables of air volume, Jacobian and shear strain are normalized by their respective medians at the 80% VC level, and are denoted by $airV^*$, J^* and γ^*_{max}, respectively. Furthermore, the total air volume V in Eq. (2.10) is normalized as

$$V^* = \frac{(V - V_1)}{\Delta V} \tag{2.13}$$

Thus, $0 \le V^* \le 1$ and $V^* = (0, 0.5, 1)$ correspond to the beginning, peak and end of the inspiration $t^*=t=(0, 0.25, 0.5)$, respectively, in a sinusoidal waveform. In the following analysis, V^* is used in Eqs. (2.9) and (2.11) to account for inter-subject variations of lung

size so that the average coefficients of *a*, *b*, and *c* based on all the subjects can be calculated. In the following presentation, data at different inflation levels are warped to the 80% VC domain for comparison.

2.3 Results

2.3.1 Assessment of two-image linearly interpolated intermediate state

If CT images are available only at 20% and 80% VC, variables at any intermediate state between them, e.g. 60% VC, can only be approximated using linear interpolation. Since the intermediate state at 60% VC is available in this study, we can derive, via registration, the variables in association with the volume change from 20% to 60% VC, and compare them with those linearly interpolated using the results from registering 20% and 80% VC images (see section 2.2.4, Eq. (2.9) with *c*=0). Figure 2.1 (left column) shows the distributions of air volume, Jacobian and shear strain obtained via direct registration of images at 20% and 60% VC, while Figure 2.1 (right column) shows those obtained from linear interpolation between 20% and 80% VC. To quantify the differences between the two methods, the relative errors, the correlation factors using linear regression analysis and the paired student t-tests were performed for each subject (see Table 2.1). The sample size for local variables in the whole lung as well as in each of the five lobes was large and ranged between 40,000 and 500,000. These data exhibit normal distributions. The t-tests are significant for all variables ($P < 0.05$) and the errors are greater in shear strain than those found in Jacobian and air volume. Also, correlation factors ($r^2 < 0.85$) show that the variables at the intermediate state of 60 %VC calculated with linear interpolation only roughly agree with those by matching 20% and 60 %VC.

2.3.2 Three image-based, quadratic interpolation

With three images, the quadratic interpolation as described by Eq. (2.9) is employed to calculate variables at intermediate states. In all cases the lung air volume changes from 20% to 80% VC. The results are presented by lung and by lobe at multiple inflation levels (see V^* in Eq. (2.13)). Also the average rates of change of each variable with respect to V^* are displayed. Note that the rates of change based on linear interpolation between 20% and 80% VC are constant with respect to V^*.

Air volume

Figure *2.2*A shows the air volume distributions of a subject at $V^* = 0.01, 0.25, 0.50, 0.75$ and 0.99 in a sagittal section at which the dorsal surface and the ventral surface are on the right and left, respectively, and the diaphragm is at the bottom. Air volume at $V^* = 0.01$, closest to the 20% VC, has the minimum value in all regions and increases to the maximum value at $V^* = 0.99$, closest to 80% VC, which is almost uniform in all regions. The result shows that the ventral section reaches the maximum capacity for air first and then, the dorsal regions are filled with air. Figure *2.2*B shows the average lobar distributions of air volume based on all the subjects at various inflation levels. At the initial states, the upper and middle lobes have greater values than the lower lobes, but with increasing V^*, the difference of the air volumes between them is diminished and they reach to almost the same level and become uniform at the final stage. The averages of the coefficients in Eq. (2.9) for all the subjects are tabulated in Table 2.2 for the whole lung and for each lobe. In addition, to compare the air volumes calculated with two-image linear interpolation and three-image quadratic interpolation, paired student t-tests were done in the whole lung and in each lobe, indicating that they are different ($P < 0.05$).

Figure 2.3A shows the average total lung air flow rate calculated with Eq. (2.12). As expected, air flow rate has its peak at the middle with V^*=0.5. Since the global variable in Eq. (2.9) is the total air volume, two image-based (linear interpolation between 20% and 80% VC) and three image-based (quadratic interpolation between 20%, 60% and 80% VC) methods give the same result for the flow rate of the whole lung. However, the local flow rates in three image-based method are different from those of two image-based method in which the rates are constant. For example, Figure 2.3B and C show the lobar flow rates in the respective left and right lungs. The flow rates in the lower lobes are greater than those of the upper and the middle lobes, and reach their maxima later at $V^* \cong 0.54$ and 0.56 for LLL and RLL, respectively, than the peak of the total lung flow rate. On the other hand, the peaks of the middle and upper lobes occur earlier at $V^* \cong 0.39, 0.46$, and 0.44 for RML, RUL and LUL, respectively.

Jacobian

Figure 2.4A shows the distributions of Jacobian at four different volumes of $V^* = 0.25, 0.5, 0.75, 1$. Jacobian at volume close to 20% VC is almost unity and is not shown. The dorsal surface and the bottom close to the diaphragm have most expansion as the volume increases. Furthermore, Figure *2.4*B shows that the largest and smallest Jacobian values occur in the lower lobes and the upper lobes, respectively. The averages of the coefficients in Eq. (2.9) for Jacobian based on all six subjects are given in Table 2.3. To compare two and three image-based results, paired student t-tests were performed, showing that the Jacobin calculated by linear and quadratic interpolations are different ($P < 0.05$).

shear strain

Figure 2.5A shows the distributions of local shear strain γ_{max}^* at different inflation levels. Local shear strain is mainly found at the bottom of the ventral surface. With increasing V^*, the increase of γ_{max}^* starts from the bottom of the ventral surface, and then spreads to the upper regions. Figure 2.5B shows that the lobar changes of average γ_{max}^* at various inflation levels. The results show that high γ_{max}^* is located in the lower and middle lobes of LLL and RML, whereas low γ_{max}^* is found in the upper lobes of LUL and RUL at all inflation levels. The average interpolation coefficients for γ_{max}^* are listed in Table 2.4. Paired student t-tests were performed to compare γ_{max}^* calculated by two image-based and three image-based methods. The result shows *P*<0.05, indicating that they are different. Also, a comparison between γ_{max}^* and the anisotropic deformation index (ADI) defined as

$$\sqrt{\left(\frac{\lambda_{p1}-\lambda_{p2}}{\lambda_{p2}}\right)^2 + \left(\frac{\lambda_{p2}-\lambda_{p3}}{\lambda_{p3}}\right)^2}$$ by Amelon et al. (1) shows a strong correlation coefficient of r^2>0.88.

Figure 2.6A exhibits the average rates of γ_{max}^* in the total lung as a function of V^* calculated with two-image linear interpolation and three-image quadratic interpolation. With quadratic interpolation, average rates of γ_{max}^* reaches the peak at $V^* = 0.37$, which is earlier than those of air volume and Jacobian at $V^* = 0.5$. Figure 2.6B and C further show the averages of γ_{max}^* in the left and the right lungs, respectively. The peaks of the rates in the lower and middle lobes occur earlier (at $V^* \cong 0.32, 0.34, 0.31$ for LLL, RLL and RML, respectively) than those of the upper lobes (at $V^* \cong 0.39$ and 0.44 for LUL and RUL, respectively).

2.4 Discussion

In this study, we examined non-linear behaviors of lung deformation and air volume change by applying image registration to CT images acquired at three static inflation levels. Specifically the change of local volume and anisotropy in lung deformation were measured by two independent indices: Jacobian and shear strain. These indices were calculated using the eigenvalues obtained from the registration-derived transformation function (Eqs. (2.5) and (2.7)). Moreover, to investigate air volume change in the lung, we calculated air volume by Eq. (2.8). With two images, regional variables are assumed to change linearly. With three images, non-linear behaviors of the lung in terms of the above variables can be investigated by employing quadratic interpolation.

Comparison of air volumes obtained by directly matching 20% and 60 % VC images and by linearly interpolating between 20% and 80% VC (Table 2.1 and Figure 2.1) showed that the linear interpolation reveals non-uniform regional air volume, but is not sensitive enough to detect local non-linear features with $r^2 < 0.85$, RMS error $> 12\%$ and $P < 0.05$. Subsequently, a three image-based method was applied to examine the changes of air volume at multiple inflation levels. Because of body posture and diaphragm motion, dorsal surface and lower lobes can inflate more so that air is distributed uniformly at the 80% VC stage in the whole lung (Figure 2.2). These results are consistent with the observed physiology of ventilation in subjects with supine position ((50), (62))

As for Jacobian, both two and three image-based method showed that the Jacobian has the largest values in the lower lobes and also in the dorsal surfaces (Figure 2.1 and Figure 2.4), which are consistent with the diaphragm motion and in good agreement with the principle that volume changes more in the regions close to the diaphragm (1). However,

unlike the flow rates obtained by two-image linear interpolation whose peaks occur at the middle of $V^* = 0.5$, the three-image results (see Figure 2.3) showed that the peaks of the flow rate in the upper and the middle lobes occur earlier than those of the lower lobes. These observations agree with the fact that some regions in these lobes reach their maximum capacity for air before the 80% VC level (Figure 2.1A).

In this study, the index of shear strain was adopted to represent anisotropic deformation. Since there was a good correlation between the shear strain and the ADI index proposed by Amelon et al. (1) with $r^2 > 0.88$, it is concluded that shear strain can be used to measure the degree of anisotropic deformation. As for shear strain, Table 1 and Figure 1c showed that the two-image linear interpolation approach yields more error in predicting local non-linear tissue deformation in terms of shear strain (or ADI) than air volume and Jacobian. The three-image results showed that shear strain has the highest value in the inferior region due to large deformation in association with the diaphragm motion. With two image linear interpolation, the rates of all local variables with respect to V^* are constant and the peaks of both the flow and the shear strain rates occur at V^*=0.5, being the same as the peak of the sinusoidal waveform (Figure 2.3A and Figure 2.6A). However, three image-based results showed that shear strain rate peaks at $V^* \cong 0.37$, which is earlier than the peak of the flow rate (Figure 2.6A). This earlier peak was also observed in the results of ADI.

From the perspective of lung mechanics, the current result is consistent with the notion that under quasi-static conditions the elasticity at low lung volume is lower, especially in dependent lung regions, than at high lung volumes. Thus, lung tissue deforms more at low lung volumes, as has been shown by Hoffman et al using early volumetric CT

methodologies ((31), (32), (33)). That is, shear strain represents tissue deformation and tissue deforms more at low lung volumes, thus the peak of shear rate occurs earlier than the peak inspiration. In addition, the lower lobes have higher shear strains and airflow rates than the upper lobes. Therefore, the three image-based variables, as expected, provide more sensitive measures of non-linear lung mechanics both in time and space. This is important when seeking to understand regional interactions associated with lung pathophysiology, particularly when evaluating the lung for mechanical changes associated with early pathological processes. A critical pathway that bridges lung mechanics and biology is through the mechanosensing capability of bronchial epithelial cells (22). Sensitive measures of local lung structural and functional variables can allow one to study local alterations of mechanical forces that may lead to inflammation.

In all cases, we constructed the interpolation function as a function of total air volume and then we applied the sinusoidal waveform independently to calculate the rates (Eq. (2.10)). For other waveforms, the time rate of change of variables can be assessed by merely re-calculating $[dV/dt^*]$ in Eq. (2.11). Also, the calculated interpolation coefficients (Tables 2.2-2.4) allow one to estimate the average of each variable in the total lung and each lobe at arbitrary inflation levels. This is important to improve simulation of pulmonary gas flow as described in Yin et al. (80) and (81). In conclusion, we showed that three image-based method is able to capture some non-linear behaviors of the lung that are missing in the two-image based analysis.

Table 2.1. Comparison of two-image based and image registration methods for the air volume, Jacobian and shear strain in the total lung and each lobe

$airV^*$	RMS error%	r (correlation factor)	P (t test)
Total lung	11.27	0.82	< 0.05
LLL	12.39	0.81	< 0.05
LUL	11.19	0.77	< 0.05
RLL	11.35	0.85	<0.05
RML	11.49	0.82	<0.05
RUL	9.41	0.86	<0.05
J^*	RMS error %	r (correlation factor)	P (t test)
Total lung	7.34	0.86	< 0.05
LLL	9.26	0.82	< 0.05
LUL	8.55	0.77	< 0.05
RLL	8.33	0.86	< 0.05
RML	9.43	0.81	< 0.05
RUL	6.85	0.84	< 0.05
γ_{max}^*	RMS error%	r (correlation factor)	P (t test)
Total lung	28.34	0.78	< 0.05
LLL	27.07	0.78	< 0.05
LUL	27.54	0.73	< 0.05
RLL	32.21	0.77	< 0.05
RML	31.66	0.79	< 0.05
RUL	23.16	0.81	< 0.05

Table 2.2. Means (±SE) of a, b and c coefficients in Eq. (9) for the air volume of the total lung and each lobe

$airV^*$	a	b	c
	Mean (± SE)	Mean (± SE)	Mean (± SE)
Whole	0.0129 (0.001)	0.4317 (0.010)	0.5433 (0.009)
LLL	0.0459 (0.004)	0.4623 (0.009)	0.4695 (0.017)
LUL	-0.0413 (0.006)	0.4398 (0.021)	0.5873 (0.015)
RLL	0.0766 (0.001)	0.4105 (0.004)	0.4908 (0.002)
RML	-0.0519 (0.001)	0.4051 (0.028)	0.6511 (0.022)
RUL	-0.0220 (0.005)	0.4180 (0.003)	0.5941 (0.007)

Table 2.3. Means (±SE) of a, b and c coefficients in Eq. (9) for the Jacobian of the total lung and each lobe

J^*	a	b	c
	Mean (± SE)	Mean (± SE)	
Whole	-0.0193 (0.001)	0.4038 (0.008)	1
LLL	0.0059 (0.008)	0.4698 (0.021)	1
LUL	-0.0465 (0.005)	0.3793 (0.016)	1
RLL	0.0056 (0.007)	0.4371 (0.006)	1
RML	-0.0652 (0.005)	0.3375 (0.018)	1
RUL	-0.0307 (0.001)	0.3526 (0.008)	1

Table 2.4. Means (±SE) of a, b and c coefficients in Eq. (9) for the shear strain of the total lung and each lobe

γ^*_{max}	a	b	c
	Mean (± SE)	Mean (± SE)	
Whole	-0.4969 (0.028)	1.4131 (0.034)	0
LLL	-0.5988 (0.021)	1.7023 (0.071)	0
LUL	-0.3487 (0.011)	1.2054 (0.028)	0
RLL	-0.6491 (0.097)	1.5609 (0.117)	0
RML	-0.6792 (0.017)	1.7938 (0.051)	0
RUL	-0.3739 (0.049)	1.1602 (0.045)	0

Image Registeration   Linear Interpolation

Air Volume

Image Registeration   Linear Interpolation

Jacobian
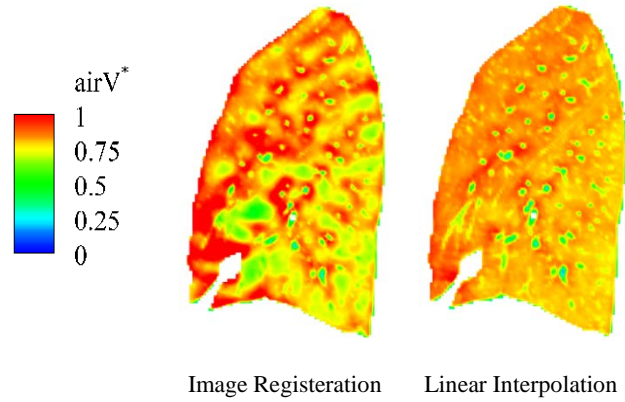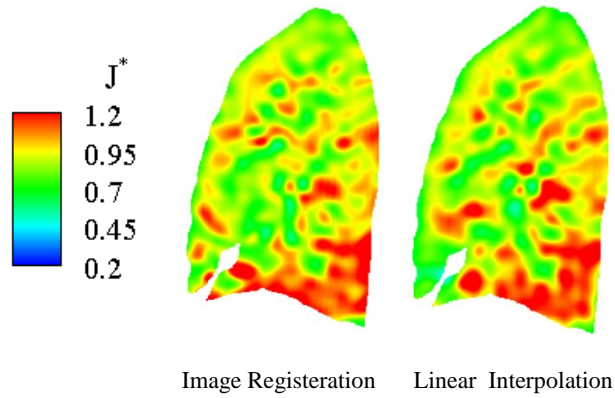
Image Registeration   Linear Interpolation
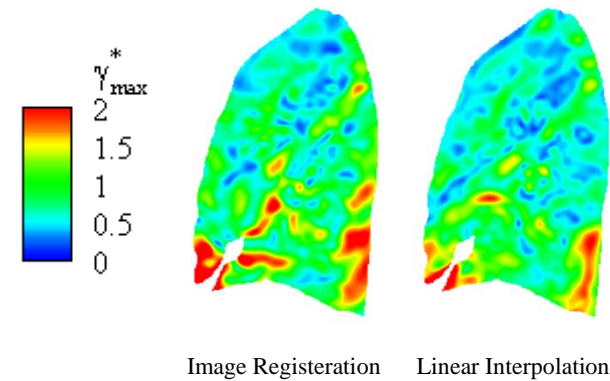
Shear strain

Figure 2.1. Comparison between normalized variables obtained by image registration between 20% and 60 %VC and linear interpolation at 60% VC between 20% and 80% VC: (a) Air volume (b) Jacobian (c) Shear strain

A

B
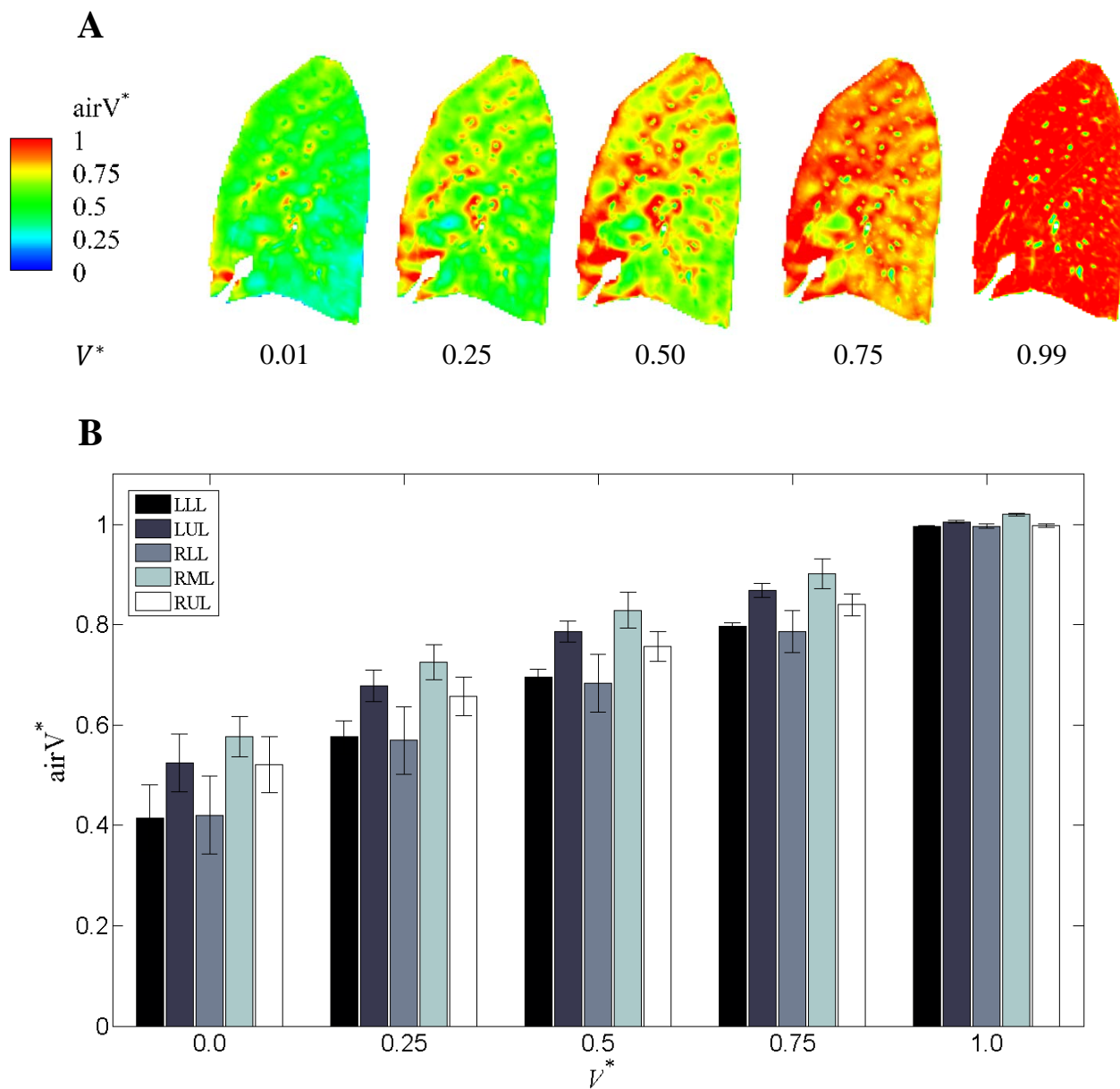
Figure 2.2. Regional normalized air volume at different levels. A: Air volume distribution for a certain subject. B: Bar graph showing lobar air volume values. The average and standard deviation show the median of a group of six subjects

A

B

C
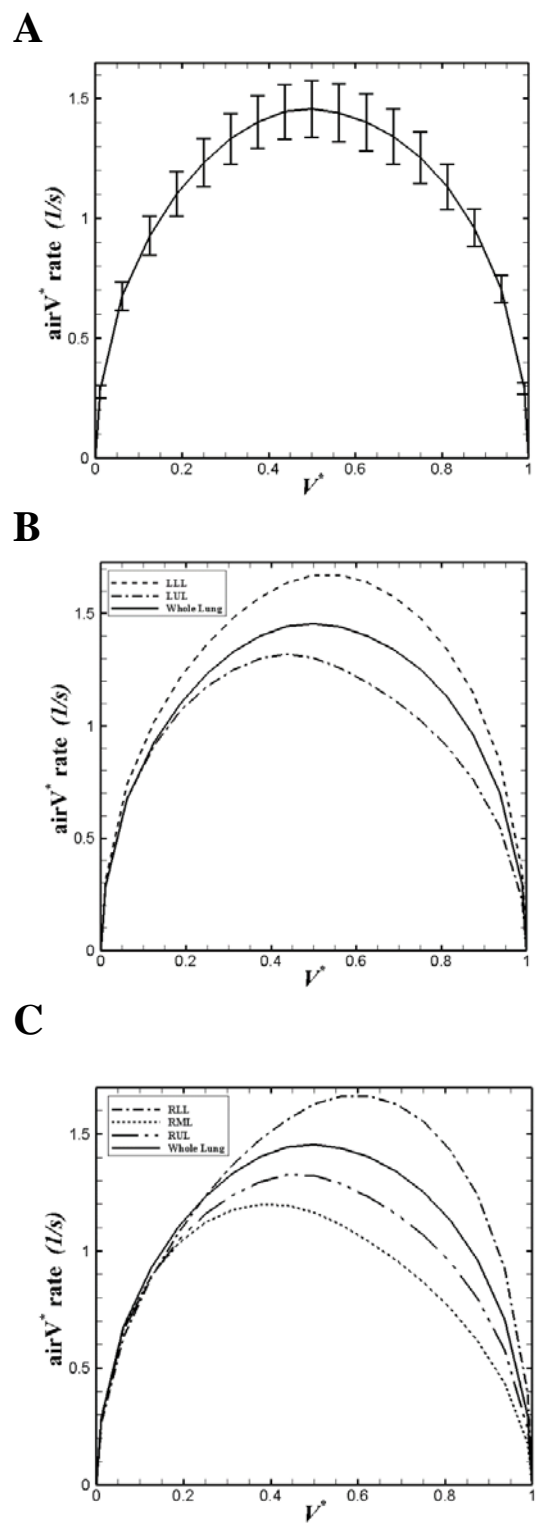
Figure 2.3. Normalized flow rates. A: the whole lung: comparison between linear and quadratic forms. The lines represent the average and standard deviation of the median flow rate of six subjects. B: left lobes C: right lobes

A

B
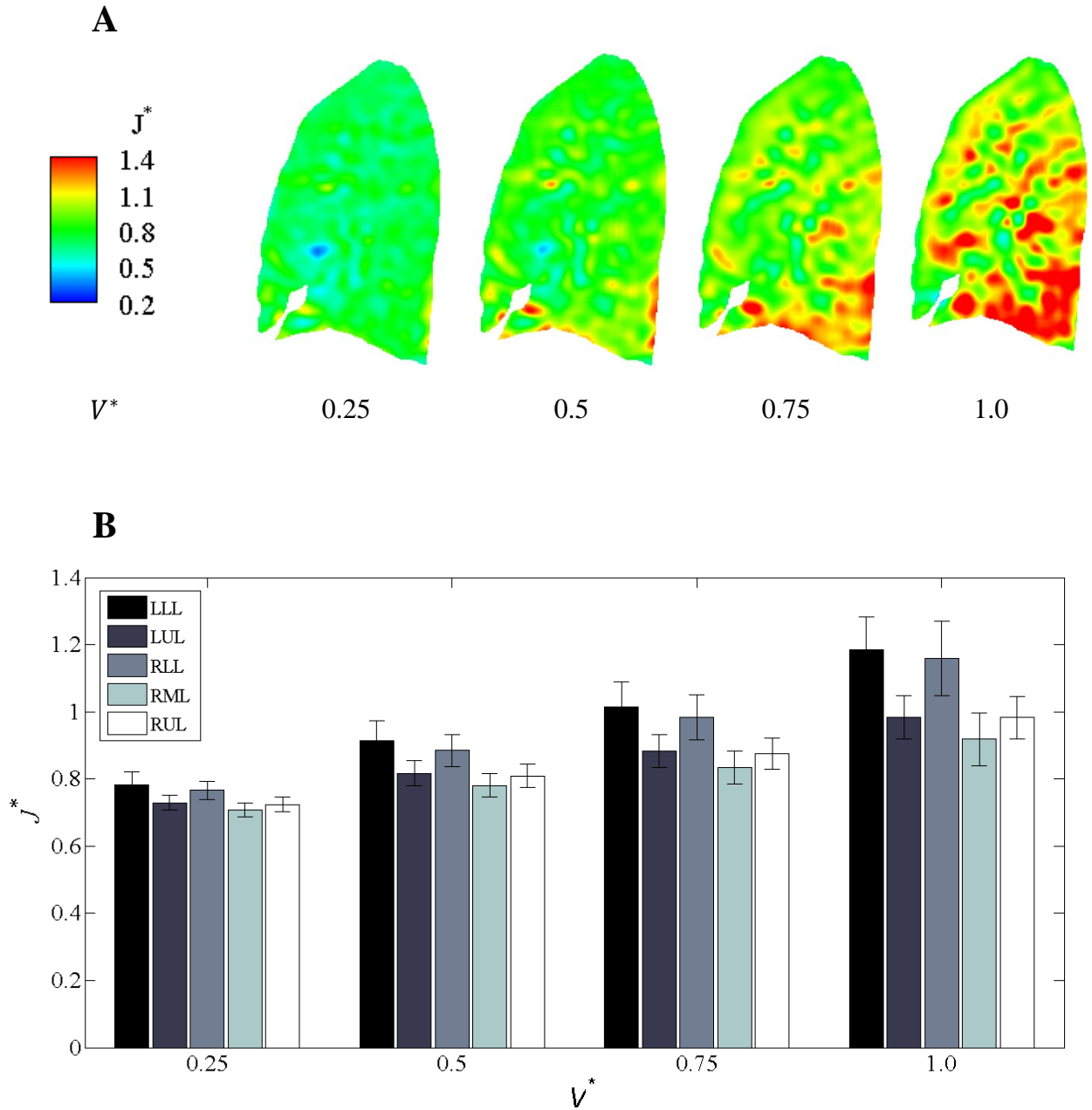
Figure 2.4. Regional normalized Jacobian at different levels. A: Jacobian distribution for a certain subject. B: Bar graph showing lobar Jacobian values. The average and standard deviation show the median of a group of six subjects

A

V^* 0.25   0.50   0.75   1.0

B
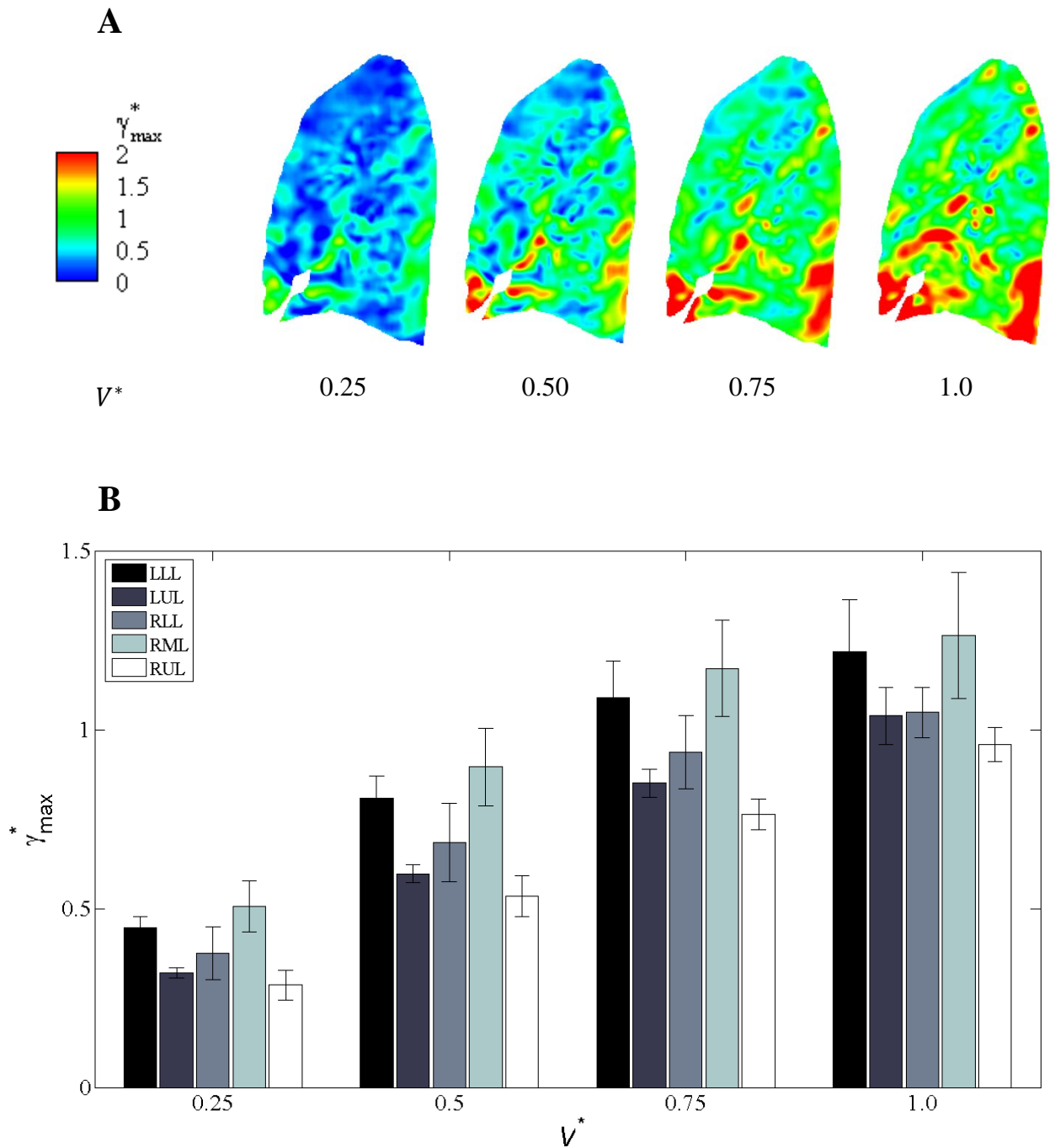
Figure 2.5. Regional normalized shear strain at different levels. A: shear strain distribution for a certain subject. B: Bar graph showing lobar shear strain values. The average and standard deviation show the median of a group of six subjects

A
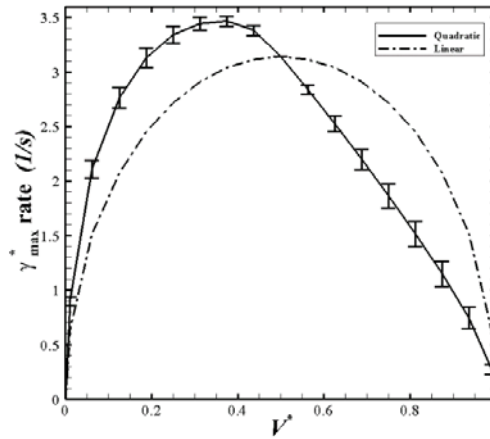
B
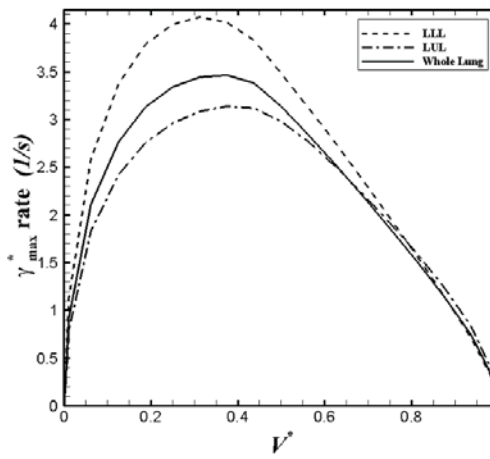
C
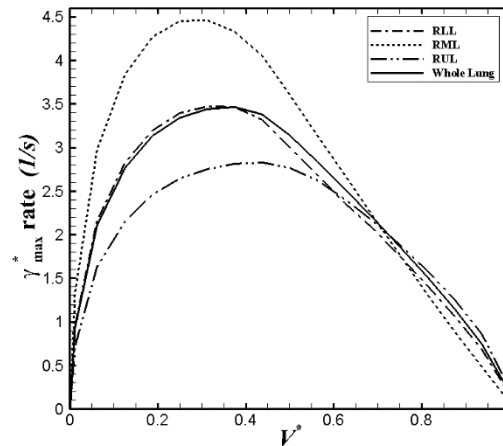
Figure 2.6. Normalized shear rates. A: the whole lung: comparison between linear and quadratic forms. The lines represent the average and standard deviation of the median flow rate of six subjects. B: left lobes C: right lobes

3 ASSESSMENT OF REGIONAL VENTILATION AND DEFORMATION USING 4D-CT IMAGING FOR HEALTHY HUMAN LUNGS DURING TIDAL BREATHING

3.1 Introduction

Precise analysis of lung motion during respiration is essential to study sensitive structure and function relationships at the local level. Several studies have used imaging tools such as magnetic resonance imaging (MRI) ((3), (37)) and single photon emission computed tomography (SPECT) ((61), (84)). The studies have shown regional lung information such as regional ventilation and perfusion to perform physiological evaluation of those imaging modalities. Although MRI is radiation free and SPECT has the ability to analyze ventilation-perfusion, the low resolution and long acquisition time of these imaging techniques limit precise evaluation of lung function and reduce number of examinations. Multi-detector-row computed tomographic (MDCT) imaging equipped with a two-dimensional array of detectors (multiple detector rows) greatly shortens image acquisition time, allowing acquisition of a large number (128 in this case) of slices simultaneously for assessment of detailed structure and function of the lung (7, 10). In applications such as four-dimensional computed tomography (4D-CT) imaging where the travel of the table bed is slowed during spiral acquisitions and the air flow at the mouth is recorded along with the projection images, one can reconstruct the lung volume using only projections from a select portion of the respiratory cycle. By repeating this for many points in the respiratory cycle (gathered in a single spiral acquisition), the result is a four-dimensional (4D) digital representation of the lung. With its advantage of fast acquisition

and more coverage of lung volume, MDCT can be utilized to improve 4D-CT imaging process.

4D-CT dynamic imaging can provide more detailed physiological information of lung motion during tidal breathing. However, in addition to lowered spatial resolution (due to motion and a need to limit radiation dose) compared with static imaging, there are limitations with previous studies due to inconsistencies of tidal breathing during scan acquisition (58). For example, if tidal breaths vary, the actual lung volume varies along the z-axis (apical to basal). This can clearly lead to erroneous physiologic representations. Thus, critical to this process, when seeking to define the mechanical characteristics of the lung, is maintenance of a consistent tidal volume and respiratory rate during scanning. This is critical both for the reconstruction of a meaningful lung volume at each point of the respiratory cycle in a single acquisition and also when seeking to compare subjects and to evaluate regional lung mechanics longitudinally. To resolve this issue, Fuld et al. (23) have devised a dual rolling-seal piston system that maintains the same lung tidal volumes over multiple breathing cycles for wash-in xenon CT studies.

Recent advances in image registration techniques provide accurate matching of local lung volumes, mapping pairs of lung images to a common coordinate system (83). The image registration techniques have been utilized to compute regional lung deformation and ventilation (1, 7, 23). For example, Yin et al. (80) have used a (tissue) mass preserving non-rigid registration method (83) to match two static MDCT images to compute lung deformation and regional ventilation. Later, Yin et al. (81) have proposed a method to derive nonlinear characteristics of lung deformation in three static MDCT images. Jahani et al. (41) then have compared regional lung mechanics between two and three static

images to analyze lung motion at different inflation levels. Unlike the two image-based method, the three image-based method was able to capture non-linear characteristic of lung deformation. However, static image-based analysis could not capture asymmetric physiologically characteristics and irreversible nonlinearity of the lung motion, so-called hysteresis, between inhalation and exhalation. In order to assess those characteristics, image registration methods also have been applied to the 4D-CT volumetric images to estimate continuous displacement fields of a lung and to derive more sensitive local functional variables during dynamic breathing. For example, Christensen et al. (15) have applied image registration to a few selected lung slices (i.e. not the whole lung) acquired at limited breathing cycles. They have demonstrated a strong correlation between the lung motion evaluated by image registration and the change of air volume measured by spirometry. Boldea et al. (5) have introduced new parameters based on trajectories of material points in the 4D-CT images over exhalation and inhalation to quantify nonlinearity and hysteresis. When comparing motion of tumor volume to healthy tissue, they found that hysteresis motion in the tumor volume is larger. White et al. (74) have applied a lung tissue trajectory model that depends on tidal volume and air flow to registration-processed 4D-CT images to study lung tissue hysteresis. They observed significant differences in hysteresis values between lower and upper lung regions.

The main objective of this study is to derive the displacement fields of image voxels by image registration to assess regional ventilation, lung anisotropic deformation and nonlinearity and hysteresis of anisotropic deformation for healthy human lungs during volume controlled free breathing (VCFB). The novelty of the study is two-fold. First, tidal volumes during dynamic imaging are controlled with a unique dual rolling-seal piston for

accurate image reconstruction that is important for assessment of regional lung functions. Second, displacement fields obtained from registration are used to derive sensitive local variables, such as air volume and flow rate, for assessing regional ventilation and anisotropic deformation index (*ADI*), for quantifying nonlinearity and hysteresis of lung motion. A driving motivation for our work is to use regional lung dynamic flow for improved boundary conditions required for the application of computational fluid dynamics (CFD) to the study of lung function (81). This may potentially lead to a better understanding of particle deposition patterns, shear forces at the airway surfaces, or regional distribution of and clearance of inhaled gases (19, 28, 29). These 4D-CT-derived regional air volume and flow rates are also compared with those estimated by linear or nonlinear assumption in the static scans (41). The comparison allows quantification of the differences between static vs. dynamic breathing. Furthermore, much of the motivation, to date, for assessing lung motion and hysteresis via 4D-CT is based upon the desire to adjust for regional lung motion during radiation treatment planning e.g. by tracking tumor structures (9, 24, 30).

3.2   Methods

3.2.1   *Static and Dynamic Image Acquisition*

Six healthy human volunteers (50% male/female) were recruited for this study. Prior to CT scanning, pulmonary function tests (PFT), including body plethysmography (nSpire Health, Longmont, CO), were performed to obtain preliminary lung volume information, such as total lung capacity (TLC), functional residual capacity (FRC), residual volume (RV), vital capacity (VC), forced vital capacity (FVC) and forced expiratory volume in 1 second (FEV1) in upright body posture. During a CT scanning session, both

static and dynamic MDCT image scans were performed in the supine position for each subject. For static CT (SCT) imaging, accurate breath-hold volumes were achieved by use of a pneumotachometer-controlled device (23). This system uses a balloon occlusion valve that closes when the individual is at the desired percent of their VC. In this study, we targeted 95% VC and 15 % VC approximating TLC and FRC, respectively. This method has been validated to provide strong correlations with the corresponding PFT-based TLC and FRC, being significantly improved over simple coaching methods used at other imaging centers (12). The repeatability of the method has previously been demonstrated from multiple visits relative to breath-hold verbal coaching (38).

For dynamic scans and 4D-CT volumetric reconstruction, a dual rolling-seal piston system (23) was employed to guide the subject's inspiratory and expiratory depths of breathing and subjects were coached to breath at least 12 breaths per minute (bpm) due to scanning limitations. This 12 bpm lower limit is dictated by the scanner rotation speed, the table translation rate and radiation dose limits. Scanning time took approximately one minute to acquire the projection images covering the full apex-to-base extent of the lungs. Tidal depth was set based upon assessment of a comfortable minute ventilation obtained for each subject during PFT as a first approximation. This was then adjusted in the CT facility to accommodate what the subject perceived as a comfortable depth for the desired >12 bpm ventilation rate. Subjects rehearsed breathing through the rolling seal piston device and coached to breath at a consistent, comfortable respiratory rate above 12 bpm. With 5 subjects, we were able to achieve consistent multi-slice MDCT lung volumes between end inhalation (EI) and the end exhalation (EE) for multiple breathing cycles. One subject dropped below this 12-breath limit during scanning. In this case, we were unable

to collect an adequate number of projects for use in reconstruction of each phase of the respiratory cycle. Thus, this subject was eliminated from further analysis. This was the first subject studied and motivated additional coaching prior to scanning in the subsequent 6 subjects leading to scanning success in all of the remaining 5 subjects.

The imaging protocols for acquiring MDCT human lung volumetric images were approved by the University of Iowa Institutional Review Board and the radiation safety committee. For the static and dynamic scanning, a Siemens Somatom Definition Flash dual-source 128-slice MDCT scanner (Forchheim, Germany) was employed. The scanner parameters of scan type, peak voltage, effective current and slice thickness were set to spiral, 120 kV, 75 mAs and 0.75 mm, respectively. Each volumetric data set was acquired at a section spacing of 0.5 mm and a reconstruction matrix of 512×512 using the B35f kernel. A semi-automatic segmentation software, Apollo (VIDA Diagnostics, Coralville, Iowa), was utilized to segment the airways, lungs, and lobes of both static and dynamic images.

Figure *3.1* illustrates the process of lung volume reconstruction at a selected phase. For each subject, 4D-CT volumetric image datasets were reconstructed by the scanner at 8-10 automatically defined phases based upon the signal provided by the turbine-based flow meter recorded together with the projection images. To achieve a greater number of reconstructed phases of the respiratory cycle, there was an option for the user to manually identify additional points within the respiratory cycle. The air volumes obtained from the initial, automatically defined 8-10 phases were used for validation of air volumes assessed by image-matching. The additional reconstructed time points were required for spline interpolation analysis where 8 exhalation and 8 inhalation phases were utilized. Because

the phases at EE (minimum volume) and EI (maximum volume) were common for exhalation and inhalation, there were a total of 14 phases for each breathing cycle.

3.2.2 Average of respiratory cycles

Since the inhalation period, the exhalation period and the tidal volume vary from subject to subject, times (t) in respective inhalation and exhalation phases, and continuous air volumes measured with a flow meter ($V_{air,m}$) were normalized as follows:

$$t_{in}^{*n} = \frac{t-t_{EE}^{n-1}}{t_{EI}^{n}-t_{EE}^{n-1}}; \ t_{ex}^{*n} = \frac{t-t_{EI}^{n}}{t_{EE}^{n}-t_{EI}^{n}}, \text{ where } t_{EE}^{n-1} \leq t \leq t_{EE}^{n} \text{ and } t_{EE}^{0} = 0$$

$$V_{air,m}^{*n}(t^{*n}) = \frac{V_{air,m}(t)-V_{air,m,EE}^{n}}{V_{air,m,EI}^{n} - V_{air,m,EE}^{n}}, \text{ where } t^{*n} = \begin{cases} t_{in}^{*n}, & \text{if } t_{EE}^{n-1} \leq t \leq t_{EI}^{n} \\ t_{ex}^{*n}, & \text{if } t_{EI}^{n} < t \leq t_{EE}^{n} \end{cases}$$

(3.1)

where t_{in}^{*n}, t_{ex}^{*n} and $V_{air,m}^{*n}$ are normalized inhalation time, normalized exhalation time and normalized flow-meter-measured air volume, respectively, at the nth cycle. Thus, $t_{in}^{*} = 0$ (or $t_{ex}^{*} = 0$) corresponds to the beginning of inhalation (or exhalation), and t_{in}^{*n}, t_{ex}^{*n} and $V_{air,m}^{*n}$ all range from 0 and 1. Then, the mean was computed as $V_{air,m}^{*}(t^{*} = t^{*n}) = \sum_{n=1}^{N} V_{air,m}^{*n}(t^{*n})/N$, where N is the total number of cycles, along with its standard error ($\pm$SE). With the normalized mean air volume ($V_{air,m}^{*}$), we obtained the normalized total flow rate at any time point t_{p}^{*} ($Q^{*}(t_{p}^{*})$) using a central finite difference scheme as follows:

$$Q^{*}(t_{p}^{*}) = \left(\frac{dV_{air,m}^{*}}{dt^{*}}\right)_{t_{p}^{*}} \approx \frac{V_{air,m}^{*}\left(t_{p+1/2}^{*}\right)-V_{air,m}^{*}(t_{p-1/2}^{*})}{t_{p+1/2}^{*}-t_{p-1/2}^{*}},$$

(3.2)

where the time interval ($t_{p+1/2}^{*}-t_{p-1/2}^{*}$) is taken as 0.01 in this study.

3.2.3 Image Registration

Given the image density in Hounsfield Unit (*HU*) at position **x**, the air and tissue fractions were estimated by

$$\beta_{air}(\mathbf{x}) = \frac{HU_{tissue} - I(\mathbf{x})}{HU_{tissue} - HU_{air}} \text{ and } \beta_{tissue}(\mathbf{x}) = \frac{I(\mathbf{x}) - HU_{air}}{HU_{tissue} - HU_{air}},$$

$$(3.3)$$

where $\beta_{air}(\mathbf{x})$, $\beta_{tissue}(\mathbf{x})$, $I(\mathbf{x})$, HU_{tissue} and HU_{air} denote air fraction, tissue fraction, CT density, HU of tissue, and HU of air, respectively. HU_{air} and HU_{tissue} were set to -1000 and 55, respectively (31). We employed a mass preserving image registration method to match two CT lung images, one as a reference image and the other as a moving image. A spatial transformation $\mathbf{T}(\mathbf{x})$, was determined to minimize a cost function E, based on the sum of squared tissue volume difference (SSTVD) between two images (83).

$$E = \sum_{\mathbf{x} \in \Omega} \left[v_1(\mathbf{x})\beta_{tissue,1}(\mathbf{x}) - v_2(\mathbf{T}(\mathbf{x}))\beta_{tissue,2}(\mathbf{T}(\mathbf{x})) \right]^2 \qquad (3.4)$$

where v_1 and v_2 are local volumes of the corresponding regions of reference and moving images, respectively.

3.2.4 Registration-derived Variables

For each registration between a pair of CT images, local air volume for the moving image at position $\mathbf{x}$ of the reference image was calculated as

$$v_{air}(\mathbf{x}) = v(\mathbf{T}(\mathbf{x}))\beta_{air}(\mathbf{T}(\mathbf{x})), \qquad (3.5)$$

where v_{air} (or v) is the local air volume (or local volume). We employed TLC of static scan and EE of dynamic scan as reference images. The summation of v_{air} within the whole lung is equal to total air volume of a CT image ($V_{air,CT}$), and the local air volume fraction $v_{f,air}$ is defined as the ratio of v_{air} to $V_{air,CT}$. In addition, local air volume (v_{air}) at dynamic scan was normalized as

$$v_{air}^* = \frac{v_{air} - v_{air,EE}}{V_{air,CT,EI} - V_{air,CT,EE}}. \tag{3.6}$$

Since the measured air volume should be equal to the corresponding CT image-derived air volume, we compared them using linear regression to validate the equality of $V_{air}^* = V_{air,m}^* = V_{air,CT}^*$.

In addition, we employed static CT-based TLC and FRC for $V_{air,CT}$, and corresponding %VC of the TLC and FRC to derive RV and VC in supine position of a subject as follows.

$$\%VC = (V_{air,CT} - RV)/VC \times 100 \tag{3.7}$$

We then computed %VC of each phase with corresponding total air volume of a dynamic scan for $V_{air,CT}$ and the obtained VC and RV using Eq. (3.3.7).

Furthermore, to calculate lung deformation at a local position **x**, we compute the principle strains of lung tissue deformation, λ_i (1), where $\lambda_1 > \lambda_2 > \lambda_3$. We used the principle strains to estimate anisotropic deformation index (*ADI*) as follows

$$ADI = \sqrt{\left(\frac{\lambda_1 - \lambda_2}{\lambda_2}\right)^2 + \left(\frac{\lambda_2 - \lambda_3}{\lambda_3}\right)^2} \tag{3.8}$$

ADI indicates the preferential deformation of local lung volume in one or two directions. In this study, *ADI* was computed from the lung volume at EE and normalized by its maximum value at EI state (*ADI**) for inter-subject comparisons. To quantify nonlinearity of lung motion in dynamic breathing, we defined a new quantity δ_{ADI^*} that is based on the *ADI** difference at a certain phase from the corresponding point on the straight

line between EE and EI. That is, the straight line is expected of linear behaviors, whereas any deviation from the line reflects non-linear behaviors. Similarly, the hysteresis of the lung motion is defined as a function of ADI^* at each point ($Hys_{ADI^*}(\mathbf{x})$) as the absolute difference between the ADI^* values of inhalation and exhalation at the same phases.

$$Hys_{ADI^*}(\mathbf{x}) = |ADI^*(\mathbf{x})_{inhalation} - ADI^*(\mathbf{x})_{exhalation}| \tag{3.9}$$

3.2.5 *Interpolation method*

In this study, we used a cubic spline interpolation method to construct a continuous function of a local variable *s*, such as v_{air} and *ADI* at various V_{air}^* based on those derived from CT images at the discrete phases. The interpolation function is piecewise cubic polynomials for a set of *q+1* phases $\{(V_{air,0}^*, s_0), ..., (V_{air,q}^*, s_q)\}$. The function in each interval $(V_{air,i}^*, V_{air,i+1}^*)$ is defined as

$$s_i(V_{air}^*) = a_i(V_{air}^* - V_{air,i}^*)^3 + b_i(V_{air}^* - V_{air,i}^*)^2 + c_i(V_{air}^* - V_{air,i}^*) + d_i \tag{3.10}$$

where the constructed functions pass through *q+1* control points. This method is twice continuously differentiable and used for inhalation and exhalation separately. Combining the breathing waveform $\left(\frac{dV_{air}^*}{dt^*}\right)$ with interpolated variables (*s*) allowed us to find the time rate of *s* as follows,

$$\frac{ds_i(V_{air}^*)}{dt^*} = \frac{ds_i}{dV_{air}^*}\left(\frac{dV_{air}^*}{dt^*}\right)$$

$$= \left[3a_i(V_{air}^* - V_{air,i}^*)^2 + 2b_i(V_{air}^* - V_{air,i}^*) + c_i\right]\left(\frac{dV_{air}^*}{dt^*}\right) \tag{3.11}$$

For example, to assess regional ventilation, the local normalized flow rate q^*, can be calculated as

$$q^* = \frac{dv^*_{air}}{dt^*} = \frac{dv^*_{air}}{dV^*_{air}} \frac{dV^*_{air}}{dt^*} \tag{3.12}$$

In addition to the measured waveform, we also performed a symmetric sinusoidal waveform ($V^*_{air} = \frac{1}{2}(1 - \cos(\pi t^*))$ for inhalation and $V^*_{air} = \frac{1}{2}(1 - \cos(\pi(1 - t^*)))$ for exhalation) to evaluate the effect of waveform on regional flow rate and on inter-subject variability. Furthermore, the flow rate fraction (q_f) in each region is defined as the flow rate in that region over total flow rate. In dynamic analysis, q_f is computed as follows.

$$q_f = \frac{q^*}{Q^*} = \frac{dv^*_{air}}{dV^*_{air}} \tag{3.13}$$

It is noted that q_f is independent from the waveform. In two static images, q_f is equivalent to the ratio of local air volume change to total air volume change ($\Delta v_{air}/\Delta V_{air,CT}$), so it could be used for CFD boundary condition if only two CT images are available (80). The flow rate fraction q_f is mainly used to compare the distributions of air volume changes derived from dynamic vs. static scans.

Furthermore, all the variables plotted in the result section were derived from their corresponding continuous functions, but we only plotted a certain number of SE for clarity.

3.3 Results

3.3.1 Reliability of dynamic lung volume controller system

Demographic information and PFT data of the six healthy subjects are shown in Table *3.1*. The percent predicted values of the six subjects indicates that the measurements

were within normal ranges ((29), (67)). Meanwhile, 4D-CT analysis was performed for the five subjects for whom we were able to reconstruct volumetric image data sets. As discussed in the methods, the respiratory rate of Subject 1 fell below 12 breaths per minute, limiting our ability to reconstruct volumetric image data. Figure *3.2A* and *B* show $V_{air,m}^*$ (±SE) for exhalation and inhalation for Subject 6. For all subjects, the SEs of the means were less than 4% between all the cycles. The results indicate that the dual piston-based volume controller adequately maintained consistent tidal volumes over multiple breathing cycles. It was this consistency that provided for the consistent trends shown in the data across all five subjects.

3.3.2   *Total lung volume and flow rate*

Based upon data acquired at the time of imaging, Table *3.2* shows the actual %VC achieved for the inspiratory and expiratory breath holds (TLC and FRC) in the supine body posture and the corresponding air volumes for these two breath holds along with the air volumes achieved for EI and EE of the 4D-CT scans of the five subjects. Table *3.2* also indicates the supine RV, VC, %VC of EI and EE estimated by Eq. (3.3.7). TLC, FRC and RV in Table *3.2* show strong correlations with those volumes obtained from PFT shown in Table *3.1* ($R^2 > 0.89$). While %VCs of EI and EE show large standard deviations of 14-15% among different subjects, the difference of %VC between EI and EE (viz. %VC of tidal volume) has a standard deviation of 6% (Table *3.2*).

Figure *3.3* shows the means (±SE) of normalized total flow rate Q^* for the five subjects during exhalation (positive values) and inhalation (negative values). The Q^* for each subject was used to calculate the normalized regional flow rate q^* by Eq. (3.3.12). To validate registration results, approximated values for normalized air volumes from the

measurement ($V_{air,m}^*$) were compared with the corresponding air volumes in the whole lungs derived from image registration ($V_{air,CT}^*$). Since we compared the data at 8-10 phases automatically selected by the scanner, there were 42 data points. The comparisons for the five subjects are plotted in Figure *3.4*, demonstrating that $V_{air,CT}^*$ is significantly correlated with $V_{air,m}^*$ for the five subjects ($R^2 \approx 0.98$). Thus, it validates the assumption of $V_{air}^* = V_{air,CT}^* = V_{air,m}^*$.

3.3.3   *Local air volume and flow rate*

Figure *3.5* illustrates the mean (+SE) of lobar air volume fraction $v_{f,air}$ during inhalation and exhalation for the five subjects. As the lung volume increases, $v_{f,air}$ in the lower lobes increase while those in the upper and the middle lobes decrease. In addition, $v_{f,air}$ values at EE ($V_{air}^* = 0$) and at EI states ($V_{air}^* = 1$) for both the lower and upper lobes are significantly different in VCFB range ($P<0.005$).

In regard to regional ventilation, **Figure *3.6*A** and *B* exhibit the mean (+SE) of medians q^* in each lobe as a function of V_{air}^* calculated using Eq. (3.3.12) for exhalation and inhalation, respectively. The results show that the q^* values of the lower lobes always remain greater than those of the upper and the middle lobes during breathing. Next, to evaluate the effect of the waveform on asymmetric patterns of regional flow rates and on inter-subject variability, instead of the measured waveforms, we imposed an ideal symmetric sinusoidal waveform to compute q^* for all subjects. Figure *3.6*C and D demonstrate the mean (+SE) of the medians of lobar q^* at which the overall trends of q^* remain similar with those using the measured waveform, and further inter-subject variability does not vary significantly (mean of SE decrease from 24% to 23%). While the

sinusoidal waveform provides the same notion that $q*$ of the lower lobes is greater than that of the upper and the middle lobes, the values and peak location of the sinusoidal waveform are different from those in the measured waveform, and asymmetric pattern between inhalation and exhalation is reduced (Figure *3.6*)

3.3.4 *Comparison of tidal and deep breathing (dynamic and static scans)*

We compared air volume changes obtained from 4D-CT at VCFB with those obtained from SCT at deep breathing to see how deep breathing analysis is able to estimate regional ventilation in VCFB range in the case that 4D-CT image data are not available. Linear interpolation (like Eq. (3.3.10) where a_i and b_i equal zero) of lobar v_{air} from FRC to TLC for SCT gives a constant flow rate fraction q_f equivalent to lobar air volume difference over total air volume difference ($q_{f,SCT} = \frac{\text{Lobar } \Delta V_{air,CT}}{\text{Total } \Delta V_{air,CT}}$). We compared $q_{f,SCT}$ with the average of flow rate fractions of 4D-CT obtained from Eq. (3.) ($\overline{q_{f,4D-CT}}$). Figure *3.7A* shows the linear regression between $q_{f,SCT}$ and $\overline{q_{f,4D-CT}}$ in all lobes for the five subjects, indicating good correlation ($R^2 \approx 0.84$).

However, the comparison of q_f in the left lungs (LL) with q_f in the right lungs (RL) for the five subjects indicates that in deep breathing, the contributions of the left and the right lungs in air volume change are almost the same ($q_{f,LL}= 0.492$, $q_{f,RL}= 0.508$) while in VCFB, the average contribution of the right lung in air volume change is significantly ($P < 0.05$) greater than that of the left lung ($\overline{q_{f,LL}}=0.449$, $\overline{q_{f,RL}}= 0.551$). In addition, means of air volume fractions in the lower lung volumes (FRC, EE and EI) are $0.56 < v_{f,air} < 0.58$ for the right lung and $0.42 < v_{f,air} < 0.44$ for the left lung, while the air volume fraction at full inspiration (TLC) was 0.53 ± 0.02 for the right lung and 0.47 ± 0.02 for

the left lung. Since inter-subject variability of q_f is small (SE $<$ %2), we can compute flow

rate fraction of the left and the right lungs at tidal breathing from deep breathing analysis

with two correction weighting factors of $W_{left} = \frac{0.449}{0.492} = 0.913$ and $W_{right} = \frac{0.551}{0.508} =$

1.085, respectively for the all subjects. Therefore, to predict q_f during VCFB range more

accurately, we assume that W_{left} and W_{right} can be multiplied by q_f in any region of the

left and right regions computed by the deep breathing analysis, respectively. **Figure *3.7B***

shows the linear regression between $\overline{q_{f,4D-CT}}$ and $q_{f,SCT}$ modified by W_{left} and W_{right}

(denoted by $q_{f,modified}$). In this case, the correlation factor R^2, was improved from 0.84 to

0.92 so that we can roughly use the equations $(q_{f,modified})_{left} = (q_{f,SCT})_{left} \times W_{left}$ and

$(q_{f,modified})_{right} = (q_{f,SCT})_{right} \times W_{right}$ to predict air volume change during VCFB. A

comparison between original and modified values of the left and right lungs showed that

they are significantly different ($P < 0.05$).

Furthermore, the comparison of the left and right lungs for *ADI* of FRC-TLC

normalized by total *ADI* at TLC ($ADI^*_{LL} = 1.02$, $ADI^*_{RL} = 0.97$) and *ADI* of EE-EI

normalized by total *ADI* at EI ($ADI^*_{LL} = 0.87$, $ADI^*_{RL} = 1.19$) illustrates consistency with

the left-right lung differences observed by air volume changes in each left and right lungs.

3.3.5   Nonlinearity and hysteresis of ADI

To observe nonlinearity and hysteresis of the lung motion during dynamic breathing,

we examined *ADI** values during VCFB. Figure *3.8A* shows that the means ($\pm$SE) of *ADI**

values in the whole lung at different V^*_{air} over a breathing cycle for the five subjects. The

results showed that *ADI** values are not along a straight line and the values of inhalation

are greater than those of exhalation ($P < 0.05$), capturing nonlinear and asymmetric lung

deformations between two certain points (EE and EI). In Figure *3.8B,* we also observed greater ADI^* values for the right lung rather than the left lung. Figure *3.9A* and *B* show the lobar distributions of ADI^* over exhalation and inhalation, respectively. We observed that ADI^* values in the middle and the lower lobes are greater than those in the upper lobes for both exhalation and inhalation. We further quantified the nonlinearity δ_{ADI^*}. Figure *3.9C* and *D* show that δ_{ADI^*} in inhalation is greater than that of exhalation, and lower and middle regions represent greater δ_{ADI^*}. Furthermore, Figure *3.10* shows mean and maximum of Hys_{ADI^*} in the whole lung, the left and the right lungs and each lobe for different phases. The results demonstrate that the right lung has greater Hys_{ADI^*} than the left lung ($P < 0.05$).

3.4 Discussion

3.4.1 *Controlled tidal volume*

The limitations of inconsistent tidal volumes and irregular breathing patterns during 4D-CT have been recognized by others ((5), (15), (58)). The amplitude difference produces artificial motions in the reconstructed 4D volumetric CT data set, leading to erroneous assessment of regional mechanical behavior. With the introduction of a dual rolling-seal piston system (23) for control of tidal breathing during 4D-CT data collection we presented a means of regionally assessing lung mechanics that provides physiologically meaningful metrics. The results demonstrated that the dual-piston system successfully controlled the subject's respiratory cycle to obtain consistent air volume change and breathing waveforms (SE < 4%), thus allowing for the collapse of multiple-cycle data into a single cycle (Figure *3.2A* and *B*). To further harmonize subject data, air volumes derived from registration were normalized utilizing measurements via the same scheme as discussed in Eq. (3.1) and Eq. (3.6). The strong correlation between the measured air volume and the

air volume computed by image registration not only validates the accuracy of 4D-CT data, but also enables use of a single normalized air volume for analysis of measurement and 4D-CT data. Because of inter-subject variability in respiratory waveforms, other studies had to examine each subject separately ((15), (74)). In contrast, with use of a dual-piston system, we were able to derive consistent normalized flow rates and lobar air volume fractions during inhalation and exhalation in a group of healthy subjects (Figure *3.3* and Figure *3.5*). This is particularly important for future studies that seek to define phenotypes based upon altered regional mechanical properties in a patient population.

3.4.2   *Regional air volume and flow rate*

Several studies used linear assumption between each two successive phases to estimate 4D-CT lung motion ((5), (15)). Piecewise linear interpolation yields discontinuity in calculation of air flow rate at each phase while, in the present study, we used a cubic spline interpolation function to construct a continuous function for any local variable, which is independent of breathing waveform. Regional air volume and flow rates obtained from 4D-CT analysis showed that lower lobes always have more contribution to air volume change compared with upper and middle lobes during dynamic breathing (Figure *3.5* and Figure *3.6*). This supports the analysis of Yin et al. (81) and Jahani et al. (41) based on interpolation of three static MDCT images. It is speculated the predominance of diaphragm motion in driving lung expansion leads to the greater volume change in the lower lobes than the upper lobes.

Furthermore, since the interpolated function is independent of lung volume waveforms, it can be incorporated with any other lung volume curve for various

waveforms. Thus, if measured temporal lung volume curves are not available, an ideal lung volume waveform can be assumed to compute local air flow rates (Eq. 3.3.12) for various respiratory condition. For example, in order to examine the effect of waveform, we replaced the actual waveform with a sinusoidal one. Although, the results showed similar trends when using a symmetric waveform, asymmetric patterns of local flow rates (Eq. 3.) of exhalation and inhalation were reduced (Figure *3.6*).

3.4.3   *Regional tidal vs. deep breathing (dynamic vs. static scans) flow rate*

Several studies have utilized static scans acquired at static points to evaluate regional lung ventilation and deformation ((31), (41), (80)). Although 4D-CT images can provide more physiological information, they typically yield lower spatial resolution compared with static imaging and expose subjects to higher radiation doses. Newer generation CT scanners are serving to dramatically drop radiation doses (56). Because of the need for high resolution acquired with lower radiation doses, lung mechanics studies have typically been carried out with static breath hold imaging. Our study provides, possibly for the first time, a means of comparing the mechanical data derived from breath hold vs. dynamic imaging and provides a methodology which, when coupled with newer methods for low dose imaging, can provide important dynamic regional lung mechanics which, in the future, can be used as novel phenotypes, differentiating populations at early stages of lung disease. In some studies, FRC and TLC data (instead of end tidal lung volumes) have been used to derive mean flow rate fraction, equivalent to the fractions of lobar air volume change ((13), (80)). Our comparisons between tidal breathing (4D-CT) vs. static imaging at FRC and TLC demonstrated that fractions of lobar air volume change across lung volumes are in good correlation with the flow-rate fractions in 4D-CTs

(Figure *3.7A*). This suggests that, in normal subjects, static breath-hold derived metrics may be adequate for certain lung mechanics studies. However, we found that during VCFB the air volume change fractions in the right lung is greater than that of the left lung, while the air volume change fractions of both lungs derived from static FRC and TLC images are almost the same, consistent with findings of Voorhees et al. (71). Since the left lung was less well expanded at lower lung volumes and during VCFB, it is able to expand more than the right lung when inspiring to full lung capacity, equalizing lung volume changes between the two lungs at TLC while at tidal breathing, one observes differences in distribution of lung volume changes. Flow rate fractions for the left and right lungs, between VCFB and deep breathing, are significantly different where respective values for the five subjects were similar with small standard errors (SE < 2%). Therefore, we proposed two correction weighting factors $W_{left} = 0.913$ and $W_{right} = 1.085$, which were multiplied by mean flow rate fractions, i.e. air volume change fractions, obtained from the SCT analysis in left and right lungs, respectively. The improved correlation implies that the proposed correction factors could be utilized to estimate regional ventilation predictions (Figure *3.7*B). Yin et al. (80) have proposed an image-based technique using two static CT lung datasets to estimate a subject-specific boundary condition for CFD simulation. Thus, those two correction factors can be employed in their method to estimate more realistic boundary conditions for CFD simulation in tidal breathing range.

Yin et al. (81) and Jahani et al. (41) have used 3 static images to study non-linear behaviors of lung mechanics with a sinusoidal waveform. They showed that, as lung volume increases for a deep breathing, the peaks of flow rate occur earlier in the upper

lobes than the peaks in the lower lobes while our dynamic breathing analysis with the assumption of a sinusoidal waveform did not show any ascending or descending trend in lobar flow rate fractions (Figure *3.6*). One reason is that most regions in the upper lobes are fully inflated before the lung volume reaches its maximum volume, while the upper lobes in VCFB still have capacity to accommodate more air at the maximum volume of EI because of lower lung volume. In addition, acquiring 4D-CT data can allow assessment of regional flow volume loop that is asymmetric between inhalation and exhalation. In contrast to 4D-CT analysis, two static scans can provide only constant flow rate, and three static scans can provide a nonlinear but symmetric volume-dependent flow rate between inhalation and exhalation (81).

3.4.4   Nonlinearity and hysteresis

In this study, *ADI* was used to quantify nonlinearity and hysteresis in lung deformation during VCFB. Our results indicated that *ADI* and nonlinearity are greater in inhalation, being consistent with the parameters of anisotropic deformation and nonlinearity quantified by Jahani et al. (41) and Boldea et al. (5), respectively. Our observations may reflect the fact that the diaphragm and chest wall muscles are typically active only during inhalation, producing greater directional forces than occur during passive exhalation. It is noted that Boldea et al. (5) have used trajectories of material points to quantify nonlinearity. They assumed that local points have uniform motion relative to total volume change over inhalation and exhalation, while our study showed that local points might move non-uniformly relative to the motion of normalized total lung volume. Similar to point trajectory, *ADI* is a Lagrangian quantity obtained via the registration-derived one-to-one mapping field.

Physiologically, the hysteresis of lung motion is attributed to the fact that some part of the transmitted energy in inhalation is dissipated due to local forces such as surface tension and tissue stress and is not recovered in exhalation (42). Locally, those forces are correlated with strains. For example, Jahani et al. (41) have used shear strain expressed as $(\lambda_1 - \lambda_3)/2$ to quantify nonlinearity in the lung and have demonstrated a strong correlation between shear strain and *ADI* ($R^2 > 0.89$), being consistent with our results. The significant difference between *ADI* values on inhalation and those on exhalation suggests that anisotropic deformation can be used to assess the hysteresis of lung motion. The computed hysteresis showed the maximum value at the middle of breathing and greater hysteresis in the right lung (Figure *3.8* and Figure *3.10*).

3.4.5 *Limitations and future work*

In this study, we investigated 4D-CT analysis for only five healthy subjects while more subjects are needed to fully define the characteristics of a normal population. Nonetheless, we performed t-test between different regions (e.g. lower vs. upper lobes, left vs. right lung, and inhalation vs. exhalation) to assure that the reported characteristics are statistically significant. With P<0.05, the heterogeneous pattern of lung characteristics are confirmed. Furthermore, in order to evaluate inter-subject variability, means and standard errors between the five subjects were reported for all variables. To achieve more subjects we need to resolve the remaining issues such as imaging protocol and limitation in breathing rates and it will be desirable to identify lower dose protocols, taking advantage of newer scanner technologies (56). In addition, application of the current analysis to disease states, such as asthma, chronic obstructive lung disease, and interstitial fibrosis is desirable because heterogeneity in diseased lungs may pose new challenges on

normalization of inter-subject data ((13), (11)). Several studies have applied CFD to simulate respiratory air flow in a breathing lung based on static-image derived flow boundary conditions ((48), (81)). The regional air flow distributions and flow rates extracted from the current 4D-CT analysis can be further used in CFD to better predict the distributions of flow-induced shear stress and pressure as well as temperature, water loss rate ((76), (77) and particle depositions (52) for various applications. In addition, using the methods in this study for tracking the motion of lung cancers could provide more accurate information regarding lung motion required for the targeting of radiotherapy and for the assessment of regional, longitudinal changes in lung mechanics throughout therapy ((2), (5), (16), (79)).

Table 3.1. Demographic information[*] and PFT values (% predicted normal values) for the six subjects

Subject	1	2	3	4	5	6
Gender	F	F	M	F	M	M
Age (yrs.)	24	44	23	39	53	58
BMI (kg/m²)	25	26	26	24	30	32
FEV1 (L)	3.3 (99 %)	2.6 (95 %)	3.7 (91 %)	3.0 (97 %)	3.5 (87 %)	3.4 (83 %)
FVC (L)	4.1 (105 %)	3.4 (101 %)	4.6 (95 %)	3.6 (97 %)	4.6 (86 %)	4.4 (82 %)
FEV1/FVC	0.806	0.762	0.813	0.818	0.774	0.768
TLC (L)	4.8 (93%)	4.5 (99%)	5.4 (87%)	5.2 (104%)	6.6 (88%)	7.2 (93%)
FRC (L)	2.1 (76%)	2.2 (85%)	1.9 (71%)	2.8 (102%)	2.9 (79%)	2.9 (78%)
RV (L)	1.0 (73%)	1.1 (73%)	0.9 (69%)	1.5 (97%)	2.1 (90%)	2.3 (93%)
RV/TLC	0.209	0.249	0.157	0.296	0.315	0.318

*: All subjects are white non-Hispanic except subject 4 that is white Hispanic. F: female; M: male.

Table 3.2. Lung volume information at the TLC, FRC, EI and EE states for the five subjects

Subject	2	3	4	5	6	Average	SD
%VC from measurement							
TLC	92.7%	91.6%	88.2%	95.3%	89.9%	92%	3%
FRC	15.8%	13.3%	16.2%	11.5%	13.4%	14%	2%
CT lung volume (L)							
TLC	4.73	5.19	5.31	6.82	7.77	5.96	1.28
FRC	2.41	2.21	2.87	3.34	3.69	2.90	0.62
EI	3.84	2.96	3.46	5.42	5.99	4.33	1.31
EE	3.69	2.08	2.67	4.56	4.88	3.58	1.20
Volume (L) From Eq. (3.3.7)							
RV	1.93	1.70	2.32	2.86	2.97	2.35	0.56
VC	3.02	3.81	3.38	4.15	5.33	3.93	0.88
%VC from Eq. (3.3.7)							
EI	63.2%	33.1%	33.7%	61.7%	56.5%	50%	15%
EE	28.5%	9.9%	10.3%	40.9%	35.8%	25%	14%
EI-EE	34.7%	23.2%	23.4%	20.8%	20.7%	25%	6%
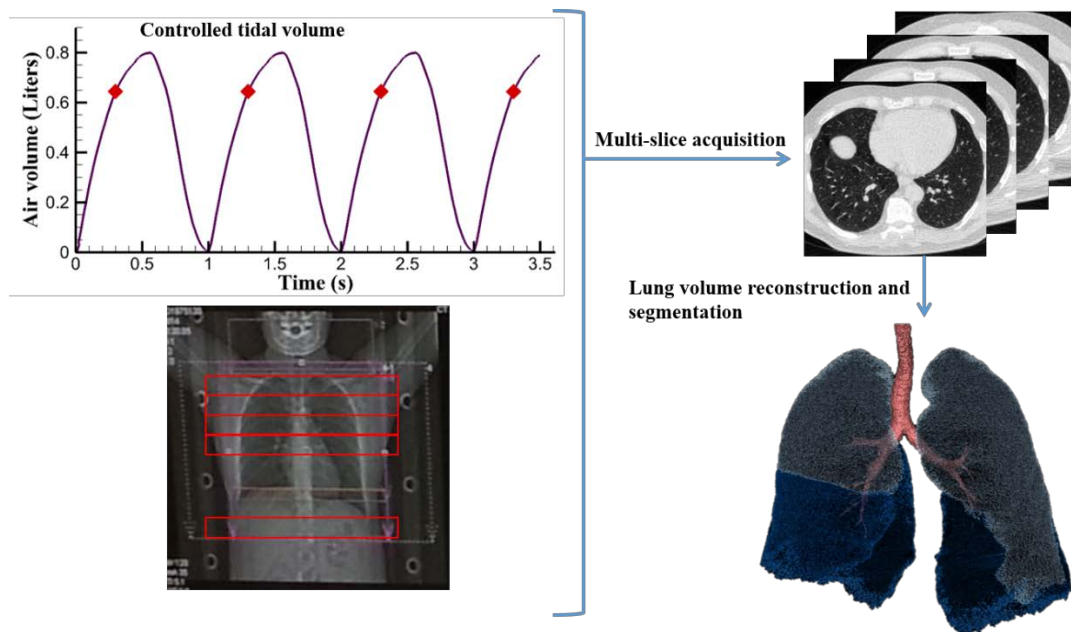
Figure 3.1. A flow chart of lung volume reconstruction process at a certain phase

A

B
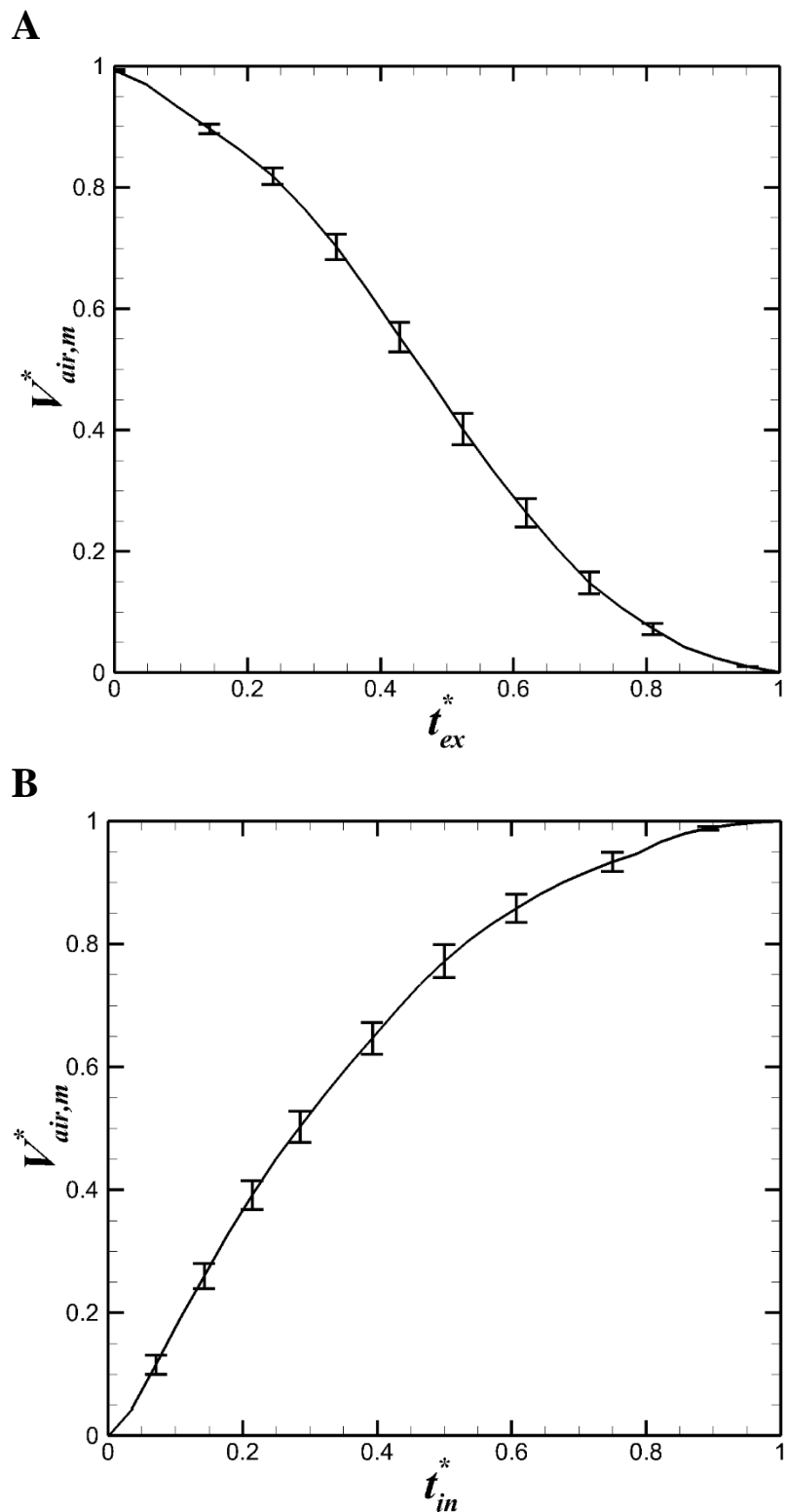
Figure 3.2. Normalized air volume (±SE) for (a) exhalation and (b) inhalation for Subject 6
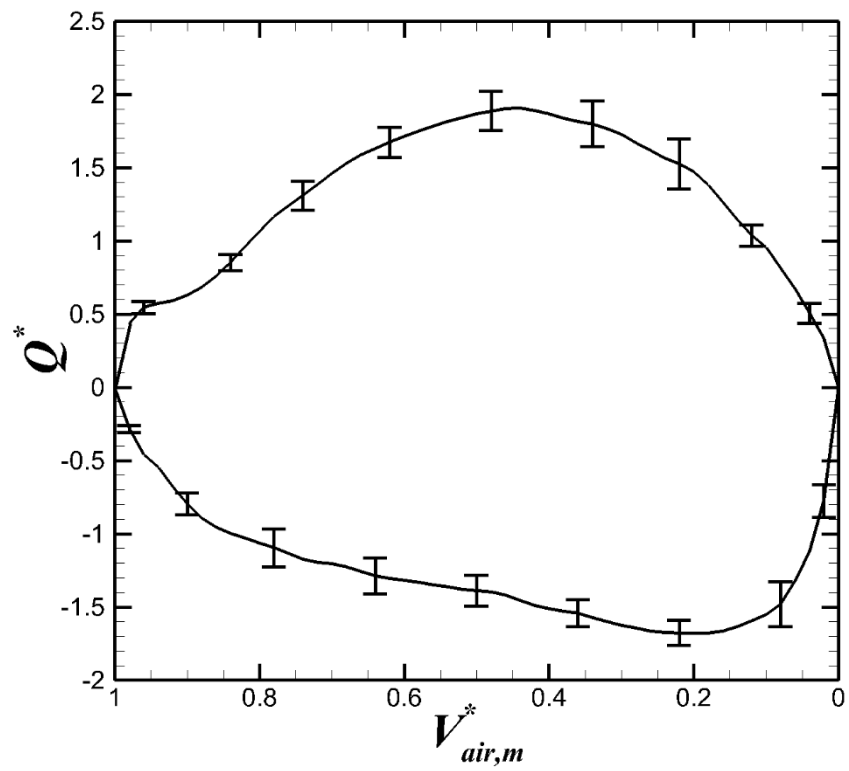
Figure 3.3. Means (±SE) of normalized flow rates obtained from measurement for exhalation (+) and inhalation (-) in the whole lung for the five subjects
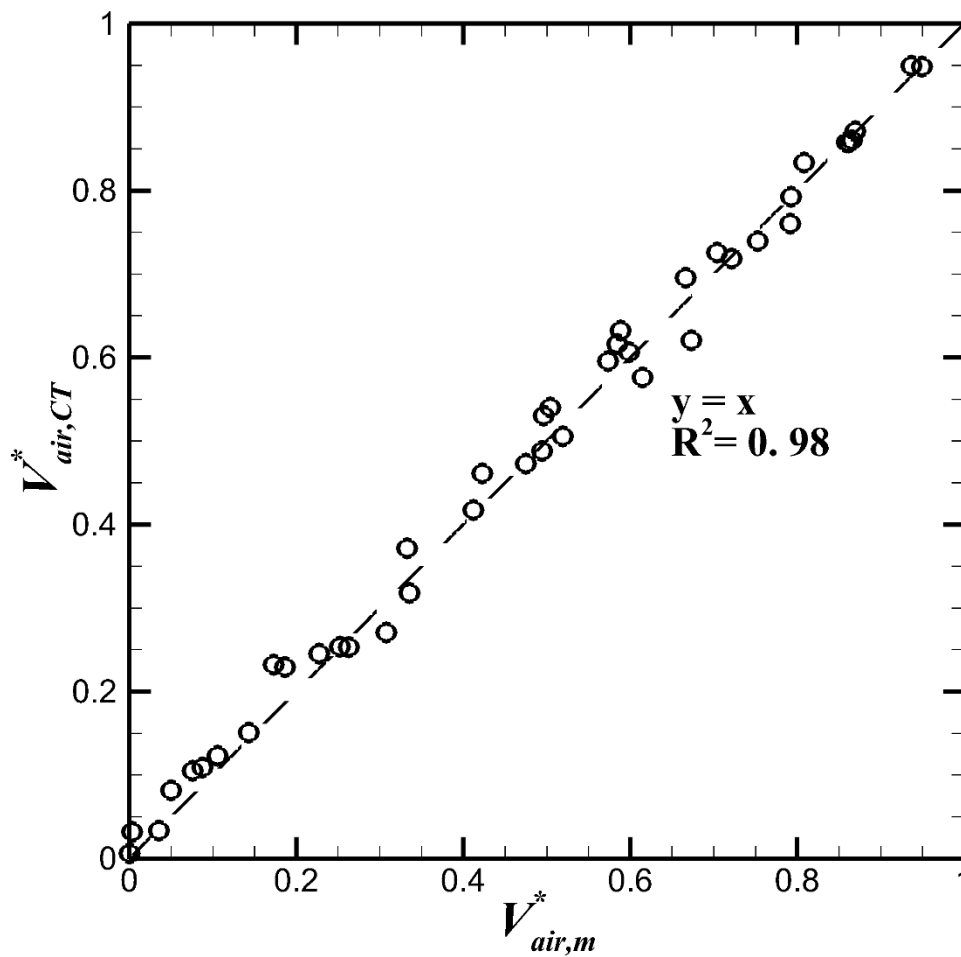
Figure 3.4. Linear regression between normalized measured air volume and normalized registration-derived air volume for the five subjects

A

B
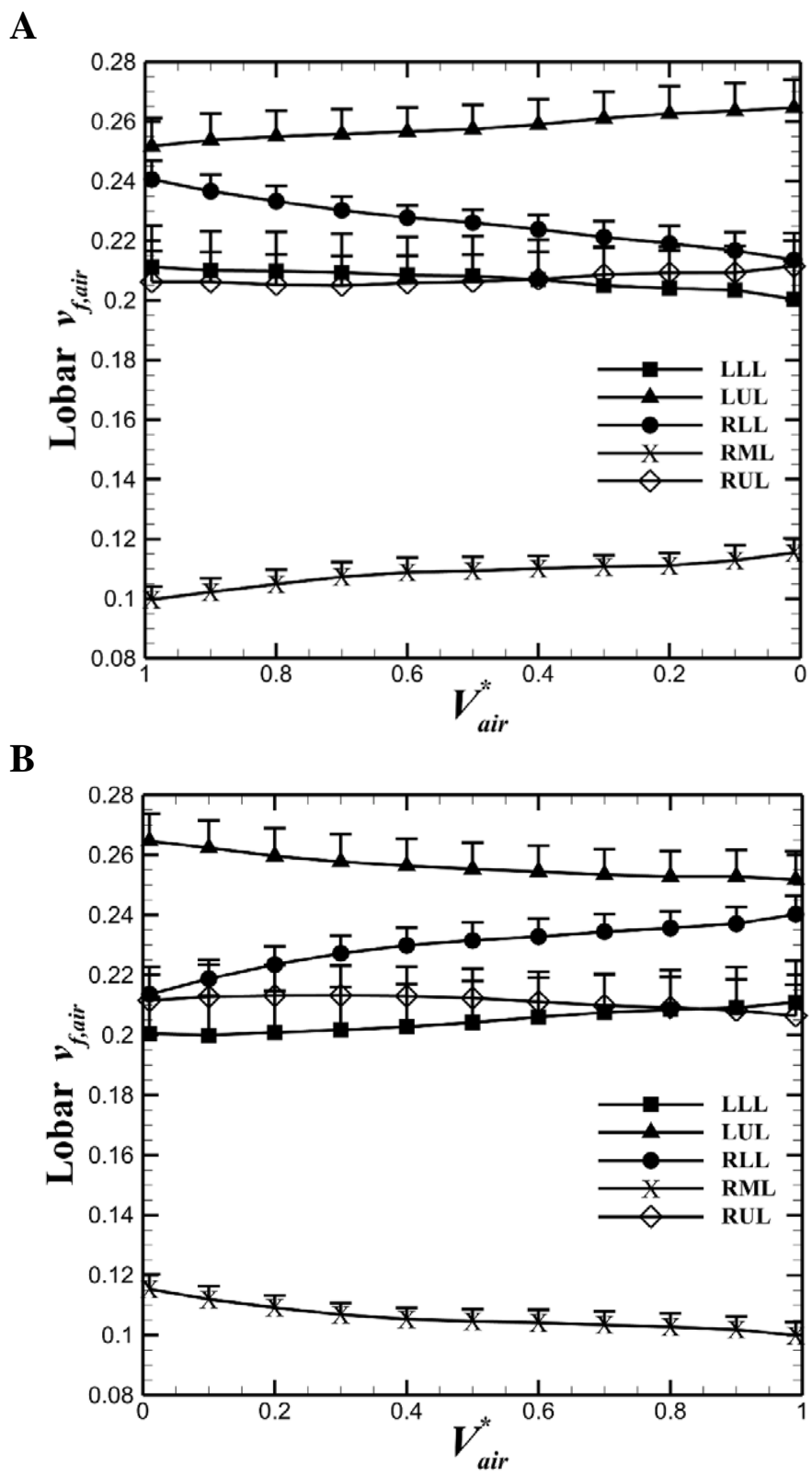
Figure 3.5. Mean (+SE) of lobar air volume fraction during (a) exhalation and (b) inhalation for the five subjects. [(LLL, LUL, RLL,RML,RUL) =(left lower lobe, left upper lobe, right lower lobe, right middle lobe, right upper lobe)]

A

B

C

D
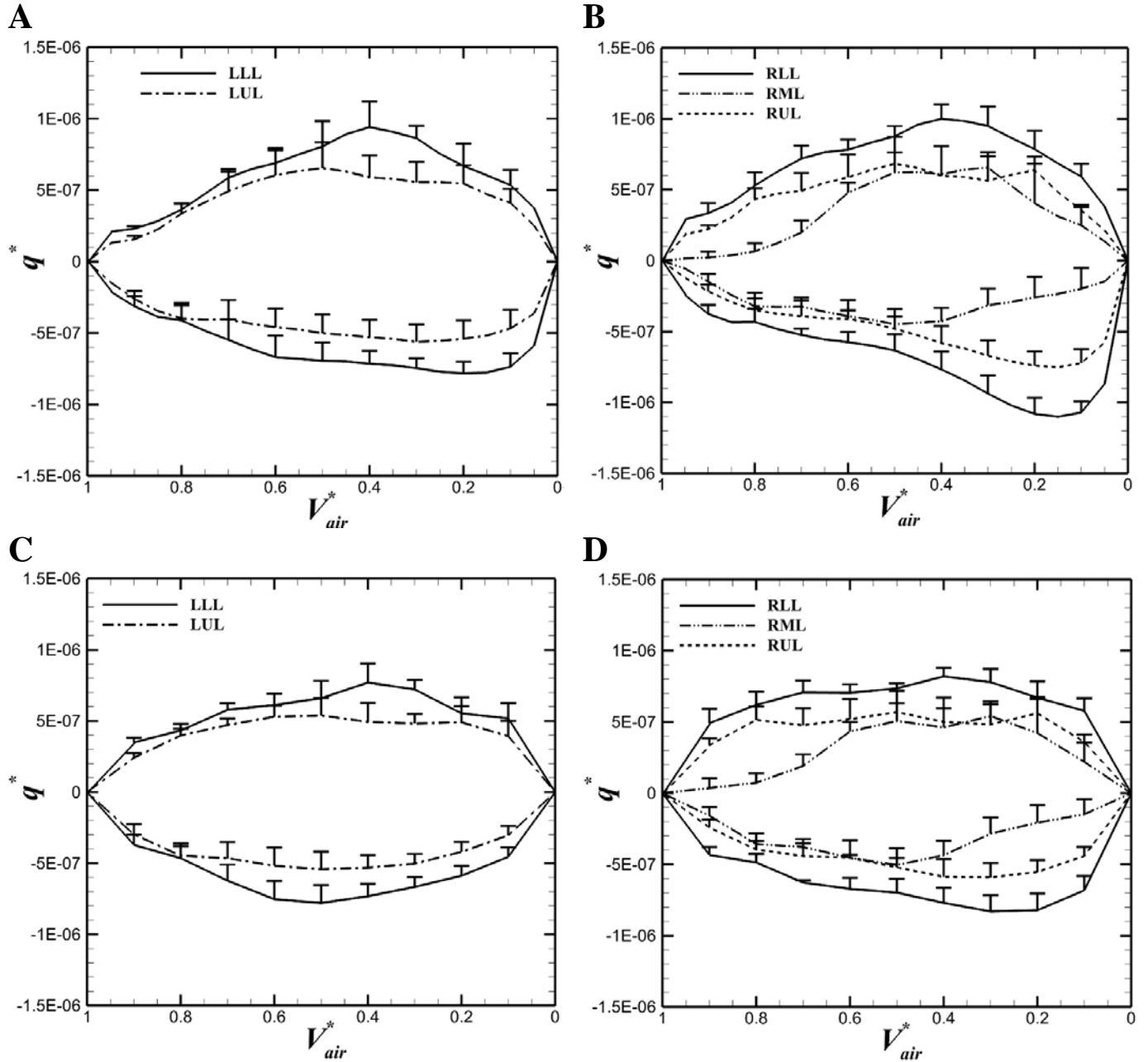
Figure 3.6. Mean (+SE) of median of lobar flow rate during exhalation (+) and inhalation (-) for the five subjects: Plots correspond to results using measured waveform for (a) the left lobes and (b) the right lobes, and using sinusoidal waveform for (c) the left lobes and (d) the right lobes

A

B
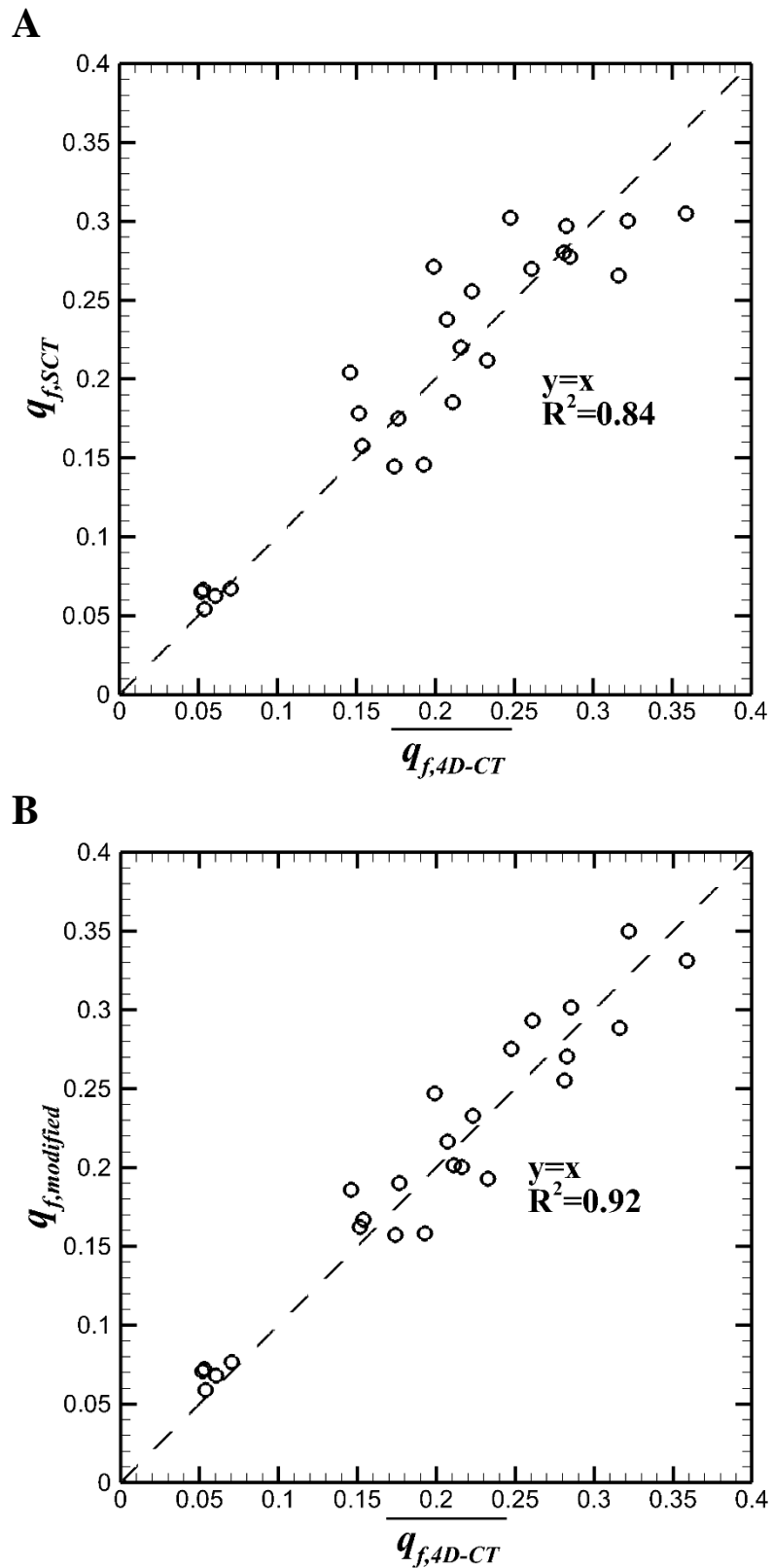
Figure 3.7. Linear regression (a) between lobar q_f of static images (FRC-TLC) and average q_f of dynamic (EE-EI) (b) between lobar average q_f of dynamic (EE-EI) and q_f modified from static images (FRC-TLC) for the five lobes of the all five subjects

A
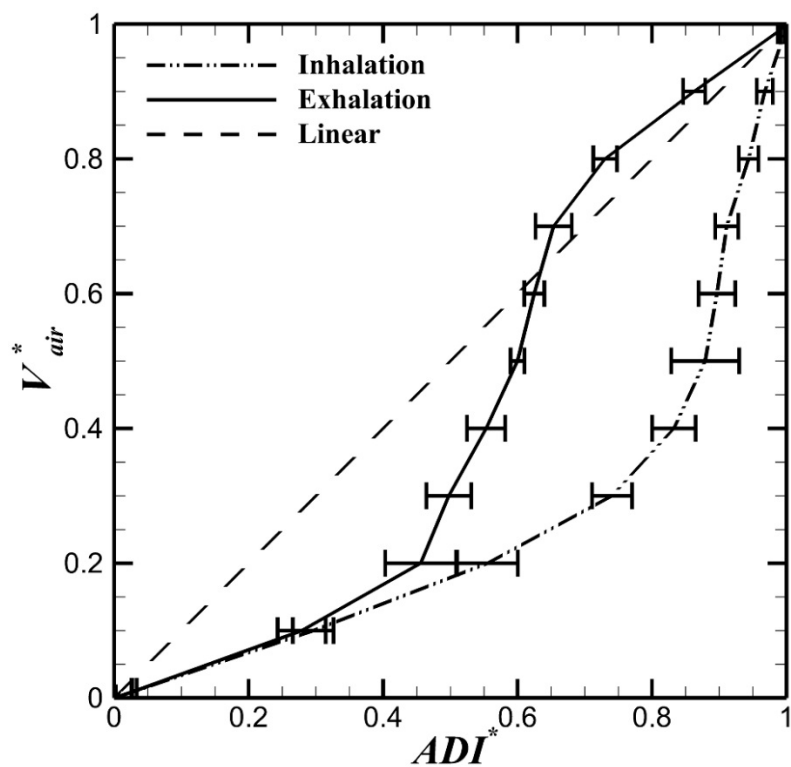
B
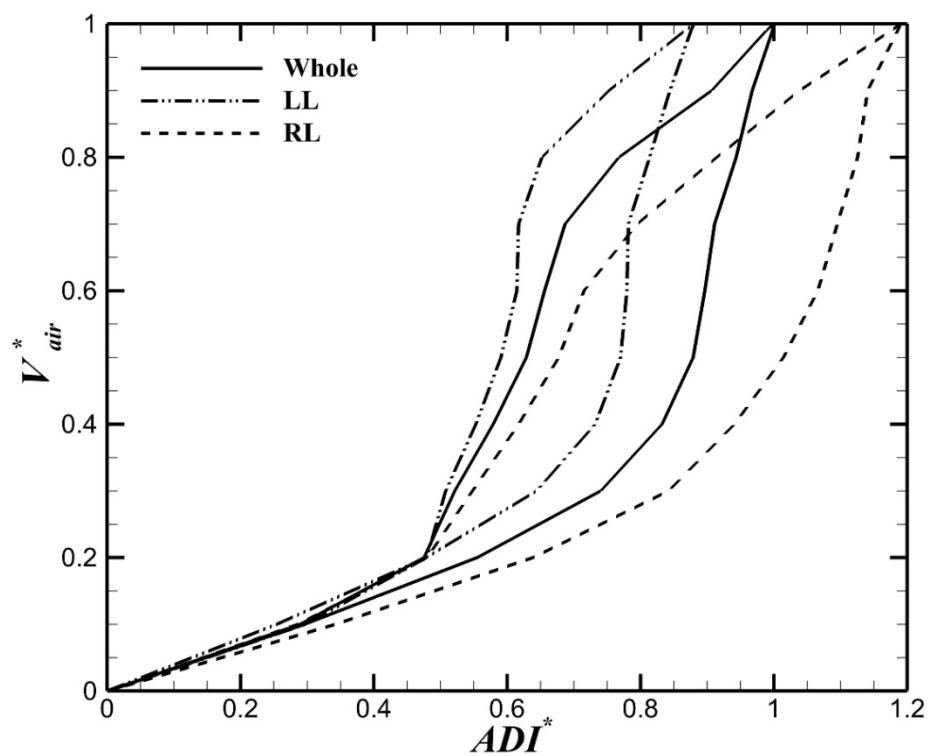
Figure 3.8. (a) Mean (±SE) of *ADI** in the whole lung (b) Mean of *ADI** in the whole, left and right lungs during VCFB for the five subjects
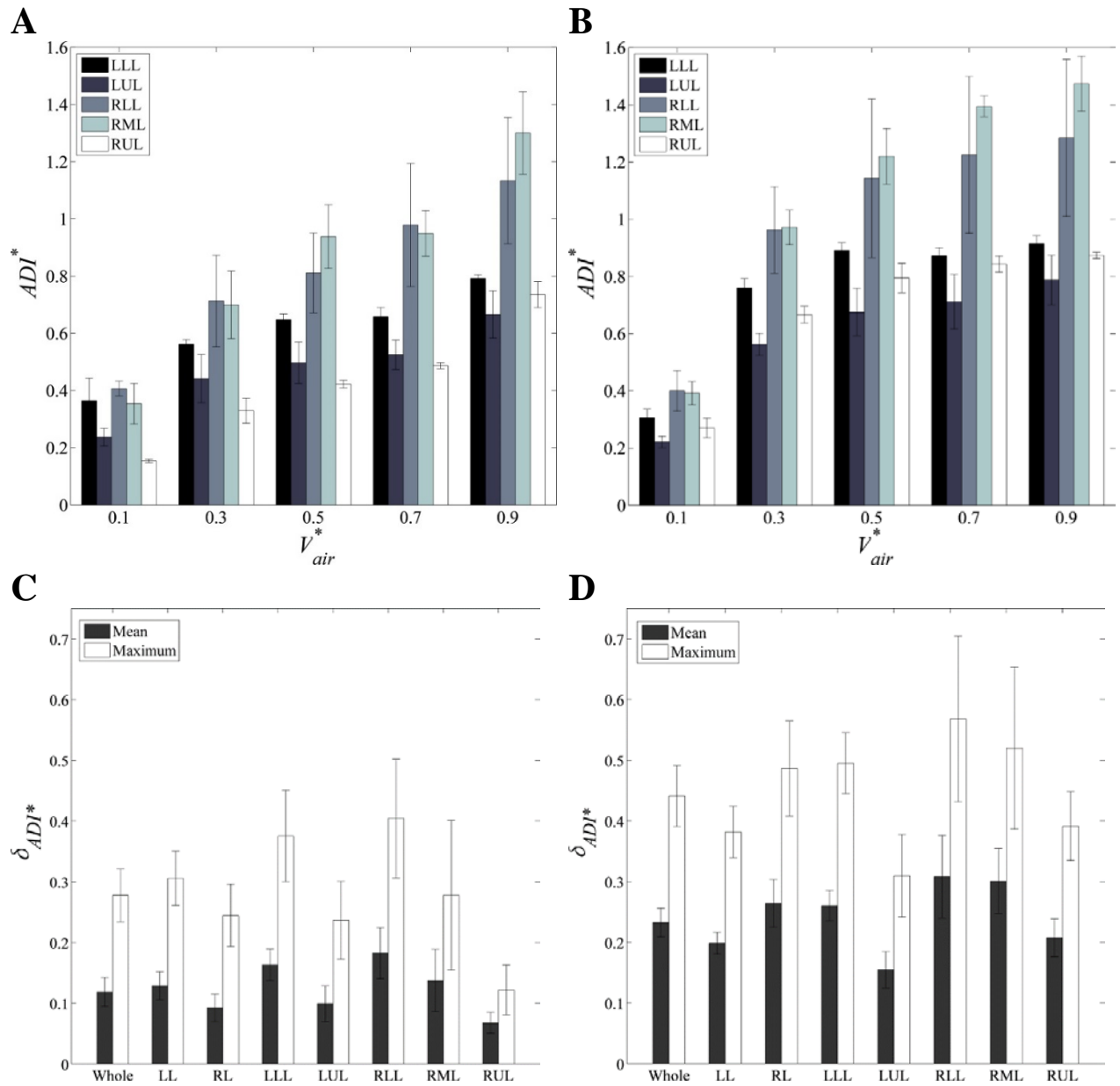
Figure 3.9. Bar graph showing (a) mean (±SE) of lungs and lobar ADI^* values of exhalation and (b) inhalation, (c) mean (±SE) and maximum (±SE) of lungs and lobar nonlinearity of exhalation and (d) inhalation
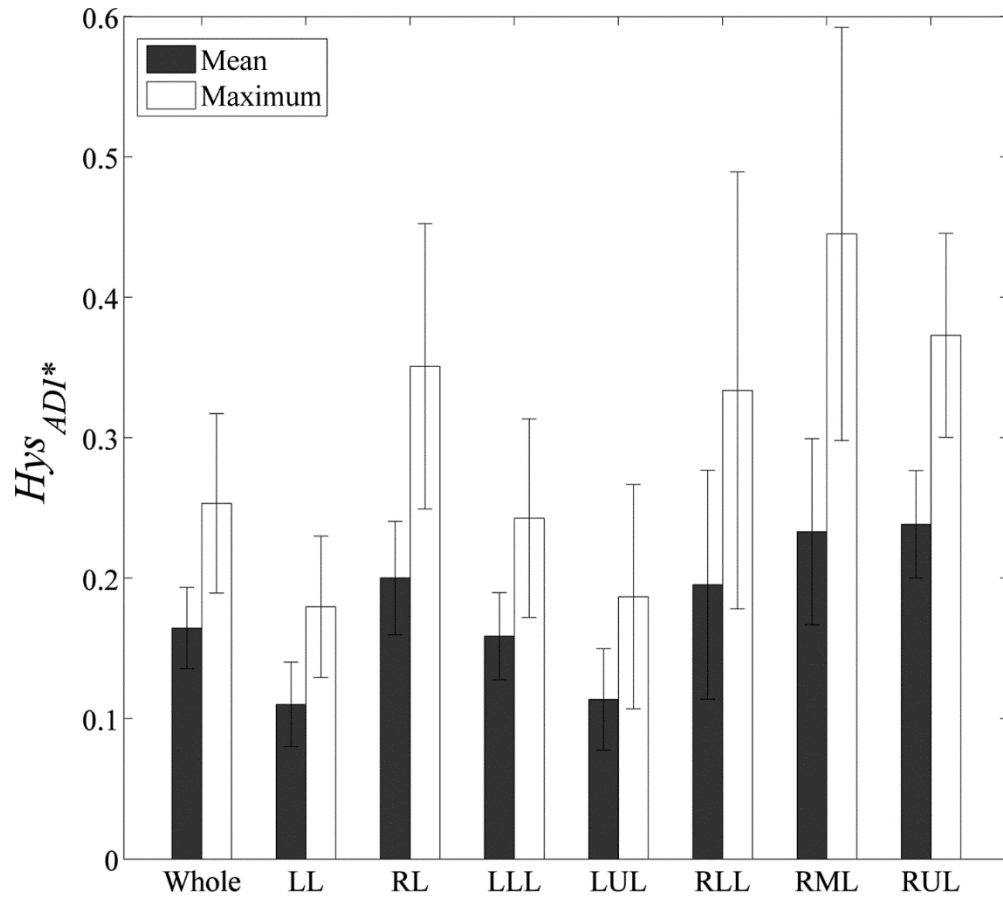
Figure 3.10. Bar graph showing mean (±SE) and maximum (±SE) of lungs and lobar hysteresis for the five subjects

4   A 4D-CT COMPARISON OF HEALTHY VS. ASTHMATIC HUMAN LUNGS

4.1 Introduction

In obstructive lung diseases such as asthma, accurate quantification of regional features and their heterogeneity is essential for advancing our understanding of the underlying mechanisms of disease. Due to non-linear behavior and hysteresis of lung motion, the analysis for breathing lungs is desirable to characterize alterations of regional ventilation and tissue deformation in asthmatic lungs. Magnetic resonance (MR) and X-ray computed tomography (CT) have recently been used to advance our understanding of the lung function in asthmatic patients ((7), (9), (44)), but imaging has been carried out during inspiratory and expiratory breath holds. Using those static breath-hold techniques, regional ventilation, ventilation heterogeneity and regional deformation, have been performed to identify the regions of air flow obstruction and airway resistance in asthmatics ((13), (45)). However, it is well recognized that hysteresis, representative of regional differences in lung mechanics is minimized or eliminated during step-wise inflation or deflation of the lung. With the introduction of four-dimensional CT (4D-CT) methods (40) for assessing the lung under well controlled tidal breathing techniques and with the introduction of ultra low-dose imaging methods which maintain quantitative accuracy of the reconstructed image (56), dynamic imaging for total lung volume is feasible, allowing for the assessment of regional lung mechanics during active respiration. Advances in image registration techniques provide the ability to assess regional functional and structural metrics such as ventilation and directional tissue deformation ((41), (62), (83)).

Jahani et al. (40) have utilized 4D-CT image data for healthy human lung during tidal breathing to estimate regional ventilation and hysteresis of lung motion between inhalation and exhalation, and compared their findings to those obtained from static images at deep breathing. The study demonstrated that non-linearity of anisotropic deformation was greater in lower regions and it was smaller during exhalation. Although some studies have applied 4D-CT imaging in patients with emphysema (78) and lung cancers ((5), (74)), it has yet to be investigated for asthmatic subjects. In a study of healthy vs. asthmatic lungs, Tzeng et al. (69) showed that airway resistance provoked by bronchial challenge causes ventilation heterogeneity for both healthy and asthmatic subjects with greater heterogeneity in asthmatics. With matching of inhalation vs. exhalation scans, Choi et al. (12) showed similar regional lung function for healthy and non-severe asthmatic lungs by estimating regional air volume change and air trapping. In a different study, they quantified structural and functional alterations for both non-severe and severe asthmatics, yet the alterations in non-severe asthmatics were not significant as compared with severe asthmatics, but being close to healthy subjects (11). It is our hypothesis that because of airway resistance during breathing dynamic imaging will serve to enhance the heterogeneity of lung function metrics and this increased heterogeneity will be greater in the severe asthmatic. Furthermore, it is expected analysis of dynamic imaging provide new information about lung deformation in asthmatics which can be extracted by quantifying non-linearity and hysteresis of lung motion.

This study aims to assess regional ventilation and deformation for asthmatic human lungs using 4D-CT image data for comparison with our already reported healthy population (40). We utilize a unique dual rolling-seal piston to control tidal breathing for consistent

reconstruction of lung volumes ((23), (40)). In addition, a mass preserving image registration method (83) is employed to derive regional ventilation and anisotropic deformation. In this study, ventilation heterogeneity estimated from dynamic lung images of both healthy and asthmatic subjects are compared with those obtained from static deep-breathing lung images. We seek to establish tools for assessing heterogeneity for the purposes of utilizing these tool, eventually, for the development and assessment of new interventions and to better sub-phenotype an asthma population. In addition, precise estimation of regional ventilation during breathing can provide physiological boundary conditions for computational fluid dynamic (CFD) analysis in quantifying air flow and pressure distribution ((80), (81)). Furthermore, anisotropic deformation is utilized to quantify non-linearity and hysteresis of lung motion for healthy vs. asthmatic human lungs between inhalation and exhalation. A motivation for quantification of non-linearity and hysteresis using 4D-CT in asthmatics is to provide essential information to capture abnormal movements and sensitive regions within diseased lungs.

4.2 Method

4.2.1 *Image data acquisition*

Datasets were acquired from five non-severe asthmatics and one severe asthmatic human volunteer for comparison with previously acquired set of 5 normal subjects (40). A full set of pulmonary function tests (PFTs) were performed for each subject in the upright body posture. The PFTs provided preliminary lung information such as total lung capacity (TLC), functional residual capacity (FRC), residual volume (RV), vital capacity (VC), forced vital capacity (FVC), and forced expiratory volume in 1 second (FEV1). Asthmatic

subjects and their severity were categorized based on the National Heart, Lung, and Blood Institute (NHLBI) guidelines for the diagnosis and management of asthma (55).

CT scanning was performed for each subject to acquire both static and dynamic MDCT image data sets in supine position, withholding of bronchodilators for 12 hours to observe baseline lung function. Two static scans were acquired at FRC (~15% VC) and TLC (95% VC) using a pneumotachometer-controlled device to achieve accurate breath-hold volumes (38). For dynamic imaging, a dual rolling-seal piston system (23) was utilized to control amplitudes of inhalation and exhalation during breathing as previously described (40). Using this system, we coached the subjects to breathe through the device at a regular and consistent respiratory rate. Because of scanning limitation the respiratory rate should be above 12 breaths per minute to achieve consistent multiple breathing cycles. Reconstruction of volumetric lung image from 4D-CT image data was performed at 10-14 selected phases of each subject's respiratory cycle.

All subjects were studied under the University of Iowa Institutional Review Board and the radiation safety committee approval and with informed consent. Siemens Somatom Definition Flash dual-source 128-slice MDCT scanner (Forchheim, Germany) was utilized for the static and dynamic scanning. The parameters for scanner such as scan type, slice thickness, peak voltage and effective current were set to spiral, 0.75 mm, 120 kV and 75 mAs, respectively. All MDCT lung images were acquired at a reconstruction matrix of 512 × 512 and a section spacing of 0.5 mm with use of B35f kernel. Furthermore, in order to segment lungs, lobes and airways, a semi-automatic segmentation software, Apollo (VIDA Diagnostics, Coralville, Iowa), was employed in the same way is for the prior healthy volunteers (40).

4.2.2   Respiratory cycle

The total lung volume was reconstructed from multiple respiratory cycles. To construct a single respiratory cycle, air volumes and corresponding times, recorded by a turbine-based flow meter, were normalized at the nth cycle, denoted by V_{air}^{*n} and t^{*n}, respectively. The mean of those normalized air volumes for all cycles was obtained for a single respiratory cycle [$V_{air}^{*}(t^{*})$, for more details, see (40)]. Thus, the normalized total air flow at time point t_p^{*} was computed as follows:

$$Q^{*}(t_p^{*}) = \left(\frac{dV_{air}^{*}}{dt^{*}}\right)_{t_p^{*}} \approx \frac{V_{air}^{*}\left(t_{p+1/2}^{*}\right) - V_{air}^{*}(t_{p-1/2}^{*})}{t_{p+1/2}^{*} - t_{p-1/2}^{*}}, \tag{4.1}$$

In this study, the time step ($t^{*}_{p+1/2} - t^{*}_{p-1/2}$) was set to 0.01.

4.2.3   Image Registration

We extracted fractions of lung tissue and air volume using CT density in Hounsfield Unit (HU) as follows

$$\beta_{tissue}(\mathbf{x}) = \frac{I(\mathbf{x}) - HU_{air}}{HU_{tissue} - HU_{air}}, \text{ and } \qquad \beta_{air}(\mathbf{x}) = \frac{HU_{tissue} - I(\mathbf{x})}{HU_{tissue} - HU_{air}} \tag{4.2}$$

where $\beta_{tissue}(\mathbf{x})$, $\beta_{air}(\mathbf{x})$, $I(\mathbf{x})$, HU_{tissue} and HU_{air} are tissue fraction, air fraction, image density at position $\mathbf{x}$, *HU* of tissue and *HU* of air, respectively. In this study, we set 55 for HU_{tissue} and -1000 for HU_{air}.

A mass preserving image registration method (83) was utilized to obtain a spatial transformation $\mathbf{T}(\mathbf{x})$ to match each pair of lung images at differing inflation levels. $\mathbf{T}(\mathbf{x})$ was determined by minimizing the sum of squared local tissue volumes difference (SSTVD) between two images (83). One image was considered as a reference image and

the other was considered as a floating image. In this study, lung images at TLC and end exhalation (EE) were taken as reference images for respective static and dynamic scans.

4.2.4   Registration-derived variables

Local air volume (v_{air}) at location **x** was computed with the spatial transformation **T**(**x**) as

$$v_{air}(\mathbf{x}) = v\big(\mathbf{T}(\mathbf{x})\big)\beta_{air}\big(\mathbf{T}(\mathbf{x})\big),\tag{4.3}$$

where v is local volume. With Eq. 3.5, regional air volume fraction, $v_{f,air}$, was defined as the ratio of sum of v_{air} in each region to total air volume. Furthermore, for consistency with air volume measured by the turbine-based flow meter, CT-based local air volume during tidal breathing was normalized as follows:

$$v_{air}^{*} = \frac{v_{air}-v_{air,EE}}{V_{air,EI}-V_{air,EE}}.\tag{4.4}$$

where V_{air} is the sum of local air volumes at end inhalation (EI) or EE within the whole lung.

Furthermore, air trapping percentage (AirT%) was defined as the ratio of number of voxels with air trapping to total number of voxels in each lobe or total lung. Instead of single density-threshold-based air trapping approach ($I_{threshold} = -850$ HU) (6), we used a fraction-threshold-based air trapping approach ($\beta_{air,threshold} = 0.9$) to eliminate inter-subject variability (12). The subject-specific threshold ($I_{threshold}$) is calculated as

$$I_{threshold} = (1 - \beta_{air,threshold})HU_{tissue} + \beta_{air,threshold}HU_{air,trachea}\tag{4.5}$$

.

We then assessed local anisotropic deformation using principle strains, i.e., $\lambda_1 > \lambda_2 > \lambda_3$, obtained from lung displacement at each location (1). The anisotropic deformation index (ADI) was calculated as:

$$ADI = \sqrt{\left(\frac{\lambda_1 - \lambda_2}{\lambda_2}\right)^2 + \left(\frac{\lambda_2 - \lambda_3}{\lambda_3}\right)^2} \tag{4.6}$$

ADI quantified the degree of preferential deformation of a local volume. To reduce inter-subject variability, we normalized ADI with its value at EI. Normalized anisotropic deformation index, ADI*, was used to quantify non-linearity and hysteresis of lung deformation during tidal breathing. Non-linearity, δ_{ADI^*}, at each location was defined as the difference of ADI* estimated from cubic interpolation for each phase and corresponding values obtained from linear assumption between EE and EI. In addition, the hysteresis at each location, $Hys_{ADI^*}(\mathbf{x})$, was quantified by the absolute difference between the ADI* of inhalation and exhalation at the same V_{air}^*.

4.2.5   Interpolation method

A cubic spline interpolation was utilized to estimate a continuous function for each variable during tidal breathing. The interpolated values at phase i were computed from the values derived from given lung images as a function of V_{air}^* [$s_i(V_{air}^*)$] (40), where s_i is a local variable interpolated in the interval of $(V_{air,i}^*, V_{air,i+1}^*)$. In this study, the variable s was either v_{air}^* or ADI*. Thus, the normalized air flow was calculated as $\frac{dv_{air}^*}{dV_{air}^*}\left(\frac{dV_{air}^*}{dt^*}\right)$ from the composition of the derivative of v_{air}^* and the derivative of breathing waveform (Eq. 3.2) . Consequently, the local air flow fraction, q_f, was defined as the ratio of local air flow to total air flow

$$q_f = \frac{dv_{air}^*}{dV_{air}^*} \tag{4.7}$$

To compare distribution of air volume change between static and dynamic scans, we assume linear interpolation between TLC and FRC and the average values from cubic interpolation between EE and EI, respectively. For linear assumption, q_f was simplified as the ratio of local air volume change to total air volume change ($\Delta v_{air}/\Delta V_{air}$). Furthermore, regional coefficient of variations (CV) of air volume changes (defined as standard deviation of Δv_{air}/ mean of Δv_{air}) was calculated to quantify heterogeneity between static and dynamic scans or between healthy and asthmatic subjects.

4.3 Results

4.3.1 PFT-, CT-based volumes, and air-trapping percentage

Table 4.1 indicated demographic information and PFT, %predicted values, ((67), (28), (29)) of five healthy, five non-severe, and one severe asthmatic subjects. FEV1, %predicted values and FEV1/FVC for non-severe asthmatic subjects were significantly smaller than those of healthy subjects ($P < 0.01$). FRC and RV, %predicted values of non-severe asthmatics were within normal range while those of the severe asthmatic subject were greater than normal range. Furthermore, TLC and FRC values obtained from CT images in supine position were significantly correlated with those obtained from PFT in upright position ($R^2 > 0.88$). Next, with the static image at FRC, we calculated air-trapping percentages (AirT%) for all subjects (**Table 4.2**). There was no significant difference of AirT% between healthy and non-severe subjects ($P > 0.46$), whereas AirT% was considerably elevated in the severe asthmatic subject, being consistent with the increased RV and FRC of the subject (Table 4.1).

4.3.2   Total and lobar air volumes and air flows

Total air volumes from CT images at respective phases, e.g., 10-14 phases per subject, were significantly correlated with corresponding air volumes measured by the turbine-based flow meter ($R^2 > 0.97$). With the meter-measured air volumes, we further estimated normalized total air flow (Q^*, Eq. 4.1) for the five healthy and six asthmatic subjects (**Figure *4.1***). Both healthy and asthmatic subjects demonstrated similar trends during tidal breathing. However, the asthmatic subjects had greater Q^* during exhalation ($P < 0.05$) while the difference was not significant during inhalation ($P > 0.15$).

We obtained the means of lobar air volume fraction, $v_{f,air}$, i.e. the ratio of lobar air volume to total air volume, for five non-severe asthmatics and one severe asthmatic during exhalation and inhalation, respectively (Figure 4.2). The trends of non-severe asthmatic subjects (**Figure *4.2***, A and B**)** were similar with those of healthy subjects (40) in that $v_{f,air}$ of upper lobes decreased and $v_{f,air}$ of lower lobes increased with increasing total lung volume ($P < 0.05$, between EE and EI). On the other hand, the severe asthmatic subject exhibited the opposite trends (**Figure *4.2***, C and D). Lobar flow fractions q_f (Eq.) for all subjects were then compared between static and dynamic scans in **Figure *4.3***. In this figure, linear interpolation was employed to calculate q_f for static scans between TLC and FRC (denoted by $q_{f,SCT}$), and cubic interpolation was used to calculate q_f for dynamic scans between EE and EI (denoted by $q_{f,4D-CT}$). The $q_{f,SCT}$ values were in similar range for all subjects during deep breathing (**Figure *4.3***A). On the other hand, the $q_{f,4D-CT}$ for the severe asthmatic subject showed different values in the left lower lobe (LLL), left upper lobe

(LUL) and right upper lobe (RUL) as compared with those for healthy and non-severe asthmatic subjects during tidal breathing (**Figure *4.3*B**). **Figure *4.3*C** indicated that there was a good correlation between lobar $q_{f,SCT}$ and $q_{f,4D-CT}$ for both healthy ($R^2 = 0.84$) and non-severe asthmatic ($R^2 = 0.90$) subjects. Nonetheless, the severe asthmatic subject showed deviations in three lobes from the identity line.

4.3.3 *Heterogeneity of regional ventilation*

To quantify global and lobar heterogeneity for air flow, we calculated CVs of local air volume changes for both static (FRC vs. TLC) and dynamic (EE vs. EI) scans (**Table 4.3**). Heterogeneity in dynamic images significantly increased as compared with that in static images for both healthy and asthmatic subjects ($P < 0.005$). In addition, heterogeneity of lower lobes in the severe asthmatic subject was much greater than that of upper lobes in dynamic images while this feature was not observed in static images. To demonstrate the difference in heterogeneity between dynamic and static images, **Figure *4.4*** displayed normalized histograms for the ratio of local air volume change over their average value over the whole lung for two representative subjects. One was a healthy subject with FEV1/FVC = 0.77 and the other was a non-severe asthmatic with FEV1/FVC = 0.60. The histogram based on dynamic images showed a more widespread distribution, signifying greater variation in air volume change at local (image-voxel) scale although lobar air flow fractions at global scale for static and dynamic images were similar (see Figure 4.3).

4.3.4 *Non-linearity and hysteresis of lung motion*

The normalized anisotropic deformation index (ADI[*]) was used to quantify global and local non-linearity and hysteresis of lung deformation during tidal breathing. For both healthy and asthmatic subjects, ADI[*] and non-linearity (δ_{ADI^*}, distance from the identity

line) during inhalation were in a same range and greater than those of exhalation (Figure 4.5). However, during exhalation, the δ_{ADI^*} values for asthmatic subjects were greater than those of healthy subjects. Consistent with total lungs, in all lobes except RUL, the δ_{ADI^*} values for asthmatic subjects during exhalation were greater than those of healthy subjects (Figure 4.6A, $P < 0.05$). Furthermore, for both healthy and asthmatic lungs, the left lungs had greater δ_{ADI^*} during exhalation (Figure 4.6A), while the right lungs had greater δ_{ADI^*} during inhalation (Figure 4.6B, $P < 0.05$). Furthermore, the lower lobes had greater δ_{ADI^*} than the upper lobes for all subjects ($P < 0.05$). Consequently, greater values of δ_{ADI^*} in asthmatic subjects during exhalation resulted in less global and lobar hysteresis (Hys_{ADI^*}) during tidal breathing (Figure 4.6C). Hys_{ADI^*} of asthmatics was less than that of healthy subjects in all regions. Hys_{ADI^*} of the right lungs was greater than that of the left lungs for both healthy and asthmatic subjects.

4.4 Discussion

Using the unique dataset of dynamic 4D-CT volumetric lung images, we analyzed regional ventilation, heterogeneity and lung deformation for asthmatic subjects including five non-severe asthmatics and one severe asthmatic subject. The results were compared with the previously published 4D-CT data of five healthy subjects (40). We further compared the differences between the analyses based on dynamic and static images. A dual rolling-seal piston system (23) was utilized to control tidal volume and reduce inter-subject viability for both healthy and asthmatic subjects (Figure 4.1). For analysis of regional ventilation, we employed an image matching technique (83) to derive additional metrics, such as anisotropic deformation (ADI), to quantity non-linearity as well as lung hysteresis during tidal breathing.

4.4.1   Regional ventilation

We first investigated air trapping (AirT%) at FRC scans for all subjects, because it has been widely used as a putative index of small airways disease ((6), (12), (57)). In the current study, AirT% in non-severe asthmatics was similar with that of healthy subjects (Table 4.2), implying that the baseline lung functions of non-severe asthmatic lungs are close to normal (6). This was further supported by the fact that both healthy and non-severe asthmatic subjects showed similar trends of lobar air volume fraction during tidal breathing ((40) and Figure 4.2A and B). However, unlike the non-severe asthmatic and healthy subjects, the air volume fraction in upper lobes increased at larger lung volumes in the severe asthmatic subject (Figure 4.2C and D). This is possibly due to the significant air trapping of lower lobes (Table 4.2) as demonstrated by Choi et al. (13) that air trapping predominantly occurs in the lower lobes than the upper lobes of severe asthmatics.

Ventilation heterogeneity during tidal breathing was predominantly increased relative to those during deep breathing for both healthy and asthmatic subjects. However, there was no significant difference of ventilation heterogeneity between healthy and non-severe asthmatic subjects. In the non-severe asthmatic population it may require a methacholine challenge to bring out significant differences. However, these subjects were not given a bronchodilator. The increased heterogeneity in dynamic scans may be attributable to the presence and heterogeneous variation of airway resistance during tidal breathing and the absence of airway resistance during breath hold for static scans (30). Similar characteristics of airway resistance between asthmatic and non-asthmatic lungs were also observed in Wongviriyawong et al.'s study (75). In their study, at baseline before methacholine challenge, airway resistances for healthy and asthmatic subjects were similar,

whereas greater resistance, as expected, was found in asthmatic lungs after methacholine challenge. Investigation of lobar ventilation heterogeneity also increased during dynamic breathing, but their quantities were different in each lobe. For example, the severe asthmatic subject exhibited higher heterogeneity especially in lower lobes. Furthermore, since lobar air flow fractions between static and dynamic scans were well correlated for both healthy and non-severe asthmatic subjects in lobar scale (Figure 4.3C), smaller regions such as constricted small airways might be responsible for different ventilation heterogeneity between dynamic and static images (70). Downie et al. (18) also demonstrated that ventilation heterogeneity can be used to determine airway hyper-responsiveness in asthmatics. Since heterogeneity increased during tidal breathing, if asthmatic subjects respond to methacholine challenge, ventilation heterogeneity in 4D-CT may be utilized as a sensitive metric to diagnose asthmatic alterations.

4.4.2 Non-linearity and hysteresis

Assessment of lung deformation during tidal breathing illustrated larger non-linearity of all asthmatics (non-severe and severe:Figure 4.5) relative to healthy subjects during exhalation. Air flow resistance due to airway narrowing would be elevated during exhalation as compared with that during inhalation, because transpulmonary pressure is negative during expiration (36). Therefore, the respiratory system needs to provide higher forces and works to overcome the resistance during exhalation ((36), (46)). Some of those forces, such as shear forces, are correlated with anisotropic deformation ((24), (41)). Thus, we speculated that larger anisotropic deformation and non-linearity of asthmatic lungs during exhalation were due in part to increased shear forces produced during exhalation. Furthermore, the characteristics in total lungs showing the increase of non-linearity during

exhalation were demonstrated in most regions of asthmatics as compared with healthy subjects. Thus, lower total and regional hysteresis during exhalation in asthma is due to the higher non-linearity of increased shear forces, relative to healthy subjects.

4.5 Conclusions

In this study, we found two significant differences between healthy and asthmatics (both non-severe and severe) during exhalation. First, the increased normalized air flow (Figure 4.1), and the other was the increased anisotropic deformation (Figure 4.5) in asthmatics. In addition to the metrics discussed here, there is a need to investigate the relationship of local lung mechanics with global alterations. CFD simulation may be used to shed light on the underlying mechanics. Analysis of 4D-CT image data can provide actual regional air flow during breathing to implement CFD simulation to estimate pressure distribution. Having regional air flow and pressure distribution would provide information to identify and predict regional air flow obstruction and airway resistance in asthmatics.

Increased ventilation heterogeneity during dynamic breathing was observed in both healthy and asthmatic subjects. However, the heterogeneity was different between the population of non-severe and the one severe subject but, because there is only one severe subject, a statistical statement is not possible. To define common characteristics among a group of asthmatic and healthy subjects, more subjects are needed. However, statistical tests were performed to verify significant difference between regional characteristics. Furthermore, we obtained means and SE of every global and regional variable in each group to evaluate inter-subject variability. To acquire more dynamic lung images, it is necessary to resolve issues such as radiation dose, imaging protocols, image quality and cost.

Table 4.1. Demographic and PFT information for five healthy, five non-severe asthmatic and one severe asthmatic subjects

	Healthy	Non-severe asthmatic	Severe asthmatic	Mann-Whitney U test† (P value)
Subjects, n (female)	5 (2)	5 (2)	1 (1)	
Age, yr	40 ± 15	37 ± 13	52	0.89
BMI, kg/m^2	27 ± 3	26 ± 5	31	0.91
Race, n (white non-Hispanic/Hispanic/Asian)	4 / 1 / 0	5 / 0 / 0	0 / 0 / 1	-
TLC, %predicted	94 ± 7	95 ± 7	99	0.92
FRC, %predicted	82 ±10	95 ± 16	128	0.12
RV, %predicted	83 ± 12	89 ± 6	153	0.76
FVC, %predicted	94 ± 9	92 ± 9	72	0.75
FEV1, %predicted	92 ± 6	76 ± 7	36	< 0.05
FEV1/FVC × 100	79 ± 2	67 ± 5	39	< 0.01

Values are means ±SD; n, no. of subjects. †Statistical tests were performed between five healthy and five non-severe asthmatic subjects.

Table 4.2. Means ± SD of total and lobar AirT% at FRC for 5 healthy, 5 non-severe asthmatic, and 1 severe asthmatic subjects

	Healthy subjects	Non-severe asthmatics	Severe asthmatic	Mann-Whitney U test† (P value)
Total	9.1% ± 7.6%	6.1% ± 4.3%	51.3%	0.60
LLL	1.5% ± 1.1%	1.3% ± 0.5%	62.7%	0.75
LUL	10.7 ± 9.9%	6.7% ± 4.3%	42.1%	0.74
RLL	1.1% ± 0.7%	1.8% ± 2.1%	54.3%	0.75
RML	27.4% ± 20.2%	24.2% ± 16.4%	66.6%	0.92
RUL	9.3% ± 8.4%	6.4% ± 6.9%	30.3%	0.46

† Statistical tests were performed between five healthy and five non-severe asthmatic subjects

Table 4.3. Means ± SD of Coefficient of Variations of whole and lobar air volume change for healthy and asthmatic subjects during deep and tidal breathing

	Healthy subjects		Non-severe asthmatics		Severe asthmatic		Mann-Whitney U test† (P value)
	CV_{static}	$CV_{dynamic}$	CV_{static}	$CV_{dynamic}$	CV_{static}	$CV_{dynamic}$	
Whole	0.31 ± 0.03	0.79 ± 0.29	0.29 ± 0.02	0.68 ± 0.18	0.413652	0.934951	<0.005
LLL	0.22 ± 0.02	0.73 ± 0.19	0.22 ± 0.01	0.65 ± 0.20	0.412511	1.78656	<0.005
LUL	0.27 ± 0.05	0.80 ± 0.36	0.27 ± 0.02	0.63 ± 0.25	0.40323	0.62237	<0.005
RLL	0.23 ± 0.02	0.61 ± 0.21	0.23 ± 0.02	0.61 ± 0.15	0.370018	0.932261	<0.005
RML	0.49 ± 0.15	2.4 ± 3.04	0.43 ± 0.16	1.11 ± 0.39	0.534224	0.972335	<0.005
RUL	0.26 ± 0.02	0.59 ± 0.19	0.25 ± 0.02	0.55 ± 0.14	0.332232	0.398269	<0.005

CV_{static}, Coefficient of Variation during deep breathing; $CV_{dynamic}$, Coefficient of Variation during tidal breathing; † Statistical tests were performed between CV_{static} and $CV_{dynamic}$ for both healthy and non-severe asthmatic subjects
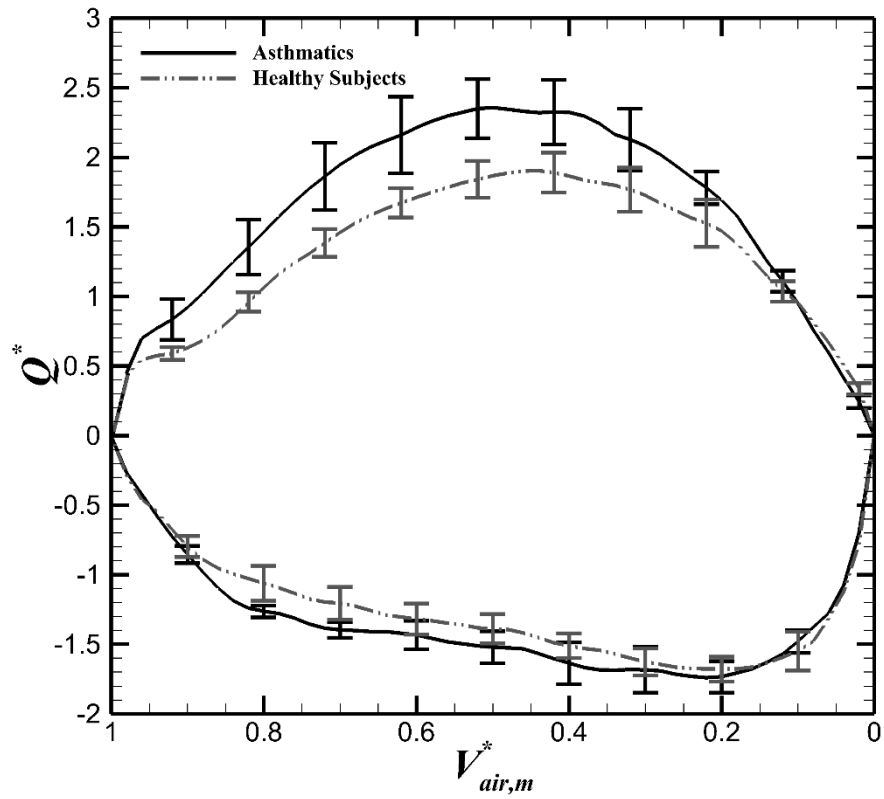
Figure 4.1. Means (±SE) of normalized air flow (Q*) measured by the turbine-based flow meter for exhalation (positive value) and inhalation (negative value) in the total lung for both asthmatic and healthy subjects

A

B

C

D
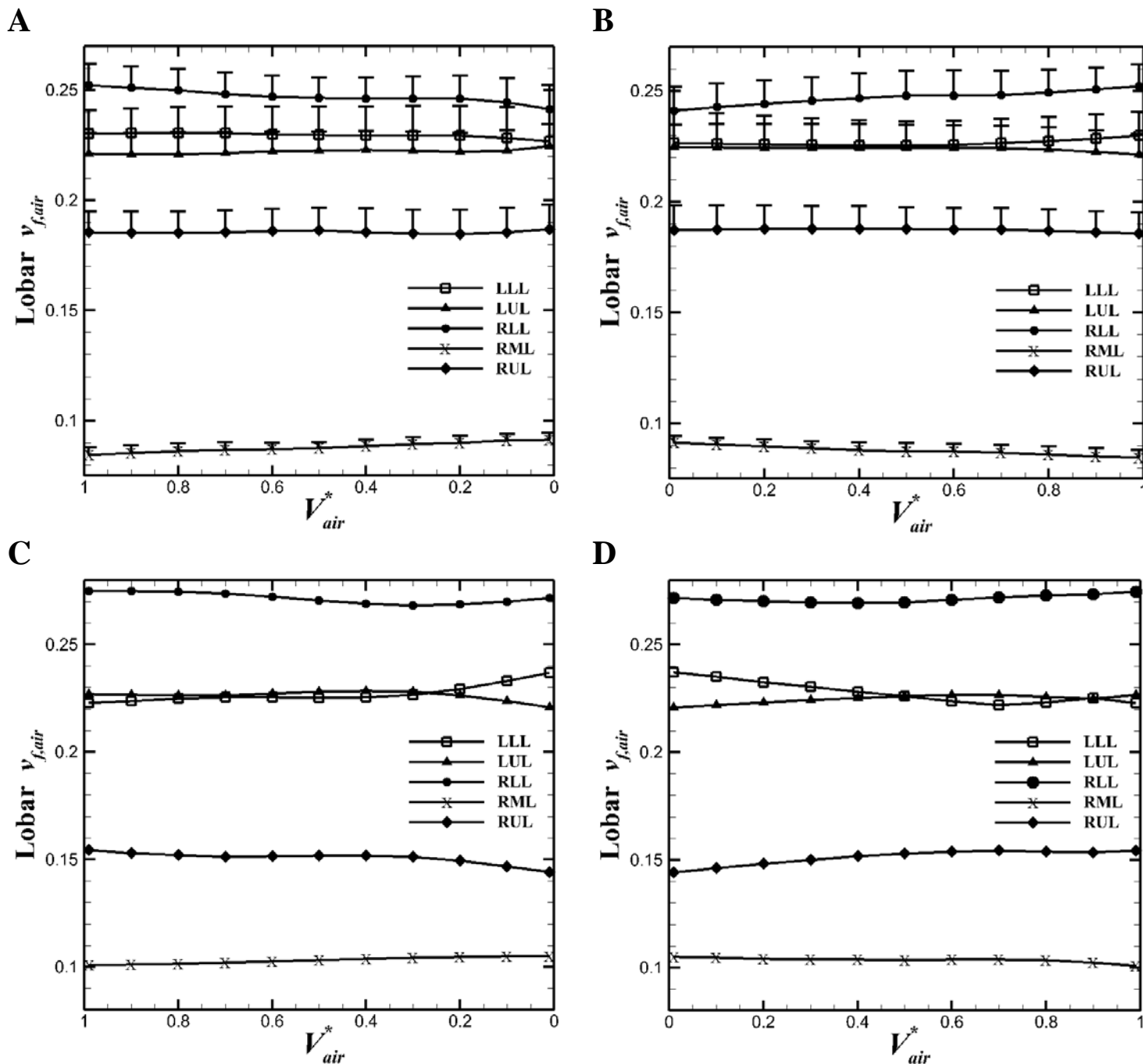
Figure 4.2. Means (+SE) of lobar air volume fraction for five non-severe asthmatics A: during exhalation and B: during inhalation, and for the severe asthmatic subject C: during exhalation and D: during inhalation

A

B

C
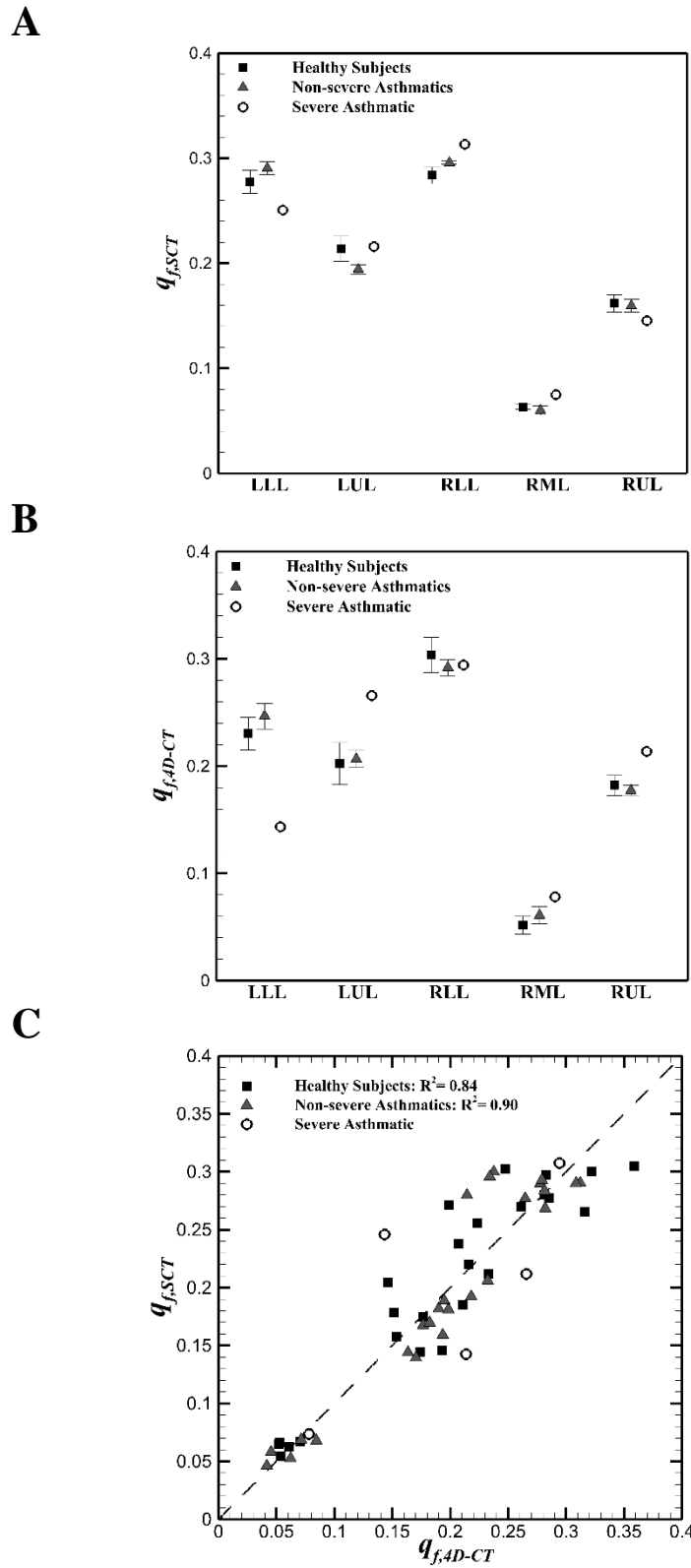
Figure 4.3. Means (±SE) of A: lobar air flow fraction ($q_{f,SCT}$) in static scans, B: lobar air flow fraction ($q_{f,4D\text{-}CT}$) in 4D-CT scans among healthy, non-severe asthmatic, and the severe asthmatic subjects; C: Comparison between lobar $q_{f,SCT}$ and $q_{f,4D\text{-}CT}$ for all subjects
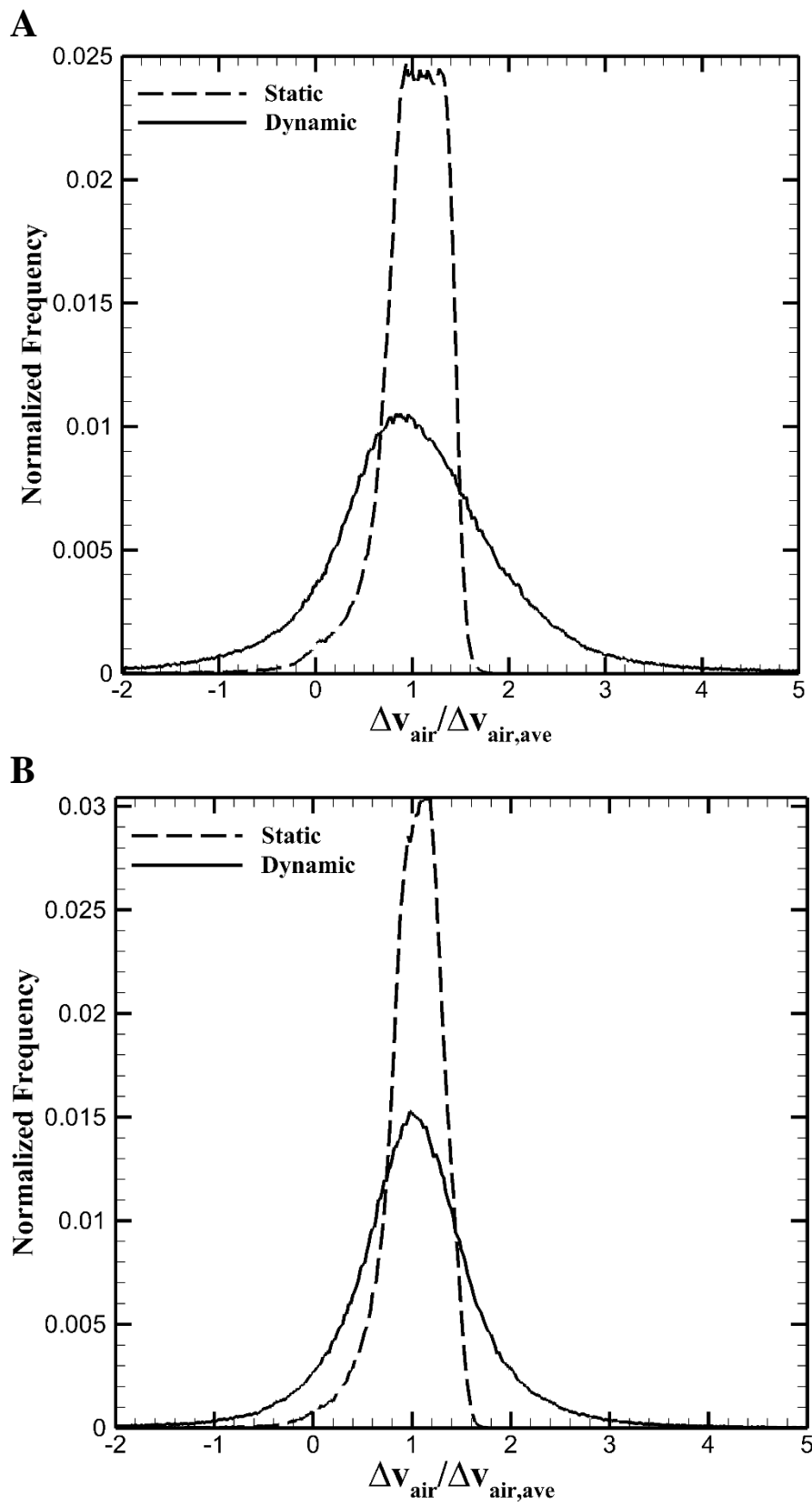
Figure 4.4. Voxel ventilation histogram for A: a representative healthy subject and B: a representative asthmatic subject
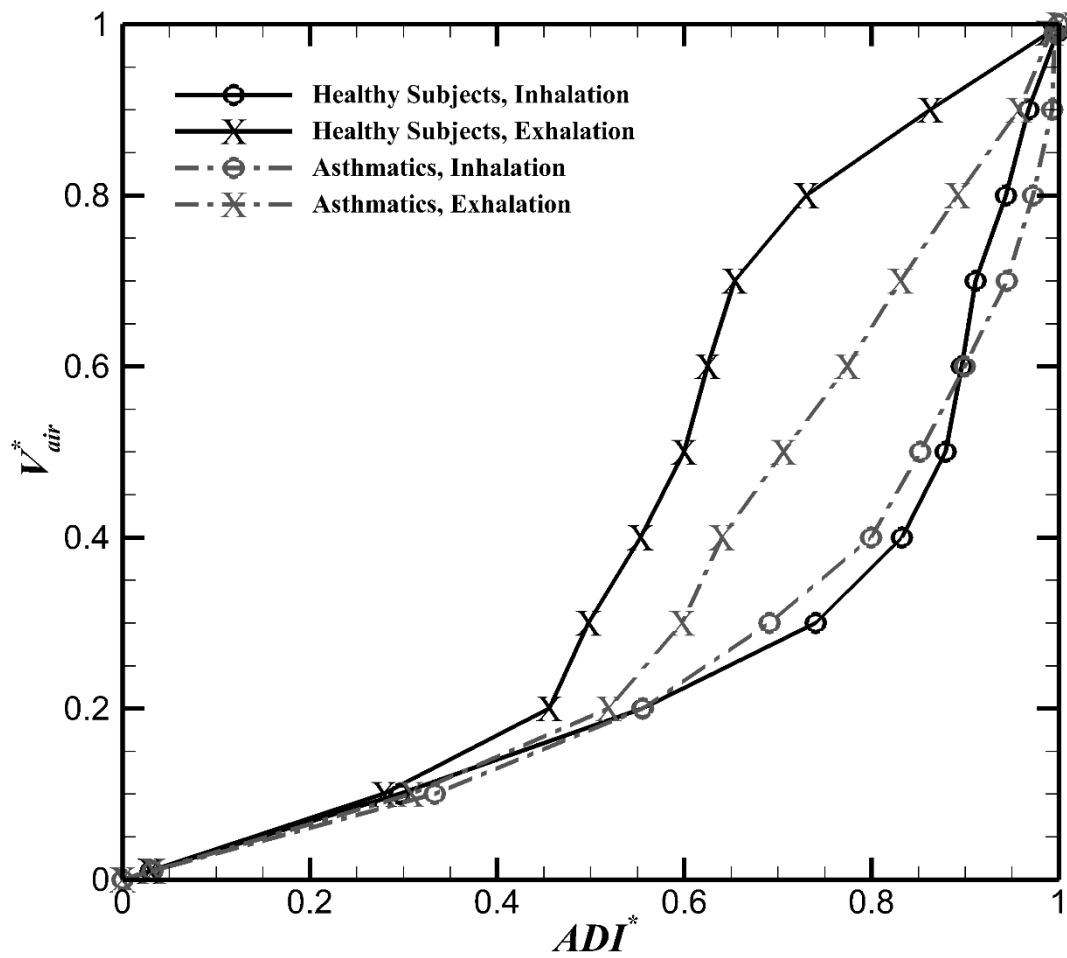
Figure 4.5. Means of ADI* in the total lungs for five healthy and six asthmatic subjects

A
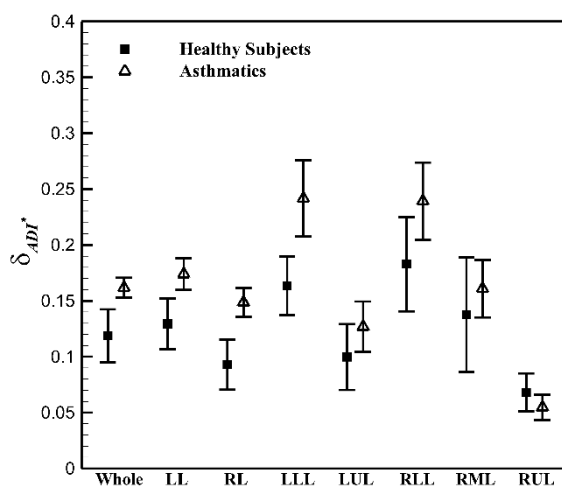
B
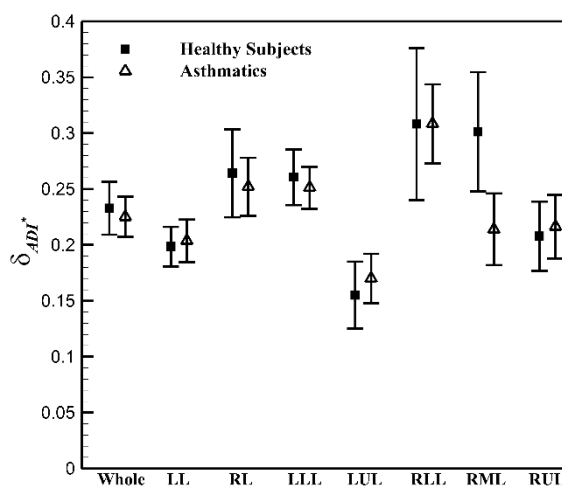
C
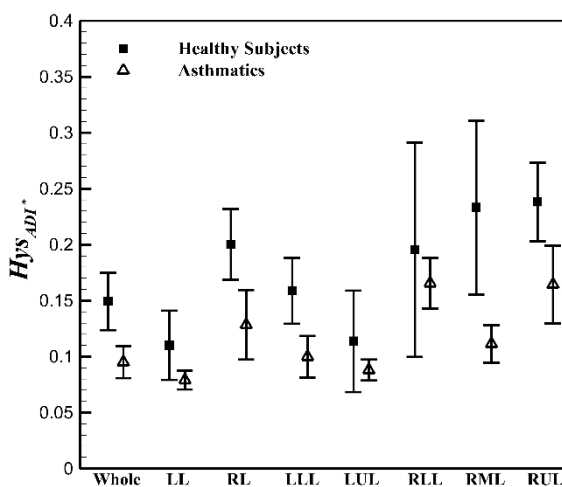
Figure 4.6. Means (±SE) of lung and lobar A: non-linearity of ADI* during exhalation B: non-linearity of ADI* during inhalation, and C: hysteresis of ADI* between five healthy and six asthmatic subjects

5 CFD SIMULATION OF ASTHMATIC LUNGS DURING TIDAL BREATHING

5.1 Introduction

In asthmatic lungs, due to increased local airway resistance and airflow obstruction, quantification of regional distributions of variables such as air volume change and pressure drop are essential to assess breathing mechanism of asthmatic lungs. Computational fluid dynamics (CFD) simulation can be used as a tool to provide regional air flow pattern and pressure distribution within airways to evaluate airway resistance, as an important indicator in asthmatic lungs, and understand flow characteristic in asthmatic lungs. However, accurate estimations of flow pattern and pressure distribution are highly dependent on airway geometry model and boundary condition (BC) used in CFD simulation. Due to the complexity of airway geometry, earlier studies idealized the airway models to estimate flow pattern in human lungs ((34), (72)). However, the idealized models could not capture the features specific to individual subjects. With recent advances in imaging techniques, high resolution computed tomography (CT) images allow us to extract subject-specific three-dimensional (3D) realistic airway models for CFD simulation ((10), (49)). However, those studies neglected the heterogeneous nature of BCs in the lung and applied uniform pressure or velocity at ending branches. Lin et al. (47) utilized a 3D-1D coupled airway model to propose a multiscale CFD simulation method. Based on their method, Yin et al. (80) estimated a subject-specific realistic BC for CFD simulation using functional residual capacity (FRC) and total lung capacity (TLC) scans with TLC airways as the geometry model. With use of image registration, they quantified realistic regional ventilation by mapping the two CT lung images.

Previously, most existing studies applied CFD simulation using rigid airways as the geometry model. However, since the lung deforms during breathing it is important to consider lung motion. Yin et al. (82) utilized the displacement field derived from registered lung images at FRC and TLC to construct a dynamic lung geometry model. Then, they extended their work for multiple lung images to develop more realistic time-varying BCs considering non-liner motion of the lung (81). However, all those studies used static scans for their simulation and did not consider the dynamic motion during breathing. Recent advances in dynamic imaging make it possible to acquire four-dimensional CT images during tidal breathing. 4D-CT imaging technique could provide more physiological boundary conditions. Miyawaki et al. (51) utilized 4D-images to develop a CFD model for a healthy breathing lung. They studied the effect of dynamic imaging on pressure drop predicted by CFD simulation. However, because of airway narrowing in asthmatic lungs, CFD simulation in asthmatics is much more challenging. Jahani et al. (39) utilized 4D-CT imaging to investigate differences between healthy and asthmatic lungs during breathing. They showed that dynamic breathing causes different regional ventilation and deformation in comparison with breath-hold condition.

In this study, we aim to utilize CFD simulation for an asthmatic subject using both static and dynamic images during tidal breathing to assess the effect of dynamic imaging on air flow structures for asthmatics. Then, we compare the results with CFD analysis of a healthy subject reported by (51). We use a mass preserving image registration technique to provide regional ventilation to set BCs and a CFD model with a multiscale 3D-1D coupled airway geometry. Knowing regional pressure drop and air flow distribution provides essential information to differentiate airway resistance indicating progression of asthma.

5.2 Methods

In this study, CFD simulation of air flow was performed in asthmatic human lung for both static and 4D-CT images. Then, the results were compared with those of a healthy subject (51). 4D-CT imaging technique accounts for space and time, yielding more realistic results due to irregular human lung motion. Air volume and displacement field of lung motion were obtained from a mass preserving image registration method (83). Then 1D tree and consequently 3D mesh were generated. While a computational-solid-mechanics (CSM)-based algorithm was used to account for mesh deformation, a volume filling method was used to employ a physiologically realistic and meaningful air flow boundary condition to compensate unresolved airways in CT images. The aforementioned methods were used to perform CFD simulations of airflow in both healthy and asthmatic human airways.

5.2.1   Image acquisition

4D-CT and static CT images for one healthy subject and one asthmatic subject were acquired as described by (40) and were used to perform the CFD simulation.

5.2.2   CFD mesh generation

In this study, we segmented TLC volumes as the reference images for the asthmatic lung like what Miyawaki et al. did for a healthy subject (51). The segmented airway geometry with labeling for the asthmatic subject is shown in Figure *5.1*. Deformation field and 1D tree were obtained from the mass preserving image registration technique. Then, the geometric model and meshing methods proposed by Miyawaki et al. (53) were used to to generate 3D mesh for airway geometry. First, airway skeleton as well as airway wall geometry were extracted from TLC images. Then, the obtained airway skeleton was used

to generate 3D mesh so that airway volume is filled with tetrahedral elements. Then the image registration technique was used to find the transformed reference surface mesh at different times in 4D-CT imaging.

5.2.3 Boundary conditions

A subject-specific boundary condition, such as flow rate, can significantly improve results of CFD simulation of pulmonary air flow. To measure the flow rate at the branches at the end of CT-resolved bronchial tree, a regional volume V_R was defined such that V_R is equal to the peripheral regions to which the ending branch ventilates. Using volume filling method to construct airways in CT-unresolved region, V_R can be obtained at the reference time point. The time rate of the change of V_R yields the flow rate at an ending branch. Also V_R at different time points can be obtained using deformable image registration.

5.2.4 CFD simulation

Large eddy simulation (LES) in a Lagrangian-Eulerian (ALE) framework was applied to capture laminar, transitional and turbulent flow (81). The filtered continuity equation as well as Navier-Stokes equations for incompressible flow were included in the governing equations.

$$\frac{\partial u_j}{\partial x_j} = 0$$

$$\frac{\partial u_i}{\partial t} + \left(u_j - u_j^{ALE}\right)\frac{\partial u_i}{\partial x_j} = -\frac{1}{\rho}\frac{\partial p}{\partial x_i} + \frac{\partial}{\partial x_j}\left[(v + v_T)\frac{\partial u_j}{\partial x_j}\right],$$

(5.1)

where u_i, u_i^{ALE}, p, ρ, v, and v_T are the ith components of fluid and grid velocities, pressure, density, kinematic viscosity, and subgrid-scale eddy viscosity, respectively. The density and kinematic viscosity of air were 1.2 kg/m^3 and 1.5 m^2/s, respectively.

Using the displacement of two surface meshes as an essential boundary condition at two different time points, a CSM-based algorithm (66) was applied to deform the volume mesh.

5.3 Results

Demographic information and PFT results of the healthy and the asthmatic subjects are shown in Table 5.1. In addition, Table 5.2 indicates global breathing information of both subjects. Total air flow, trachea hydraulic diameter and Reynolds number at peak inhalation for the healthy subject (or the asthmatic) are 50 L/min, 18.9 mm and 3740 (or 36 L/min, 16.1 mm and 2791), respectively. Figure *5.2* shows total normalized flow rates for both subjects during a single breathing cycle. It can be observed that with the dual piston system we could control breathing rate to achieve consistent air flow.

First, we utilized the CFD simulation for 4D-CT scans at EE and EI and for static scans at TLC and FRC. Table 5.3 demonstrates how air flow fraction (local flow/total flow) was distributed in the first and second generation airways (which include the left main bronchus (LMB) and right main bronchus (RMB), LUL, LLB6, RUL and BronInt, Figure *5.1*). The results showed that in large airways both healthy and asthmatic subjects had similar ranges in terms of flow rate fractions (with a difference of less than 12%). However, the distributions of air flow in the left and right healthy lungs based on the dynamic images were different from the static one. That is consistent with our results in Chapter 3. Table 5.4 shows different pressure drop distributions along the airways. The

results indicated that pressure drop distribution was different between static and dynamic simulation for both healthy and asthmatic lungs even in large airways although the values in larger airways are small. Figure 5.3 indicates that pressure distributions in smaller airways were quite different between static and dynamic scans for both healthy and asthmatic subjects.

Table 5.1. Demographic information* and PFT values (% predicted normal values) for healthy and asthmatic subjects

Subject	Healthy subject	Asthmatic
Gender	M	M
Age (yrs.)	58	49
BMI (kg/m^2)	32	27
FEV1 (L)	3.4 (83 %)	2.9 (73%)
FVC (L)	4.4 (82 %)	4.35 (85%)
FEV1/FVC	0.768	0.66
TLC (L)	7.2 (93%)	6.08 (85%)
FRC (L)	2.9 (78%)	2.86 (80%)
RV (L)	2.3 (93%)	1.73 (79%)
RV/TLC	0.318	0.28

Table 5.2. Global breathing information for the healthy and asthmatic subjects

Subject	Tidal breathing (L)	Time period (s)	Inhalation time (s)	Peak inhalation time (s)
Healthy	0.98	4.34	2.57	0.26
Asthmatic	0.89	4.24	2.25	0.42

Table 5.3. Flow rate fractions of 4D-CT analysis in the 1st and 2nd generations of the airways at peak inhalation

Healthy subject							
Dynamic				Static			
LMB		RMB		LMB		RMB	
0.42		0.58		0.48		0.52	
LUL	LLB6	RUL	BronInt	LUL	LLB6	RUL	BronInt
0.17	0.25	0.16	0.42	0.20	0.28	0.14	0.38
Asthmatic							
Dynamic				Static			
LMB		RMB		LMB		RMB	
0.49		0.51		0.47		0.53	
LUL	LLB6	RUL	BronInt	LUL	LLB6	RUL	BronInt
0.23	0.26	0.21	0.30	0.19	0.28	0.17	0.36

Table 5.4. Pressure drop (in pa) of 4D-CT analysis in the 1st and 2nd generations of the airways at peak inhalation

Healthy subject							
Dynamic				Static			
Trachea				Trachea			
1.66				0.0585			
LMB		RMB		LMB		RMB	
4.9		0.04		5.89		-0.247	
LUL	LLB6	RUL	BronInt	LUL	LLB6	RUL	BronInt
0.879	5.40	18.11	7.95	2.07	1.68	17.86	6.03
Asthmatic							
Dynamic				Static			
Trachea				Trachea			
3.69				4.95			
LMB		RMB		LMB		RMB	
13.1		1.15		4.18		0.362	
LUL	LLB6	RUL	BronInt	LUL	LLB6	RUL	BronInt
1.46	-0.23	8.14	3.33	1.51	2.75	4.33	2.14
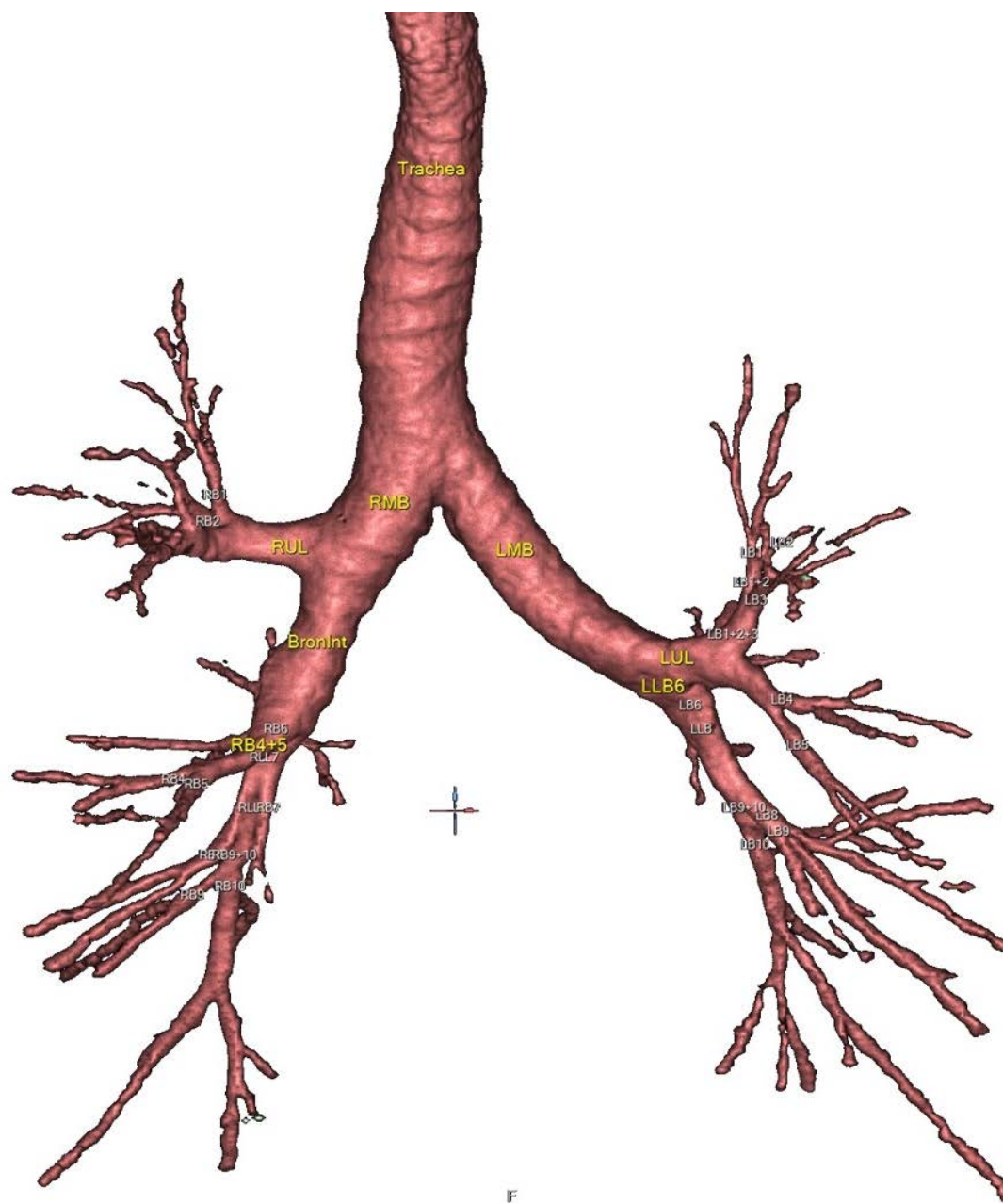
Figure 5.1. The segmented airway with its labeling at TLC for the healthy subject
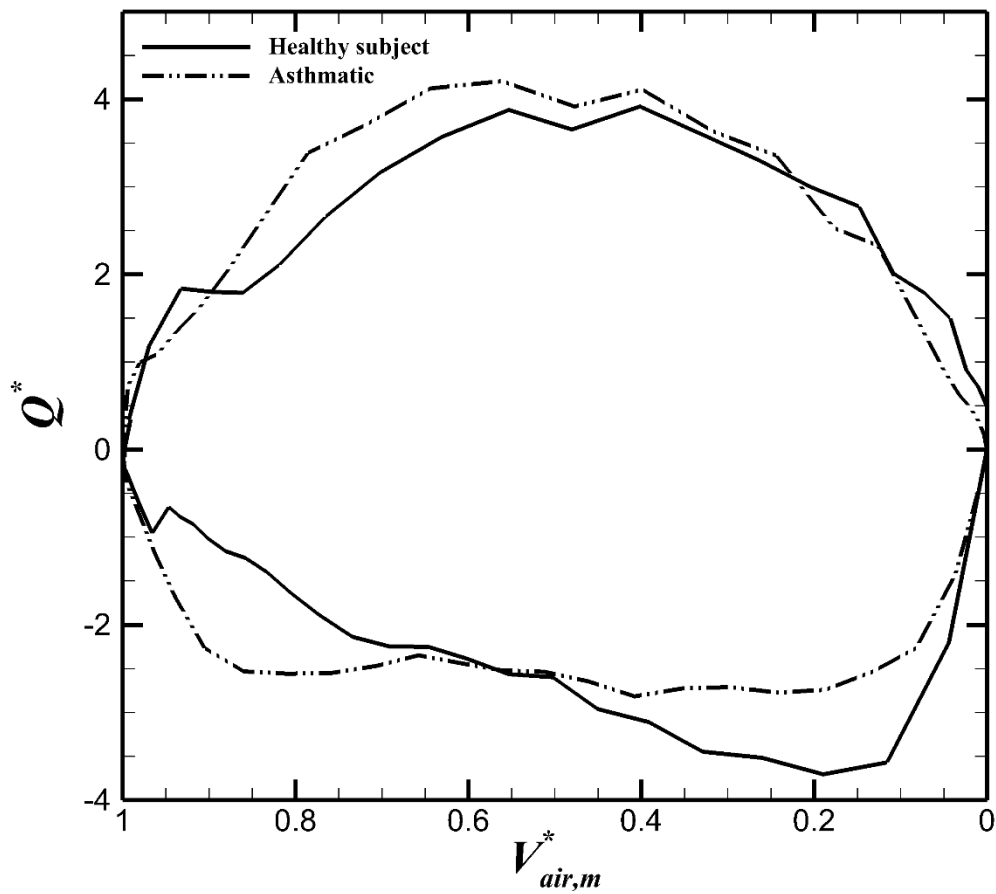
Figure 5.2. Normalized flow rates obtained from measurement for exhalation (+) and inhalation (-) in the whole lung

Dynamic　　　　　　　　　　　　　**Static**

Healthy subject

Dynamic　　　　　　　　　　　　　**Static**
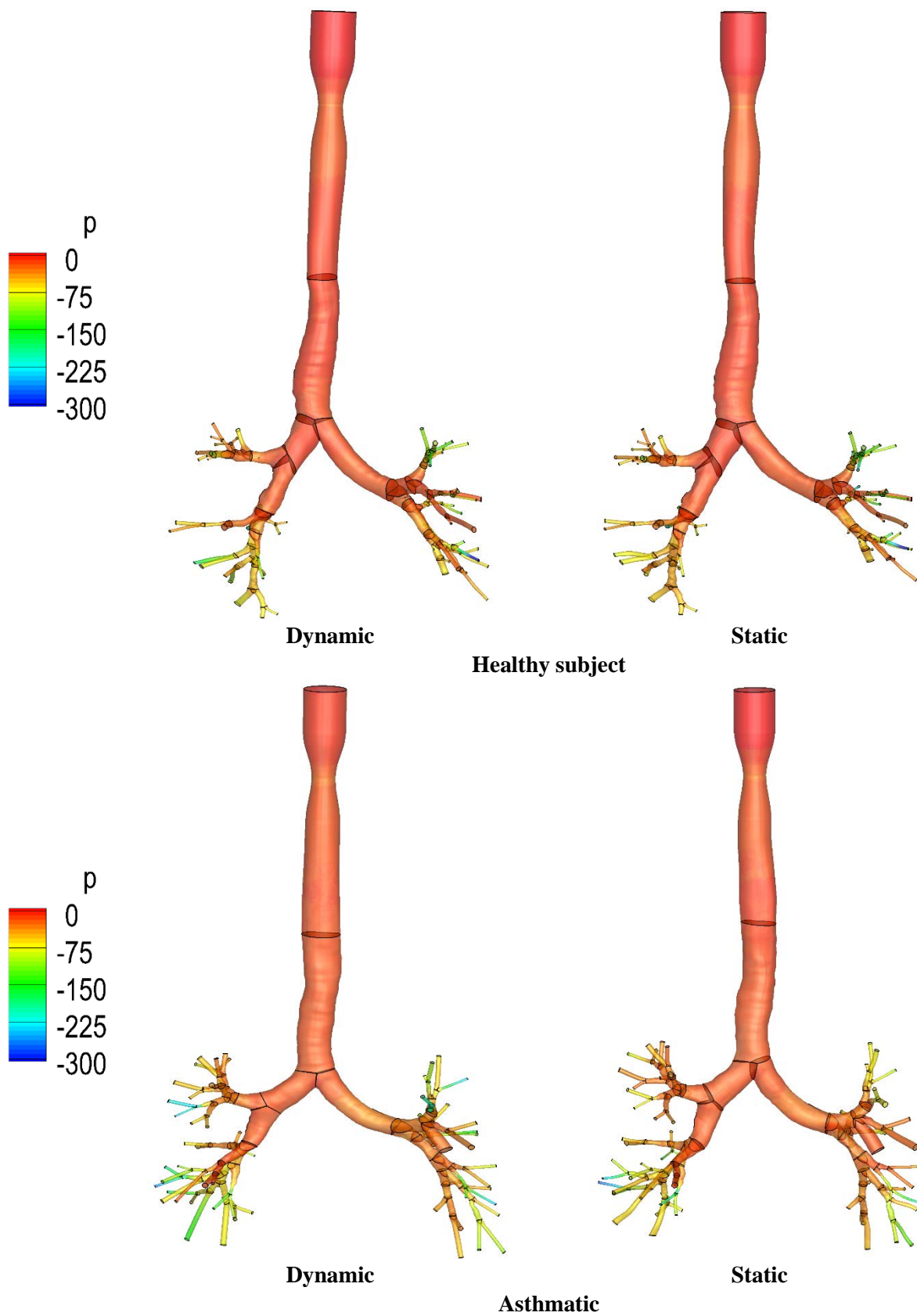
Asthmatic
Figure 5.3. Pressure distribution at peak inhalation

6   SUMMARY AND FUTURE WORK

6.1 Summary

In this thesis, we developed dynamic breathing lung models using static and dynamic CT images for both healthy and asthmatic human lungs. We extracted new local features of the lung function in association with the non-linear nature of lung motion for both healthy and asthmatic lungs.

6.1.1   Assessment of regional non-linear ventilation and tissue deformation using three breath-hold CT data sets

We evaluated the non-linear characteristics of the human lung via image registration-derived local variables based on volumetric MDCT lung image data of six normal human subjects acquired at three inflation levels: 20% of vital capacity (VC), 60% VC and 80% VC. Local variables included Jacobian and maximum shear strain for assessment of lung deformation, and air volume change for assessment of air distribution. First, the variables linearly interpolated between 20% and 80% VC images to reflect deformation from 20% to 60% VC were compared with those of direct registration of 20% and 60% VC images. The result showed that the linearly-interpolated variables agreed only qualitatively with those of registration. Then, a quadratic (or linear) interpolation was introduced to link local variables to global air volumes of three images (or 20% and 80% VC images). A sinusoidal breathing waveform was assumed for assessing the time rate of change of these variables. The results indicated significant differences between two-image and three-image results ($P<0.05$). The three-image results for the whole lung showed that the peak of the maximum shear rate occurred at 37% of the maximum volume difference between 20% and 80% VC, while the peaks for the Jacobian and flow rate occurred at 50%.

This was in agreement with accepted physiology whereby lung tissues deform more at lower lung volumes due to lower elasticity and greater compliance. Furthermore, the three-image results showed that the upper and middle lobes, even in the recumbent, supine posture, reached full expansion earlier than the lower lobes.

6.1.2 Assessment of regional ventilation and deformation using 4D-CT imaging for healthy human lungs during tidal breathing

We assessed regional ventilation, nonlinearity, and hysteresis of human lungs during dynamic breathing via image registration of 4D-CT scans. Six healthy adult humans were studied by spiral multidetector-row CT during controlled tidal breathing as well as during total lung capacity and functional residual capacity breath holds. Static images were utilized to contrast static vs. dynamic (deep vs. tidal) breathing. A rolling-seal piston system was employed to maintain consistent tidal breathing during 4D-CT spiral image acquisition, providing required between-breath consistency for physiologically meaningful reconstructed respiratory motion. Registration-derived variables including local air volume and anisotropic deformation index were employed to assess regional ventilation and lung deformation. Lobar distributions of air volume change during tidal breathing were correlated with those of deep breathing ($R^2 \approx 0.84$). Small discrepancies between tidal and deep breathing were shown to be likely due to different distributions of air volume change in the left and the right lungs. We also demonstrated an asymmetric characteristic of flow rate between inhalation and exhalation. With ADI, we were able to quantify nonlinearity and hysteresis of lung deformation that can only be captured in dynamic images. Nonlinearity quantified by ADI is greater during inhalation, and it is stronger in the lower

lobes (P < 0.05). Lung hysteresis estimated by the difference of ADI between inhalation and exhalation is more significant in the right lungs than that in the left lungs.

6.1.3   *A 4D-CT comparison of healthy vs. asthmatic human lungs*

We tried to explore new insights in the dynamics of asthmatic human lungs using four-dimensional computed tomography (4D-CT) image data acquired during tidal breathing. Volumetric image data were acquired for 5 non-severe asthmatic and one severe asthmatic human volunteers. Besides 4D-CT image data, function residual capacity and total lung capacity image data during breath-hold were acquired for comparison with dynamic scans. Quantitative results were compared with the previously reported analysis of five healthy human lungs. Using an image registration technique, local variables such as regional ventilation and anisotropic deformation index (ADI) were estimated. Regional ventilation characteristics of non-severe asthmatic subjects were similar to those of healthy subjects, but different from the severe asthmatic subject. Lobar air flow fractions were also well correlated between static and dynamic scans ($R^2 > 0.84$). However, local ventilation heterogeneity significantly increased during tidal breathing in both healthy and asthmatic subjects relative to that of breath-hold perhaps because of airway resistance present only in dynamic breathing. ADI was used to quantify non-linearity and hysteresis of lung motion during tidal breathing. Non-linearity was greater on inhalation than exhalation among all subjects. However, exhalation non-linearity among asthmatic subjects was greater than healthy subjects and the difference diminished during inhalation. An increase of non-linearity during exhalation in asthmatic subjects accounted for lower hysteresis relative to that of healthy ones. Thus, assessment of non-linearity differences between healthy and

asthmatic lungs during exhalation may provide quantitative metrics for subject identification and outcome assessment of new interventions.

6.1.4 *CFD simulation of asthmatic lungs during tidal breathing*

We applied CFD to model an asthmatic breathing lung using both static and 4D-CT image data. We applied improved algorithms introduced by Miyawaki et al. (51) to deform airway mesh and achieve physiologically-consistent boundary conditions. We quantified regional air flow and pressure drop distribution within the airways. Furthermore, we compared our results with the analysis obtained from the CFD simulation for a healthy subject. The result showed that there is no significant change in air flow and pressure drop in the 1st and 2nd generations of the airways. However, in smaller airways, we observed different distributions of air flow and pressure distribution. The results suggested that CFD simulation may use as a predictor of airway resistance in small airways.

6.2 Future work

6.2.1 *Quantitative assessment of regional structural alteration in asthmatic lungs using 4D-CT image data*

Functional variables such as regional ventilation and deformation estimated in Chapters 3 and 4 can be utilized to establish a relationship with structural variables. Local alterations of structural variables in asthmatic subjects during tidal breathing include bifurcation angle, circularity, airway wall thickness (WT), and hydraulic diameter (Dh). Their correlations with other imaging and PFT-based global and lobar metrics, including lung shape, regional ventilation, and anisotropic deformation can be investigated. It is expected that the correlation between those variables may provide necessary information to predict regional airflow obstruction and constricted airways.

6.2.2 *CFD simulation of a deforming human lung using 4DCT images for multiple subjects of asthmatic and healthy lungs*

In this study only one healthy subject and one asthmatic subject were investigated with CFD simulations based on dynamic and static images. To find common features and classify those features among a population of healthy and asthmatic lungs, more subjects shall be utilized. Also, image data from subjects with non-severe and sever asthmatics can be acquired to estimate and predict the progression of asthma among patients. For this purpose, the image data and results obtained in Chapters 3 and 4 can be used for the CFD simulation of 4D-CT analysis. However, if more data is needed, we need to address issues such as imaging protocol, radiation dose and cost.

BIBLIOGRAPHY

1. **Amelon R**, **Cao K**, **Ding K**, **Christensen GE**, **Reinhardt JM**, **Raghavan ML**. Three-dimensional characterization of regional lung deformation. *J Biomech* 44: 2489–2495, 2011.

2. **Aznar MC**, **Persson GF**, **Kofoed IM**, **Nygaard DE**, **Korreman SS**. Irregular breathing during 4DCT scanning of lung cancer patients: is the midventilation approach robust? *Phys Medica PM Int J Devoted Appl Phys Med Biol Off J Ital Assoc Biomed Phys AIFB* 30: 69–75, 2014.

3. **Bauman G**, **Eichinger M**. Ventilation and perfusion magnetic resonance imaging of the lung. *Pol J Radiol* 77: 37–46, 2012.

4. **van Beek EJR**, **Wild JM**, **Kauczor H-U**, **Schreiber W**, **Mugler JP**, **de Lange EE**. Functional MRI of the lung using hyperpolarized 3-helium gas. *J Magn Reson Imaging* 20: 540–554, 2004.

5. **Boldea V**, **Sharp GC**, **Jiang SB**, **Sarrut D**. 4D-CT lung motion estimation with deformable registration: Quantification of motion nonlinearity and hysteresis. *Med Phys* 35: 1008–1018, 2008.

6. **Busacker A**, **Newell J John D**, **Keefe T**, **Hoffman EA**, **Granroth JC**, **Castro M**, **Fain S**, **Wenzel S**. A multivariate analysis of risk factors for the air-trapping asthmatic phenotype as measured by quantitative ct analysis. *Chest* 135: 48–56, 2009.

7. **Campana L**, **Kenyon J**, **Zhalehdoust-Sani S**, **Tzeng Y-S**, **Sun Y**, **Albert M**, **Lutchen KR**. Probing airway conditions governing ventilation defects in asthma via hyperpolarized MRI image functional modeling. *J Appl Physiol* 106: 1293–1300, 2009.

8. **Cao K**, **Ding K**, **Christensen GE**, **Reinhardt JM**. Tissue volume and vesselness measure preserving nonrigid registration of lung CT images. , p. 762309-762309–8.

9. **Chae EJ**, **Seo JB**, **Lee J**, **Kim N**, **Goo HW**, **Lee HJ**, **Lee CW**, **Ra SW**, **Oh Y-M**, **Cho YS**. Xenon Ventilation Imaging Using Dual-Energy Computed Tomography in Asthmatics: Initial Experience. *Invest. Radiol.* (April 2010). doi: 10.1097/RLI.0b013e3181dfdae0.

10. **Choi J**, **Tawhai MH**, **Hoffman EA**, **Lin C-L**. On intra- and intersubject variabilities of airflow in the human lungs. *Phys Fluids 1994-Present* 21: 101901, 2009.

11. **Choi S**, **Hoffman EA**, **Wenzel SE**, **Castro M**, **Fain SB**, **Jarjour NN**, **Schiebler ML**, **Chen K**, **Lin C-L**. Quantitative Assessment of Multiscale Structural and Functional Alterations in Asthmatic Populations. *J Appl Physiol* 118: 1286–1298, 2015.

12. **Choi S**, **Hoffman EA**, **Wenzel SE**, **Castro M**, **Lin C-L**. Improved CT-based estimate of pulmonary gas trapping accounting for scanner and lung-volume variations in a multicenter asthmatic study. *J Appl Physiol* 117: 593–603, 2014.

13. **Choi S**, **Hoffman EA**, **Wenzel SE**, **Tawhai MH**, **Yin Y**, **Castro M**, **Lin C-L**. Registration-based Assessment of Regional Lung Function via Volumetric CT Images of Normals vs. Severe Asthmatics. *J Appl Physiol* 115: 730–742, 2013.

14. **Chon D**, **Beck KC**, **Simon BA**, **Shikata H**, **Saba OI**, **Hoffman EA**. Effect of low-xenon and krypton supplementation on signal/noise of regional CT-based ventilation measurements. *J Appl Physiol* 102: 1535–1544, 2007.

15. **Christensen GE**, **Song JH**, **Lu W**, **Naqa IE**, **Low DA**. Tracking lung tissue motion and expansion/compression with inverse consistent image registration and spirometry. *Med Phys* 34: 2155–2163, 2007.

16. **Ding K**, **Bayouth JE**, **Buatti JM**, **Christensen GE**, **Reinhardt JM**. 4DCT-based measurement of changes in pulmonary function following a course of radiation therapy. *Med Phys* 37: 1261–1272, 2010.

17. **Ding K**, **Cao K**, **Christensen GE**, **Hoffman EA**, **Reinhardt JM**. Registration-based regional lung mechanical analysis: retrospectively reconstructed dynamic imaging versus static breath-hold image acquisition. , p. 72620D–72620D–9.

18. **Downie SR**, **Salome CM**, **Verbanck S**, **Thompson B**, **Berend N**, **King GG**. Ventilation heterogeneity is a major determinant of airway hyperresponsiveness in asthma, independent of airway inflammation. *Thorax* 62: 684–689, 2007.

19. **Dubsky S**, **Hooper SB**, **Siu KKW**, **Fouras A**. Synchrotron-based dynamic computed tomography of tissue motion for regional lung function measurement. *J R Soc Interface* 9: 2213–2224, 2012.

20. **Eom J**, **Xu XG**, **De S**, **Shi C**. Predictive modeling of lung motion over the entire respiratory cycle using measured pressure-volume data, 4DCT images, and finite-element analysis. *Med Phys* 37: 4389–4400, 2010.

21. **Flohr T**, **Stierstorfer K**, **Raupach R**, **Ulzheimer S**, **Bruder H**. Performance evaluation of a 64-slice CT system with z-flying focal spot. *RöFo Fortschritte Auf Dem Geb Röntgenstrahlen Nukl* 176: 1803–1810, 2004.

22. **Fredberg JJ**, **Kamm RD**. STRESS TRANSMISSION IN THE LUNG: Pathways from Organ to Molecule. *Annu Rev Physiol* 68: 507–541, 2006.

23. **Fuld MK**, **Grout RW**, **Guo J**, **Morgan JH**, **Hoffman EA**. Systems for Lung Volume Standardization during Static and Dynamic MDCT-based Quantitative Assessment of Pulmonary Structure and Function. *Acad Radiol* 19: 930–940, 2012.

24. **Fung Y**. *Foundations of solid mechanics*. Prentice Hall, 1965.

25. **Gorbunova V**, **Lo P**, **Ashraf H**, **Dirksen A**, **Nielsen M**, **Bruijne M de**. Weight Preserving Image Registration for Monitoring Disease Progression in Lung CT [Online]. In: *Medical Image Computing and Computer-Assisted Intervention – MICCAI 2008*, edited by Metaxas D, Axel L, Fichtinger G, Székely G. Springer Berlin Heidelberg, p. 863–870. http://link.springer.com/chapter/10.1007/978-3-540-85990-1_104 [29 Nov. 2015].

26. **Grinberg L**, **Karniadakis GE**. Outflow Boundary Conditions for Arterial Networks with Multiple Outlets. *Ann Biomed Eng* 36: 1496–1514, 2008.

27. **Guerrero T**, **Sanders K**, **Castillo E**, **Zhang Y**, **Bidaut L**, **Pan T**, **Komaki R**. Dynamic ventilation imaging from four-dimensional computed tomography. *Phys Med Biol* 51: 777, 2006.

28. **Hankinson JL**, **Kawut SM**, **Shahar E**, **Smith LJ**, **Stukovsky KH**, **Barr RG**. Performance of american thoracic society-recommended spirometry reference values in a multiethnic sample of adults: The multi-ethnic study of atherosclerosis (mesa) lung study. *Chest* 137: 138–145, 2010.

29. **Hankinson JL**, **Odencrantz JR**, **Fedan KB**. Spirometric Reference Values from a Sample of the General U.S. Population. *Am J Respir Crit Care Med* 159: 179–187, 1999.

30. **Hasan A**. *Understanding Mechanical Ventilation: A Practical Handbook*. Springer Science & Business Media, 2010.

31. **Hoffman EA**. Effect of body orientation on regional lung expansion: a computed tomographic approach. *J Appl Physiol* 59: 468–480, 1985.

32. **Hoffman EA**, **Acharya RS**, **Wollins JA**. Computer-aided analysis of regional lung air content using three-dimensional computed tomographic images and multinomial models. *Math Model* 7: 1099–1116, 1986.

33. **Hoffman EA**, **Ritman EL**. Effect of body orientation on regional lung expansion in dog and sloth. *J Appl Physiol* 59: 481–491, 1985.

34. **Horsfield K**, **Dart G**, **Olson DE**, **Filley GF**, **Cumming G**. Models of the human bronchial tree. *J Appl Physiol* 31: 207–217, 1971.

35. **Hu S**, **Hoffman EA**, **Reinhardt JM**. Automatic lung segmentation for accurate quantitation of volumetric X-ray CT images. *IEEE Trans Med Imaging* 20: 490–498, 2001.

36. **Hughes M**, **Black R**. *Advanced Respiratory Critical Care*. OUP Oxford, 2011.

37. **Ireland RH**, **Bragg CM**, **McJury M**, **Woodhouse N**, **Fichele S**, **van Beek EJR**, **Wild JM**, **Hatton MQ**. Feasibility of Image Registration and Intensity-Modulated Radiotherapy Planning With Hyperpolarized Helium-3 Magnetic Resonance Imaging for Non–Small-Cell Lung Cancer. *Int J Radiat Oncol* 68: 273–281, 2007.

38. **Iyer KS**, **Grout RW**, **Zamba GK**, **Hoffman EA**. Repeatability and Sample Size Assessment Associated with Computed Tomography-Based Lung Density Metrics. *Chronic Obstr Pulm Dis Miami Fla* 1: 97–104, 2014.

39. **Jahani N**, **Choi S**, **Choi J**, **Hoffman EA**, **Comellas AP**, **Kline JN**, **Lin C-L**. A 4D-CT Comparison of Healthy vs. Asthmatic Human Lungs. .

40. **Jahani N**, **Choi S**, **Choi J**, **Iyer K**, **Hoffman EA**, **Lin C-L**. Assessment of Regional Ventilation and Deformation Using 4D-CT Imaging for Healthy Human Lungs during Tidal Breathing. *J. Appl. Physiol.* (August 27, 2015). doi: 10.1152/japplphysiol.00339.2015.

41. **Jahani N**, **Yin Y**, **Hoffman EA**, **Lin C-L**. Assessment of regional non-linear tissue deformation and air volume change of human lungs via image registration. *J Biomech* 47: 1626–1633, 2014.

42. **Jd E**, **A E**. Lung hysteresis: a morphological view. *Histol Histopathol* 19: 159–166, 2004.

43. **Kabus S**, **Klinder T**, **Murphy K**, **Ginneken B van**, **Lorenz C**, **Pluim JPW**. Evaluation of 4D-CT Lung Registration [Online]. In: *Medical Image Computing and Computer-Assisted Intervention – MICCAI 2009*, edited by Yang G-Z, Hawkes D, Rueckert D, Noble A, Taylor C. Springer Berlin Heidelberg, p. 747–754. http://link.springer.com/chapter/10.1007/978-3-642-04268-3_92 [29 Nov. 2015].

44. **de Lange EE**, **Altes TA**, **Patrie JT**, **Gaare JD**, **Knake JJ**, **Mugler I John P**, **Platts-Mills TA**. Evaluation of asthma with hyperpolarized helium-3 mri*: Correlation with clinical severity and spirometry. *Chest* 130: 1055–1062, 2006.

45. **de Lange EE**, **Altes TA**, **Patrie JT**, **Parmar J**, **Brookeman JR**, **Mugler III JP**, **Platts-Mills TAE**. The variability of regional airflow obstruction within the lungs of patients with asthma: Assessment with hyperpolarized helium-3 magnetic resonance imaging. *J Allergy Clin Immunol* 119: 1072–1078, 2007.

46. **Levitzky MG**. *Pulmonary physiology*. 8th ed. New York: McGraw-Hill, 2013.

47. **Lin C l**, **Tawhai MH**, **Mclennan G**, **Hoffman EA**. Computational fluid dynamics. *IEEE Eng Med Biol Mag* 28: 25–33, 2009.

48. **Lin C-L**, **Tawhai MH**, **Hoffman EA**. Multiscale image-based modeling and simulation of gas flow and particle transport in the human lungs. *Wiley Interdiscip Rev Syst Biol Med* 5: 643–655, 2013.

49. **Lin C-L**, **Tawhai MH**, **McLennan G**, **Hoffman EA**. Characteristics of the turbulent laryngeal jet and its effect on airflow in the human intra-thoracic airways. *Respir Physiol Neurobiol* 157: 295–309, 2007.

50. **Milic-Emili J**, **Henderson JAM**, **Dolovich MB**, **Trop D**, **Kaneko K**. Regional distribution of inspired gas in the lung. *J Appl Physiol* 21: 749–759, 1966.

51. **Miyawaki S**, **Choi S**, **Hoffman EA**, **Lin C-L**. A 4DCT imaging-based breathing human lung model with relative hysteresis. .

52. **Miyawaki S**, **Tawhai MH**, **Hoffman EA**, **Lin C-L**. Effect of Carrier Gas Properties on Aerosol Distribution in a CT-based Human Airway Numerical Model. *Ann Biomed Eng* 40: 1495–1507, 2012.

53. **Miyawaki S**, **Tawhai MH**, **Hoffman EA**, **Lin C-L**. An automatic generation of non-uniform mesh for CFD analyses of image-based multiscale human airway models [Online]. APS Meeting Abstracts http://adsabs.harvard.edu/abs/2014APS..DFDD15010M [30 Jun. 2016].

54. **Napadow VJ**, **Mai V**, **Bankier A**, **Gilbert RJ**, **Edelman R**, **Chen Q**. Determination of regional pulmonary parenchymal strain during normal respiration using spin inversion tagged magnetization MRI. *J Magn Reson Imaging* 13: 467–474, 2001.

55. **National Heart Lung and Blood Institute**. *Expert Panel Report 3 (EPR 3): guidelines for the diagnosis and management of asthma*. Bethesda: National Institutes of Health, 2007.

56. **Newell JD**, **Fuld MK**, **Allmendinger T**, **Sieren JP**, **Chan K-S**, **Guo J**, **Hoffman EA**. Very Low-Dose (0.15 mGy) Chest CT Protocols Using the COPDGene 2 Test Object and a Third-Generation Dual-Source CT Scanner With Corresponding Third-Generation Iterative Reconstruction Software. *Invest Radiol* 50: 40–45, 2015.

57. **Newman KB**, **Lynch DA**, **Newman LS**, **Ellegood D**, **Newell J John D**. QUantitative computed tomography detects air trapping due to asthma. *Chest* 106: 105–109, 1994.

58. **Noel CE**, **Parikh PJ**. Effect of mid-scan breathing changes on quality of 4DCT using a commercial phase-based sorting algorithm. *Med Phys* 38: 2430–2438, 2011.

59. **Olson LE**, **Rodarte JR**. Regional differences in expansion in excised dog lung lobes. *J Appl Physiol* 57: 1710–1714, 1984.

60. **Pan T**. Comparison of helical and cine acquisitions for 4D-CT imaging with multislice CT. *Med Phys* 32: 627–634, 2005.

61. **Petersson J**, **Sánchez-Crespo A**, **Rohdin M**, **Montmerle S**, **Nyrén S**, **Jacobsson H**, **Larsson SA**, **Lindahl SGE**, **Linnarsson D**, **Glenny RW**, **Mure M**. Physiological evaluation of a new quantitative SPECT method measuring regional ventilation and perfusion. *J Appl Physiol* 96: 1127–1136, 2004.

62. **Reinhardt JM**, **Ding K**, **Cao K**, **Christensen GE**, **Hoffman EA**, **Bodas SV**. Registration-based estimates of local lung tissue expansion compared to xenon CT measures of specific ventilation. *Med Image Anal* 12: 752–763, 2008.

63. **Rietzel E**, **Pan T**, **Chen GTY**. Four-dimensional computed tomography: Image formation and clinical protocol. *Med Phys* 32: 874–889, 2005.

64. **Rikxoort EM van**, **Prokop M**, **Hoop B de**, **Viergever MA**, **Pluim JPW**, **Ginneken B van**. Automatic Segmentation of the Pulmonary Lobes from Fissures, Airways, and Lung Borders: Evaluation of Robustness against Missing Data [Online]. In: *Medical Image Computing and Computer-Assisted Intervention – MICCAI 2009*, edited by Yang G-Z, Hawkes D, Rueckert D, Noble A, Taylor C. Springer Berlin Heidelberg, p. 263–271. http://link.springer.com/chapter/10.1007/978-3-642-04268-3_33 [29 Nov. 2015].

65. **Shikata H**, **Hoffman EA**, **Sonka M**. Automated segmentation of pulmonary vascular tree from 3D CT images. , p. 107–116.

66. **Stein K**, **Tezduyar T**, **Benney R**. Mesh Moving Techniques for Fluid-Structure Interactions With Large Displacements. *J Appl Mech* 70: 58–63, 2003.

67. **Stocks J**, **Quanjer PH**. Reference values for residual volume, functional residual capacity and total lung capacity. ATS Workshop on Lung Volume Measurements. Official Statement of The European Respiratory Society. *Eur Respir J* 8: 492–506, 1995.

68. **Tschirren J**, **Hoffman EA**, **Mclennan G**, **Sonka M**. Intrathoracic airway trees: segmentation and airway morphology analysis from low-dose CT scans. *IEEE Trans Med Imaging* 24: 1529–1539, 2005.

69. **Tzeng Y-S**, **Lutchen K**, **Albert M**. The difference in ventilation heterogeneity between asthmatic and healthy subjects quantified using hyperpolarized 3He MRI. *J Appl Physiol* 106: 813–822, 2009.

70. **Venegas JG**, **Winkler T**, **Musch G**, **Vidal Melo MF**, **Layfield D**, **Tgavalekos N**, **Fischman AJ**, **Callahan RJ**, **Bellani G**, **Scott Harris R**. Self-organized patchiness in asthma as a prelude to catastrophic shifts. *Nature* 434: 777–782, 2005.

71. **Voorhees A**, **An J**, **Berger KI**, **Goldring RM**, **Chen Q**. Magnetic resonance imaging-based spirometry for regional assessment of pulmonary function. *Magn Reson Med* 54: 1146–1154, 2005.

72. **Weibel ER**. Geometry and Dimensions of Airways of the Respiratory Zone [Online]. In: *Morphometry of the Human Lung*. Springer Berlin Heidelberg, p. 56–73. http://link.springer.com/chapter/10.1007/978-3-642-87553-3_6 [30 Jun. 2016].

73. **West JB**, **Matthews FL**. Stresses, strains, and surface pressures in the lung caused by its weight. *J Appl Physiol* 32: 332–345, 1972.

74. **White B**, **Zhao T**, **Lamb J**, **Wuenschel S**, **Bradley J**, **Naqa IE**, **Low D**. Distribution of lung tissue hysteresis during free breathing. *Med Phys* 40: 43501, 2013.

75. **Wongviriyawong C**, **Harris RS**, **Greenblatt E**, **Winkler T**, **Venegas JG**. Peripheral resistance: a link between global airflow obstruction and regional ventilation distribution. *J Appl Physiol* 114: 504–514, 2013.

76. **Wu D**, **Miyawaki S**, **Tawhai MH**, **Hoffman EA**, **Lin C-L**. A Numerical Study of Water Loss Rate Distributions in MDCT-Based Human Airway Models. *Ann. Biomed. Eng.* (April 14, 2015). doi: 10.1007/s10439-015-1318-3.

77. **Wu D**, **Tawhai MH**, **Hoffman EA**, **Lin C-L**. A Numerical Study of Heat and Water Vapor Transfer in MDCT-Based Human Airway Models. *Ann Biomed Eng* 42: 2117–2131, 2014.

78. **Yamamoto T**, **Kabus S**, **Klinder T**, **Lorenz C**, **von Berg J**, **Blaffert T**, **Loo BW**, **Keall PJ**. Investigation of four-dimensional computed tomography-based pulmonary ventilation imaging in patients with emphysematous lung regions. *Phys Med Biol* 56: 2279–2298, 2011.

79. **Yang D**, **Lu W**, **Low DA**, **Deasy JO**, **Hope AJ**, **Naqa IE**. 4D-CT motion estimation using deformable image registration and 5D respiratory motion modeling. *Med Phys* 35: 4577–4590, 2008.

80. **Yin Y**, **Choi J**, **Hoffman EA**, **Tawhai MH**, **Lin C-L**. Simulation of pulmonary air flow with a subject-specific boundary condition. *J Biomech* 43: 2159–2163, 2010.

81. **Yin Y**, **Choi J**, **Hoffman EA**, **Tawhai MH**, **Lin C-L**. A multiscale MDCT image-based breathing lung model with time-varying regional ventilation. *J Comput Phys* 244: 168–192, 2013.

82. **Yin Y**, **Hoffman EA**, **Ding K**, **Reinhardt JM**, **Lin C-L**. A cubic B-spline-based hybrid registration of lung CT images for a dynamic airway geometric model with large deformation. *Phys Med Biol* 56: 203, 2011.

83. **Yin Y**, **Hoffman EA**, **Lin C-L**. Mass preserving nonrigid registration of CT lung images using cubic B-spline. *Med Phys* 36: 4213–4222, 2009.

84. **Zhang J**, **Ma J**, **Zhou S**, **Hubbs JL**, **Wong TZ**, **Folz RJ**, **Evans ES**, **Jaszczak RJ**, **Clough R**, **Marks LB**. Radiation-Induced Reductions in Regional Lung Perfusion: 0.1–12 Year Data From a Prospective Clinical Study. *Int J Radiat Oncol* 76: 425–432, 2010.